Multifluid modelling and simulation of advanced electrodeless plasma thrusters

by

Diego García Lahuerta

A dissertation submitted in partial fulfillment of the requirements for the degree of Doctor of Philosophy in

Aerospace Engineering

Universidad Carlos III de Madrid

Advisor(s):

Mario Merino Martínez
Eduardo Ahedo Galilea

Tutor:

Mario Merino Martínez

March 2025

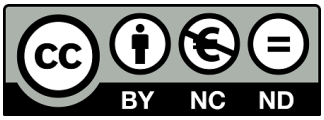

A mis abuelos: Catalina, Josefina, Paco y Mariano.

Acknowledgements

El primer agradecimiento es, como no puede ser de otra forma, a mis padres por educarme durante veintiocho años; en particular a mi madre, Rosa, por su infinita paciencia durante toda mi vida y en especial durante estos últimos meses de escritura de la tesis y a mi padre, Sergio, por inculcarme la curiosidad y el amor por la ciencia. Huelga decir que no sería quien soy sin vosotros. A mis hermanos Carlos y Sergio, porque resistirme a no mataros en todos estos años me ha dado la templanza necesaria para sobrellevar estos cuatro años de doctorado y a María por estar casi desde siempre y siempre que ha hecho falta. También a toda mi familia que, de un modo u otro, me ha acompañado desde el principio.

Por supuesto, quiero expresar mi agradecimiento a mis supervisores, Mario Merino y Eduardo Ahedo, por ofrecerme la oportunidad de adentrarme en el mundo de la física del plasma y la propulsión espacial. Le estoy particularmente agradecido a Mario por su paciencia y su diligente ayuda. Debo también agradecer su trabajo al resto de profesores y postdocs del grupo de propulsión espacial, Jaume, Adrián, Jiewei y Pablo que, aunque de manera más indirecta, también han hecho posible esta tesis. Quiero además agradecer a Christian, Olympia y Lidia su ayuda desde los despachos durante estos últimos cuatro años.

En este orden de ideas, quiero agradecer a todas las personas que me han acompañado estos últimos años, empezando por mis compañeros de despacho Celián, Davide y, durante un tiempo, Matteo Ripoli por todos los momentos que hemos vivido dentro y fuera de la universidad. A mis compañeros de cordada y caminatas, Davide Poli y Matteo Guaita, por nuestro tiempo en la montaña y también por prestarme su inestimable ayuda y sus conocimientos cuando lo he necesitado. A Guille que, aunque ha llegado hace poco, ha conseguido que se hable castellano en el grupo y ha nombrado mi código. A todo el resto de compañeros del grupo EP2: Marco, Scherezade, Simone, Alberto Modesti, Alberto Marín, Tatiana, Borja, Andrés, Pedro, Iñaki y Hugo; porque de todos he aprendido algo y todos habéis hecho de la universidad un lugar mucho más entretenido.

Merecen una mención particular mis compañeros del equipo de voleibol de la UC3M y sus entrenadores, Guille y Sandra, porque cada entrenamiento y cada partido me han servido para desconectar, para salir del despacho a una hora decente y, todo sea dicho, para ir por la cara a algún campeonato de España.

Este doctorado tampoco hubiese sido posible sin Raquel, Namir, Andy y Victor que son, desde hace ya siete años, mi segunda familia. Tampoco sin Yuriko y María que hicieron, de un piso interior de Malasaña, un hogar; sin María en especial porque, de tanto quejarse de sus problemas, hace que se me olviden los míos. Me quiero acordar aquí también de mis amigos de Alcalá, Sito, María, Iván, Félix, Rubén e Isra y, sobre todo, de los Spooky Big Peach, Jorge y Néstor, aunque esa maqueta no vaya a salir nunca. También de mis compañeros de la Autónoma y del máster, Mario, Clara y Anna; que espero me sigan admitiendo en el grupo de los físicos. No puedo olvidarme de mi amigo Guille, que lleva a mi lado casi toda la vida, por su indefectible amistad y su apoyo perenne.

Por último, pero no menos importante; gracias a Paula, con quien cualquier cantidad de tiempo se hace corta. Por alegrarme cada día desde hace ya más de tres años, espero que sean muchos más.

Diego García Lahuerta
Enero 2025

This work has been carried out as part of the ZARATHUSTRA project, which has received funding from the European Research Council (ERC) under the European Union's Horizon 2020 research and innovation programme (project ZARATHUSTRA, grant agreement No 950466).

Published and submitted content

Scientific Journals

- Mario Merino, **Diego García-Lahuerta** and Eduardo Ahedo. *Plasma Acceleration in a Magnetic Arch. Plasma Sources Science & Technology* (2023). **32** 065005. DOI 10.1088/1361-6595/acd476. The candidate contributed to software development and testing, conducted the investigation, prepared the figures, and reviewed the manuscript. The full content of this article is reproduced in chapter 4 of the thesis. Whenever material from this source is included in this thesis, it is singled out with typographic means and an explicit reference.

- **Diego García-Lahuerta**, Mario Merino and Eduardo Ahedo. *Effect of collisions and facility effects on magnetic nozzle operation* (under review). The candidate contributed to software development and testing, conducted the investigation, prepared the figures, and wrote the draft manuscript. The full content of this article is reproduced in chapter 5 of the thesis. Whenever material from this source is included in this thesis, it is singled out with typographic means and an explicit reference.

Datasets

- Mario Merino, **Diego García-Lahuerta** and Eduardo Ahedo. *Data for: Plasma Acceleration in a Magnetic Arch.* Zenodo, May 18, 2023. DOI 10.5281/zenodo.8016827. The candidate performed the simulations and produced the dataset. The data included here is reproduced in chapter 4 of the thesis. The material from this source included in this thesis is not singled out with typographic means and references.

Other research merits

Conference Proceedings

- Mario Merino, **Diego García-Lahuerta**, Celian Boye, Jaume Navarro-Cavalle and Eduardo Ahedo. *Preliminary model of the plasma expansion in a magnetic arch thruster (and overview of the first prototype).* In International Electric Propulsion Conference, IEPC-2022-423. Boston, Massachusets, June 19-23.

Other conferences:

Other contributions by the candidate in international conferences are listed here:

- Mario Merino, **Diego Garcia-Lahuerta, Celian Boye, Jaume Navarro-Cavalle, Eduardo Ahedo**. *Electrodeless plasma thrusters and magnetized plasma expansions for space propulsion.* In APS Annual Gaseous Electronics Conference, GEC-2022. Sendai, Japan. October, 3-7 2022.
- **Diego García-Lahuerta**, Mario Merino, Eduardo Ahedo. *Simulation of facility effects on magnetic nozzle expansions.* In Plasma Processing and Technology International Conference, Plasma Tech-2023. Lisbon, Portugal. April 24-26, 2023.
- **Diego García-Lahuerta**, Mario Merino, Eduardo Ahedo. *Modeling the effect of neutral dynamics on magnetic nozzle performances.* In International Conference on Phenomena in Ionized Gases, ICPIG XXXV. Egmond an Zee, Netherlands. July 9-14, 2023.
- Mario Merino, Celian Boyé, **Diego García-Lahuerta**, Jaume Navarro-Caballé and Eduardo Ahedo. *Experiments and Simulations of a Magnetic Arch Plasma Expansion for Space Propulsion.* In International Conference on Plasma Science, ICOPS 2023. Santa Fe, New Mexico. May 21 – 25, 2023.
- **Diego Garcia-Lahuerta**, Mario Merino, Eduardo Ahedo. *Simulations of the effect of neutral dynamics in magnetic nozzle expansions.* In APS Annual

Gaseous Electronics Conference, GEC-2023. Ann Arbor, Michigan, October 9 - 13, 2023.

- Mario Merino, Eduardo Ahedo, **Diego García-Lahuerta**, Matteo Guaita, Pedro Jiménez. *PIC and fluid simulations of magnetized plasma expansions for electric propulsion.* In APS Annual Gaseous Electronics Conference, GEC-2024. San Diego, California, September 30 - October 4, 2024.

Resumen

El interés en el desarrollo y la caracterización de motores-cohete de plasma ha crecido de forma continua en los últimos años gracias a la creciente demanda por parte de la industria espacial. En este contexto, el modelado y la simulación de motores de plasma sin electrodos (EPTs) así como su prototipado y testeo es de gran importancia para la comunidad científica de la propulsión eléctrica en su empeño en convertir este tipo de tecnologías en competidoras contra otras con mayor legado en vuelos espaciales. Este interés en el desarrollo de EPTs se basa en el hecho de que, en estos dispositivos, la aceleración del plasma se produce sin contacto en una tobera magnética (MN), eliminando la necesidad de mantener electrodos expuestos al plasma. Esta característica los dota de mayor simplicidad y permite que operen con virtualmente cualquier propulsante.

La tesis que aquí se presenta tiene como objetivo cubrir parte de la falta de conocimiento existente en la expansión de plasma en la pluma de los motores de plasma sin electrodos. En este sentido, una de las principales contribuciones de esta tesis es el desarrollo de una plataforma de simulación, llamada `POSETS`, que utiliza el método de Galerkin discontinuo para resolver modelos multi-fluidos de plasma magnetizado y es lo suficientemente flexible para incluir distintos modelos para el estudio de los múltiples fenómenos que tienen lugar en la operación estacionaria de este tipo de dispositivos. `POSETS` implementa un modelo cuasi-neutro con dos o tres especies fluidas en dos dimensiones que incluye además múltiples procesos colisionales y el efecto de los campos magnéticos autoinducidos por el plasma tanto en geometrías planas como axisimetricas.

Tras la explicación del funcionamiento de dicho software de simulación, esta tesis estudia dos cuestiones que son consideradas de importancia en el desarrollo los EPTs.

La primera de estas cuestiones es la expansión de plasma en una configuración magnética novedosa llamada arco magnético y la evaluación de su viabilidad para la generación de empuje en el contexto de la propulsión espacial. Este arco magnético es una configuración magnética cerrada que aparece cuando se utilizan dos EPTs cilíndricos con polaridades opuestas, así como en ciertas propuestas novedosas para la propulsión espacial. Esta configuración en arco magnético ofrece algunas posibles ventajas frente a las geometrías cilíndricas tal como la reducción del momento

magnético de la aeronave. En este trabajo se examina la extracción del plasma y la generación de empuje, así como el efecto de los campos magnéticos auto-inducidos en la expansión; estos son, a diferencia con los motores cilíndricos, de gran importancia para el funcionamiento del dispositivo.

La segunda cuestión que se aborda es el efecto de los llamados efectos de laboratorio. Se sabe que estos afectan al funcionamiento de los EPTs cilíndricos así como a otras tecnologías opacando el funcionamiento que estos tendrían en el entorno espacial. Con el fin de determinar el impacto de estos efectos en el comportamiento de la tobera magnética, el modelo utilizado para este estudio incluye neutros con dos orígenes; una fuente de plasma con ionización parcial y un fondo de neutros que representa la presión residual que aparece en todos los experimentos llevados a cabo en cámara de vacío. Con este modelo estudiamos la generación de empuje y el efecto de múltiples tipos de colisiones en la expansión.

En resumen, los resultados que se presentan en esta tesis suponen un avance en el entendimiento de la dinámica del plasma en la pluma de los EPTs. El código `POSETS` ofrece una herramienta versátil para el modelado de flujos de plasma magnetizado. Asimismo, el análisis de la configuración en arco magnético y del papel de las colisiones en los EPTs amplían el conocimiento de la comunidad en algunos aspectos clave para este tipo de tecnologías.

Abstract

The interest in the development and testing of plasma thrusters has grown steadily in the last years due to the growing demands of the space industry. In this context, the modelling and simulation of electrodeless plasma thrusters (EPTs) as well as their prototyping and testing is of great significance to the electric propulsion community in its pursue to make this novel technology a contender against more established ones. This interest in the development of EPTs stems from the fact that these devices achieve plasma acceleration in a contactless manner in a magnetic nozzle (MN), eliminating the need for exposed electrodes within the plasma. This characteristic grants them apparent simplicity and the possibility to operate with virtually any propellant.

The present thesis aims to tackle some of the gaps in the understanding of plasma expansion in the plumes of EPTs. One of the main contributions of this thesis is the development of a Discontinuous-Galerkin multifluid simulation platform, coined `POSETS`, that allows for the solution of magnetised plasma flows and is flexible enough to accommodate different models in order to study several different mechanisms taking place in the steady-state operation of these devices. `POSETS` implements a quasi-neutral, two- or three-fluid, two-dimensional model that includes several collisional processes and the effect plasma-induced magnetic field in either planar or axisymmetric geometries.

After the presentation of the workings of said simulation software, this thesis studies two different topics which are considered significant for the development of EPTs.

The first one is the expansion of plasma in a novel magnetic configuration so-called magnetic-arch and the assessment of the feasibility of this configuration for thrust generation in the context of space-propulsion. This magnetic-arch is a closed-line magnetic configuration which appears when flying two cylindrical EPTs with opposed polarities as well as in some novel propulsion concepts. This configuration offers some possible advantages against cylindrical ones such as the reduction in the magnetic moment of the spacecraft. In this work the extraction of plasma and thrust generation are examined along with the effect of plasma-induced magnetic fields which are, in comparison to the magnetic nozzle of a single cylindrical EPTs, of stark relevance to the behaviour of the device.

The second one is the effect of the so-called facility effects which are known to affect the behaviour of cylindrical EPTs and other technologies obscuring the real in-space operation of these devices. In order to gauge the impact of these phenomena in the behaviour of a magnetic nozzle (MN), the model employed for this study includes collisions with neutrals from two origins; a plasma source with imperfect ionization and a background that represents the residual pressure existing in all testing facilities. With this model we gauge the generation of thrust and the effect of several collisions on the expansion.

In summary, the findings presented in this thesis advance the understanding of plasma dynamics in the plumes of EPTs. The `POSETS` simulation platform offers a versatile tool for modelling magnetised plasma flows. Additionally, the analysis of the magnetic-arch configuration and of the role of collisions on EPT performance broadens the knowledge of the community on some key aspects in this propulsion technology.

Contents

List of Figures

List of Tables

Chapter 1

Introduction

1.1 Electric Propulsion

Electric Propulsion (EP) is broadly defined as the use of electrical power to propel spacecraft. The main advantage of electric propulsion against the more common chemical propulsion is the virtually limitless specific energy that can be imparted to the propellant, this energy is only limited by the power available in the spacecraft [1, 2]. This allows for a higher exhaust velocity of the propellant that can be orders of magnitude higher than in chemical rockets where the energy used to accelerate the propellant is only the one stored in the chemical bonds of the propellant used. This higher exhaust velocity allows for a higher specific impulse I_{sp} which, in turn, allows for higher mass efficiency and, therefore, reduced mission cost for a needed propulsive load. Electric propulsion has become a major competitor against its chemical counterpart for in-space propulsion duties for its higher propellant efficiency, however launch vehicles are necessarily propelled with chemical thrusters due to the high-thrust, high-power needs required to escape the vicinity of the Earth.

Broadly speaking, there are three main stages in the operation of an electric thruster. First the propellant is heated or ionized in the case of plasma thrusters, this stage happens usually in a so called ionization chamber. Second, the plasma is accelerated by some of the mechanisms that will be discussed in the following and, lastly, the plasma detaches from the thruster [3]. Several ways of ionizing the plasma are present in today's electric propulsion market, however, let us distinguish each type of thruster by the acceleration mechanism, in this sense we find three main branches:

- Electrothermal thrusters: this type of thrusters work by heating up the propellant which is subsequently accelerated by thermal expansion in a standard de Laval nozzle. This is the case of the arcjet and the resistojet rockets [4, 5].
- Electrostatic thrusters: the thrust in this type of devices is generated by elec-

trostatic acceleration of the plasma once it has been ionized. This is achieved by accelerating ions through an electrostatic potential fall generated by two electrodes. Within this category one finds one of the most common technologies, the Gridded Ion Thruster (GIT) [6, 7, 8]. Electrostatic acceleration is also the mechanism operating in electrospray thrusters, albeit accelerating charged liquid droplets instead of ions in a plasma.

- Electromagnetic thrusters: in this type of thrusters thrust is generated by the Lorentz forces that exist in the magnetic interaction of the internal plasma current and the current in a magnetic circuit. This type of acceleration is present in multiple thrusters present in the market such as the Hall Effect Thruster (HET). [9, 10].

The last two types of acceleration are the most commonly used in electric propulsion nowadays, mainly due to the prevalence of ion and Hall thrusters in today's propulsion landscape.

1.2 Electrodeless Plasma Thrusters

The most common EP technologies nowadays , namely the HET and GIT, require some form of bare electrodes exposed to the plasma in order to neutralize the plasma and/or accelerate the ion beam. Hall Effect Thrusters need a cathode both to generate the discharge and to neutralize the plasma plume downstream while GITs use at least a cathode to neutralize the ion beam with electrons collected at the anode to avoid spacecraft charging and in some cases an extra cathode to produce the discharge via electron bombardment. This need for naked electrodes is one of the most prominent limitations of these technologies for multiple reasons. First, the use of electrodes limits the usable propellants to mainly noble gases, although iodine fed HET have recently made their maiden flight [11] and even water fuel system are being tested [12]. Second, the need for a cathode increases the complexity of the overall propulsion system making the scaling to different powers difficult and, third, the use of electrodes exposed directly to the plasma reduces considerably the lifetime of these thrusters.

For this reasons, in the last decades, two propulsion concepts; the Helicon plasma thruster (HPT) [13, 14] and the Electron-Cyclotron Resonance Thruster (ECRT) [15, 16] have gained interest from the community. This type of thrusters are usually called Electrodeless Plasma Thrusters (EPTs) [17] as they do not need any electrodes to either ionize the plasma nor accelerate it and are considered electromagnetic thrusters in the classification mentioned before. These two thrusters differ mainly in the ionization process in the chamber. The first one couples a helicon

radio-frequency wave with the plasma (mainly collisionally, although other mechanisms are believed to play a role) to heat it and ionize it [18], on the other hand the ECRT ionizes the plasma via microwaves with a frequency that matches the electron-cyclotron resonance in the magnetic field of the ionization chamber. In these thrusters a magnetic field is imposed externally either with the use of electromagnets or permanent magnets. This magnetic field has a three-fold function:

1. The magnetic field plays a crucial role in the wave propagation process. In the case of the HPT, the magnetic field makes the plasma transparent to the propagation of helicon waves [2] while in the ECRT the magnetic field allows the existence of a region where electron-cyclotron resonance efficiently couples the power carried by the a microwave to the plasma.

2. Inside the plasma chamber, which is in most cases cylindrical, the magnetic field is almost parallel to the chamber walls, see figure 1.1. This magnetic field reduces transport of plasma to the walls and collimates the expelled plasma beam in a configuration that is very similar to a θ-pinch [19].

3. This plasma beam expands in a convergent-divergent magnetic field usually named magnetic-nozzle (MN) in which electron thermal energy is converted into ion kinetic energy via the action of an ambipolar electric field [20].

The existence of a magnetic nozzle in the external part of EPTs provides at the same time other potential advantages such as the possibility of exerting thrust vectoring without moving parts in a contact-less fashion by tuning the imposed magnetic field [21].

Despite these multiple possible advantages, EPTs are usually been considered low performing compared to more established thruster technologies. The efficiency and specific impulse of HET are around $35-60\%$ and 1500 s and around $60-80\%$ and 5000 s for GIT [3]. On the other hand, most HPT and ECRT efficiencies are usually in the range of 10% or below [22, 23, 24]. Although some of the last prototypes have shown very promising performances with efficiencies of up to 30% in HPTs [25] and up $40-50\%$ for ECRTs [26], the performance of EPTs is hindered by several phenomena that are yet not fully understood. These problems range from the role of turbulence in the perpendicular anomalous transport of electrons to the coupling of electromagnetic waves with the plasma. In addition, EPTs have some limitations that are inherent to the cylindrical geometry of the magnetic field. To begin with as one can observe in figure 1.1 the rear wall of the ionization chamber in these devices is not magnetically shielded, this is, the magnetic field is quasi-perpendicular to the chamber walls in this area, therefore plasma is lost to the rear wall decreasing efficiency. Moreover, the magnetic nozzle of a cylindrical EPT has a dipole moment that can couple to the geomagnetic field inducing a torque in the spacecraft and affecting the axisymmetry of the plume [27]. Flying EPTs in opposed polarities or

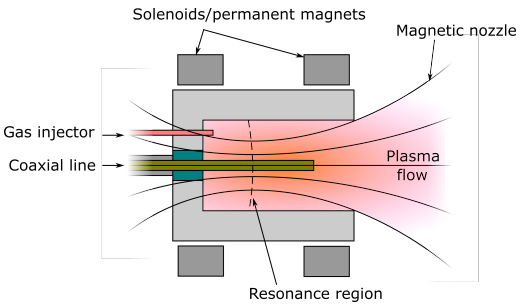

(a) Sketch of an Electron-cyclotron Resonance Thruster [29]

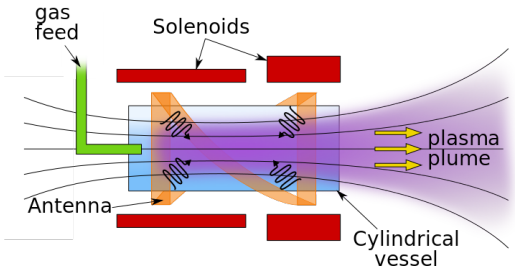

(b) Sketch of a Helicon Plasma Thruster taken from [30]

Figure 1.1: Schematic view of the two main types of EPTs, the Electron-cyclotron resonance thruster and the Helicon plasma thruster.

in a closed line configuration such as the magnetic arch thruster could alleviate these problems [28].

1.3 Plasma Simulations

Experimental development of electric propulsion devices is quite constrained for both economic and technological reasons. In-space measurements of the behaviour of plasma thrusters are limited, therefore most of the characterization of these type of technologies is done in vacuum chambers. However, testing in vacuum chambers is also not ideal. To begin with, measurements are restricted to the part of the plume closer to the thruster, second, vacuum chambers always present a small background pressure which has been shown to affect the performance of EP devices both through the ingestion of neutral gas in the source and the collisions between the expanding plasma and the neutral background [31, 32, 33, 34], lastly, vacuum chambers impose an equipotential surface over the interior of the chamber, this means that the expansion is not completely free as all the points along the surface of the camber are forced to be equipotential.

These limitations have made plasma simulation an important complement in the study and development of plasma thrusters. Therefore multiple approaches have been identified to tackle this problem, nowadays, the most prominent approaches to plasma simulation are:

- Continuous-Kinetic models - Vlasov solvers.
- Particle-Kinetic models - Particle in cell (PIC) solvers.
- Hybrid Fluid-PIC models
- Full-fluid models

Of course, the continuous-kinetic models are the most descriptive ones, however, the six dimensional (3 positions coordinates and 3 velocities) phase space makes this type of simulations unfeasible for multidimensional problems. On the other hand, PIC simulations model particle populations as macro-particles subject to electromagnetic forces and moved along mesh nodes, basically PIC models solve Boltzmann's equation with a reduced number of degrees of freedom by discretizing the distribution function in a finite number of macro-particles with delta-like distributions weighted by the number of particles encompassed in them [35]. Finally, fluid models solve a simplified set of equations stemming from the moments of the velocity distribution function. This way we can solve a set of partial differential equations that describe the plasma in terms of macroscopic its macroscopic properties such as number density, fluid velocity or pressure[36].

Nowadays the most commonly used models are PIC, fluid and hybrid, a combination of all these approaches is necessary to study EP devices as the physics of these devices is rather complex, comprising regions in which a three dimensional PIC treatment is unfeasible and regions in which the fluid description does not offer an accurate depiction of the behaviour of the device. PIC simulations offer higher precision with the backlash of computational cost. On the other hand fluid models are penalized by the weakly-collisional regime that characterizes plasma plumes in which we are forced to choose closures for the fluid equations which are not always justified from the kinetic point of view [37, 38].

1.4 Thesis objectives

This work is devoted to the fluid modelling and simulation of the plumes of electron-driven EPTs such as the helicon and the ECR thruster; other EPT concepts such as the VASIMR that rely on hot ions to produce thrust are out of the scope of this work. In particular, two problems of interest in space propulsion are tackled. The first one is the acceleration and extraction of an ion beam from a closed magnetic field line configuration called a magnetic arch which appears when operating EPTs in opposed polarities as well as in new thruster concepts as the Magnetic Arch Thruster in order to asses its feasibility for space propulsion purposes. The second is the role of neutral dynamics and facility effects in the operation of standard cylindrical magnetic nozzles. These goals con be dissected into four different objectives:

1. The development of a set of different fluid models that capture the key physics of the expansion of plasma in closed-line magnetic arch configurations as well as in collisional cylindrical nozzles.

2. The development of a numerical code for the simulation of magnetized plasma expansions that is flexible enough to handle both planar and axisymmetric geometries as well as different models depending on the physical mechanism that the user wishes to explore.

3. The study of plasma expansion in so-called magnetic arch topologies assessing the extraction of the ion beam from the source the thrust production mechanisms and the effect of plasma-induced magnetic fields in the expansion.

4. The study of collisional and facility effects in the expansion of plasma in cylindrical magnetic nozzles. Including the role of background neutrals and those expelled by the plasma source and their effect on thrust production and efficiency.

1.4.1 Thesis Outline

In order to accomplish said objectives the rest of the thesis is organized as follows:

Chapter 2 starts with a brief introduction on the derivation of fluid theory from the Boltzmann equation. Then, the coordinate systems and magnetic fields employed in the models are presented in order to latter develop fluid equations for each of the different species present in the plasma. The chapter concludes with a brief discussion on the models employed in order to evaluate the collisional cross-sections that appear in some of the fluid equations and a description of the Ampere equation which describes the self-induced magnetic field of our plasma.

Chapter 3 describes the *POSETS* code which has been developed in the context of this thesis. The code employs a Discontinuous Galerkin discretization in order to solve the different models described in the previous chapter. The chapter starts by introducing the Discontinuous Galerkin discretization for hyperbolic systems developed by Cockburn and Shu [39] by describing its weak form as well as the choice of finite elements and the time discretization of the problem. Afterwards, a brief comment on the shock capturing scheme of Hartmann and Houston [40] is introduced in order to avoid spurious oscillations around discontinuities, then, the weak form of the Poisson equation for the magnetic vector potential is discussed. Finally, the numerical implementation of the code is described including the code structure and the verification it has been subject to.

Chapter 4 shows the content of the peer-reviewed publication [41]. In said paper the expansion of plasma in a magnetic arch is studied. First, the concept of the magnetic arch and its appearance in space propulsion are discussed.

Next, we briefly discuss the model employed as their derivation was already performed in chapter 2. The results of the $\beta = 0$ limit are then discussed to latter examine the effect of plasma induced magnetic fields in the thrust performance of the plume.

Chapter 5 is devoted to the study of the effect of collisions and facility effects on the expansion of plasma in a cylindrical magnetic nozzle. The content of this chapter is under review in a peer-reviewed journal. The chapter starts presenting the model employed and discussing the different experimental and numerical evidence that support the assumptions therein. After this, the different simulation scenarios are presented in order to then show the effect of the different collisions in the expansion of the plasma for different neutral background pressures and source utilization efficiencies. The thrust generation and efficiency the nozzle are discussed.

Chapter 6 gathers the main conclusions of the thesis and points out some possible directions in which the work contained here could be continued.

Chapter 2

Fluid Models for Magnetised Plasma Expansions

This chapter is devoted to the presentation and development of the different fluid models in which the rest of the work of the thesis is based. In this chapter we explore the obtention of fluid equations from the Boltzmann equation for the velocity distribution function. We take this as a starting point to obtain fluid models for the different species involved in the plasma. For each species we mention the model employed in the rest of the chapters of the thesis.

2.1 Fluid Theory of Plasmas

Boltzmann's equation for the temporal evolution of the velocity distribution function (VDF) over time reads:

$$\frac{\partial f}{\partial t} + \boldsymbol{v}\nabla_r f + \frac{\boldsymbol{F}}{m}\nabla_v f = \left.\frac{\delta f}{\delta t}\right|_{coll} \tag{2.1}$$

To obtain equations in terms of macroscopic fluid variables one takes the equation above and multiplies by a function $g(\boldsymbol{r}, \boldsymbol{v}, t)$ and integrates over the velocity space. When the function $g(\boldsymbol{r}, \boldsymbol{v}, t) = \alpha v^n$ this operation is usually regarded as taking the *n-th* moment of the VDF. Let us first define the local density as:

$$n(\boldsymbol{r}, t) = \int_v f(r, v, t) d\boldsymbol{v} \tag{2.2}$$

and the weighted average of $g(r, v, t)$ as:

$$\langle g(r,t)\rangle = \frac{\int_v g(r,v,t) f(r,v,t) d\boldsymbol{v}}{\int_v f(r,v,t) d\boldsymbol{v}} = \frac{1}{n(\boldsymbol{r},t)} \int_v g(r,v,t) f(r,v,t) d\boldsymbol{v} \tag{2.3}$$

Finally the fluid velocity can be defined as the average particle velocity as:

$$\boldsymbol{u}(\boldsymbol{r},t) = \langle v(\boldsymbol{r},t)\rangle = \frac{1}{n(\boldsymbol{r},t)}\int_v \boldsymbol{v} f(r,v,t) d\boldsymbol{v} \tag{2.4}$$

Armed with these definitions we go back to the Boltzmann equation and multiply it by a function $g(v)$ that represents some physical property of the particles in the plasma and is only dependent on their velocity and integrate over the velocity space to obtain:

$$\int_v g\partial_t f \mathrm{d}\boldsymbol{v} + \int_v g\boldsymbol{v}\cdot\nabla f \mathrm{d}\boldsymbol{v} + \int_v g\frac{\boldsymbol{F}}{m}\cdot\nabla_v f \mathrm{d}\boldsymbol{v} = \int_v g\frac{\delta f}{\delta t}\bigg|_{coll}\mathrm{d}\boldsymbol{v} \tag{2.5}$$

The first term in equation (2.5) can be written as:

$$\int_v g\partial_t f d\boldsymbol{v} = \int_v \partial_t(gf)\mathrm{d}\boldsymbol{v} - \int_v f\partial_t g \mathrm{d}\boldsymbol{v} \tag{2.6}$$

$$= \partial_t \int_v gf \mathrm{d}\boldsymbol{v} = \partial_t(n(\boldsymbol{r},t)\langle g\rangle) \tag{2.7}$$

The second term can be written as:

$$\int_v g\boldsymbol{v}\cdot\nabla f \mathrm{d}\boldsymbol{v} = \nabla\cdot\int_v fg\boldsymbol{v}\mathrm{d}v = \nabla\cdot(n\langle g\boldsymbol{v}\rangle) \tag{2.8}$$

Similarly, the third term in (2.5) is expanded as:

$$\int_v g\frac{\boldsymbol{F}}{m}\cdot\nabla_v f \mathrm{d}\boldsymbol{v} = \int_v \nabla_v\cdot\left(g\frac{\boldsymbol{F}}{m}f\right)\mathrm{d}\boldsymbol{v} - \int_v gf\nabla_v\cdot\frac{\boldsymbol{F}}{m}\mathrm{d}v - \int_v f\frac{\boldsymbol{F}}{m}\cdot\nabla_v g d\boldsymbol{v} \tag{2.9}$$

$$= -\int_v f\frac{\boldsymbol{F}}{m}\cdot\nabla_v g d\boldsymbol{v} = -n\langle\frac{\boldsymbol{F}}{m}\cdot\nabla_v g\rangle \tag{2.10}$$

In the second step we have used that the first integral in (2.9) is equal to a sum over all the velocity components of three triple integrals:

$$\sum_{i=x,y,z}\iiint_{-\infty}^{\infty}\partial_{v_i}(g\frac{F_i}{m}f)\mathrm{d}v_x\mathrm{d}v_y\mathrm{d}v_z. \tag{2.11}$$

All these integrals end up in an evaluation of the type:

$$\left[g\frac{F_i}{m}f\right]_{v_i=-\infty}^{v_i=\infty}\iint_{-\infty}^{\infty}\mathrm{d}v_j\mathrm{d}v_k \tag{2.12}$$

with $j,k\neq i$, and since no particles with infinite velocity can exist, these integrals vanish in all cases. And also that, the second term vanishes if we assume that $\nabla_v\cdot F = 0$, this is, if the force does not depend on its corresponding velocity component. This is not only true for all forces not dependent on the velocity such as electric or gravitational forces but also for the magnetic force as $\partial(\epsilon_{i,j,k}v_jB_k) = 0$. Combining the results for (2.6), (2.8) and (2.9) we obtain:

$$\partial_t(n\langle g\rangle) + \nabla\cdot(n\langle g\boldsymbol{v}\rangle) - n\langle(\frac{\boldsymbol{F}}{m}\cdot\nabla_v g)\rangle = \left[\frac{\delta}{\delta t}(n\langle g\rangle)\right]_{coll} \tag{2.13}$$

where the term in the right hand side denotes the volumetric rate of change to g due to collisions. We designate (2.13) as the general transport equation. From this equation it is straight forward to derive momenta of the VDF. Let us take for example the zeroth order moment by choosing $g(v) = v^0 = 1$. In this situation we have the some clear identities such as; $\langle g \rangle = 1$, $\langle g\boldsymbol{v} \rangle = \langle \boldsymbol{v} \rangle = \boldsymbol{u}$ and therefore the zeroth order moment of the VDF is the common equation for particle number conservation:

$$\partial_t n + \nabla \cdot (n\boldsymbol{u}) = \left[\frac{\delta n}{\delta t}\right]_{coll} \tag{2.14}$$

Had we chosen some other constant g such as a mass or a charge we would have obtained equations for the conservation of these quantities which are formally equivalent. If we take $g(v) = \boldsymbol{v}^1 = \boldsymbol{v}$ we obtain and assume that the particle velocity can be decomposed in a fluid velocity and a random thermal velocity ($\boldsymbol{v} = \boldsymbol{u} + \boldsymbol{c}$):

$$\partial_t(n\boldsymbol{u}) + \nabla \cdot (n\boldsymbol{u}\boldsymbol{u} + n\langle \boldsymbol{c}\boldsymbol{c} \rangle) - n\boldsymbol{F} = \left[\frac{\delta(n\boldsymbol{u})}{\delta t}\right]_{coll} \tag{2.15}$$

Identifying $\langle \boldsymbol{c}\boldsymbol{c} \rangle$ as the pressure tensor $\mathcal{P}$ and we assuming our plasma is only subject to electromagnetic forces we have:

$$\partial_t(n\boldsymbol{u}) + \nabla \cdot (n\boldsymbol{u}\boldsymbol{u} + n\mathcal{P}) = n(\boldsymbol{E} + \boldsymbol{v} \times \boldsymbol{B}) + \left[\frac{\delta(n\boldsymbol{u})}{\delta t}\right]_{coll} \tag{2.16}$$

In a similar fashion we can obtain the second order moment which lead to energy conservation laws. This way we obtain the first three fluid equations for a species s [36]:

$$\partial_t n_s + \nabla \cdot (n_s \boldsymbol{u}_s) = S_c \tag{2.17}$$

$$\partial_t(m_s n_S \boldsymbol{u}_s) + \nabla \cdot (m_s n_s \boldsymbol{u}_s \boldsymbol{u}_s + \mathcal{P}_s) = q_s n_s(\boldsymbol{E} + \boldsymbol{u}_s \times \boldsymbol{B}) + \boldsymbol{F}_c \tag{2.18}$$

$$\partial_t\left(\frac{3}{2}p_s + \frac{1}{2}m_s n_s u_s^2\right) + \nabla \cdot \left[\left(\frac{3}{2}p_s + \frac{1}{2}m_s n_s u_s^2\right)\boldsymbol{u}_s + \boldsymbol{q}_s\right] = -\nabla \cdot (\boldsymbol{u}_s \mathcal{P}_s) + \boldsymbol{q}_s n \boldsymbol{u}_s \cdot \boldsymbol{E} + \mathcal{Q}_s \tag{2.19}$$

Where $\boldsymbol{q}_s$ represents the heat flux vector, and S_c, $\boldsymbol{F}_c$, and $\mathcal{Q}_s$ represent collisional contributions to particle number density, momentum and total energy of species s respectively. Moreover, $p_s = \text{trace}(\mathcal{P}_s)/3$.

This fluid formalism comes with a caveat, the closure problem. The n first fluid equations, even in their collisionless form, have $n+1$ unknowns, therefore the system itself in underdetermined. For example in equations (2.17)-(2.19) we need further information in order to relate the heat-flux vector $\boldsymbol{q}_s$ to lower moments of the VDF, this is known as a closure relation. In near-collisionless plasmas, information for the choice of a closure relation can come from either experimental data, for example the

knowledge of an isothermal behaviour by some species, or from kinetic simulations that can inform about the shape of the velocity distribution functions of the different species. Therefore, special care must be taken while choosing a fluid closure if one wants to obtain sensible results. Some common choices are the assumption of a Maxwellian VDF for the species s which renders a diagonal pressure tensor and a vanishing heat-flux vector, therefore the fluid equations become a closed, isotropic and adiabatic five moment model; the choice of a Fourier-type closure for the heat-flux vector for which we have an eight-moment model [42]. For collisionless but strongly magnetised species, such as the electrons a reasonable choice could be the Chew, Goldberger, Low model [43] where even without collisions the gas is thermalized by the small Larmor radius due to the strong Lorentz force, however this happens only in the direction perpendicular to the magnetic field leading to a diagonal but anisotropic pressure tensor an equation for the parallel internal energy and a closure relation for the heat-flux vector. Some of these models are employed in both fluid and fluid-kinetic codes.

In the following we obtain simpler models employing fewer momenta of the VDF than the ones described above exploiting the specific information we have for the expansion of plasma in a magnetic nozzle. These models are intended to be fast and able to give physical insight of the main dynamical behaviour of the different species involved in the expansion, however, we must emphasize that the models described above are more accurate at the expense of higher computational cost. The models presented in the following sections make no assumptions on the geometry of the model, this is, they can be adapted to either axisymmetric or planar geometry.

2.2 Two Dimensional Models

In this thesis all the models considered are quasi-neutral, this is $n_e = n_i$ everywhere in the domain. Moreover, these models are solved in two-dimensional geometries, either planar or axisymmetric. In the planar case we define a right-handed reference frame with the plane Oxy coincident with the exit plane of the plasma source, and the Oz axis pointing downstream. The plane under study is therefore the Oxz plane, and in the 2D expansion the plasma is infinite and uniform in the y direction. The plane Oyz is a symmetry plane, and thus only the upper half of the plane is simulated. Without loss of generality, $\boldsymbol{B}$ is taken to point axially downstream in this part of the domain. We introduce the Cartesian vector basis $\{\mathbf{1}_z, \mathbf{1}_x, \mathbf{1}_y\}$ and the magnetic vector basis $\{\mathbf{1}_b, \mathbf{1}_\perp, \mathbf{1}_y\}$, with $\mathbf{1}_\parallel = \boldsymbol{B}/B$ and $\mathbf{1}_\perp = \mathbf{1}_y \times \mathbf{1}_\parallel$.

On the other hand, for the axisymmetric case we define a frame of reference with the plane $Or\theta$ coincident with the exit plane of the plasma source, and the

Oz axis pointing downstream. The plane under study is therefore the Orz plane, and all quantities are assumed to be rotationally invariant ($\partial_\theta \to 0$). Hence the integration is formally two dimensional once an arbitrary azimuthal angle is chosen. In this case, we define the cylindrical vector basis $\{\mathbf{1}_z, \mathbf{1}_r, \mathbf{1}_\theta\}$ and the magnetic vector basis $\{\mathbf{1}_\parallel, \mathbf{1}_\perp, \mathbf{1}_\theta\}$, with $\mathbf{1}_\perp = \mathbf{1}_\theta \times \mathbf{1}_b$. In both cases the bases we have defined are right-handed and orthonormal. In the following the second component of our vector bases will be denoted with the letter r independently on the geometry of the problem while ξ will denote the third component, this is, y and θ in planar and axisymmetric geometries respectively.

The applied magnetic field $\boldsymbol{B}_a$ is generated by a set of ideal electric conductors w, each carrying an electric current I_w. The arrangement of these conductors and their electric currents is antisymmetric about the Oyz symmetry plane in the planar case and rotationally symmetric around the Oz axis in the axisymmetric case.

In the planar case the conductors will be a set of infinite wires carrying a current in the $\mathbf{1}_y$ direction and the sum of the I_w over all the wires equals zero. The magnetic stream-function of a single wire w is given by

$$\psi_{Bw} = -\frac{\mu_0 I_w}{2\pi} \ln \rho_w, \tag{2.20}$$

where ρ_w is the distance from the wire. Summing over the wire contributions we obtain the stream-function ψ_{Ba} of the applied field.

In contrast, in the axisymmetric case the conductor will be a single current loop with radius R_L and centered at the origin whose magnetic stream-function reads:

$$\psi_{Bl} = \frac{B_0 R_L}{2\pi} \sqrt{(R_L + r)^2 + z^2} [(2 - k^2)\boldsymbol{K}(k^2) - 2\boldsymbol{E}(k^2)], \tag{2.21}$$

with $k^2 = 4R_L r[(R_L + r)^2 + z^2]^{-1}$, $B_0 = B_z(0, 0)$ and $K(m)$ and $E(m)$ the complete elliptic integrals of the first and second kind respectively [20].

The applied magnetic field can be obtained from the magnetic streamfunction in a straightforward manner. Let us define a function $\zeta(r)$ such that $\zeta(r) = r$ in the axisymmetric case and $\zeta(r) = 1$ in the planar case. Then the magnetic field is given by the magnetic streamfunction as:

$$\frac{\partial \psi}{\partial z} = -\zeta(r) B_r, \qquad \frac{\partial \psi}{\partial r} = \zeta(r) B_z, \tag{2.22}$$

The plasma-induced magnetic field $\boldsymbol{B}_p$ has the streamfunction ψ_{Bp} given by Ampère's equation, which reduces to a manifestly elliptic partial differential equation:

$$\nabla^2 \psi_{Bp} = -\mu_0 j_y \equiv -\beta_0 B_{a0}^2 j_y, \tag{2.23}$$

where j_y is the out-of-plane plasma electric current and $\beta_0 = \mu_0/B_{a0}^2$ is the β parameter at the centerpoint of the thruster outlet, already normalized with n_0 and T_{e0}.

The total magnetic field $\boldsymbol{B}$ is the sum of the applied and plasma-induced ones, with $\psi_B = \psi_{Ba} + \psi_{Bp}$, and

$$\boldsymbol{B} \equiv \boldsymbol{B}_a + \boldsymbol{B}_p = \frac{1}{\zeta(r)} \nabla \psi_B \times \mathbf{1}_\xi. \tag{2.24}$$

With $\mathbf{1}_\xi$ the unit vector for the third dimension ξ. When $\beta_0 = 0$ the plasma-induced magnetic field $\boldsymbol{B}_p$ is negligible with respect to the applied one $\boldsymbol{B}_a$, and the total field coincides with the latter. Then, equation (2.23) may be dropped from the model.

Note that $\mathbf{1}_\perp \equiv \nabla\psi_B/(\zeta(r)B)$ and, for any single-variable function $f(\psi_B)$,

$$\nabla f = \frac{\partial f}{\partial \mathbf{1}_\perp} \mathbf{1}_\perp = \zeta(r) B \frac{\mathrm{d}f}{\mathrm{d}\psi_B} \mathbf{1}_\perp. \tag{2.25}$$

2.3 Electron Model

In this section we describe the model employed for the solution of the electron fluid. The model is based on the work by Ahedo and Merino in [20], which it extends. The collisionless limit of this model is the one employed in chapter 4, while the case where ionization and other collisions are taken into account is described in chapter 5.

To begin with, we start with the equations for continuity(2.17), momentum (2.18) and energy (2.19) conservation for the electron fluid. Experiments [44]-[45] have shown that electron thermodynamics can be well characterized by a polytropic relation and therefore we close the equations for the electron fluid with a relation for the temperature as $T_e = T_{e0}(n_e/n_{e0})^{\gamma_e}$, with this assumption the equation for the internal energy can be dropped. In addition, we will consider a drift-diffusive model for the electron fluid based on the fact that electrons in a typical magnetic nozzle scenario are highly sub-sonic $u_e \ll c_e$ and hence we drop the inertial terms from the electron momentum equation. This is, in fact, equivalent to retaining only zeroth-order Larmor radius effects.

With these assumptions, the equations for the electron fluid read:

$$\partial_t n_e + \nabla \cdot (n_e \boldsymbol{u}_e) = S_i, \tag{2.26}$$

$$0 = -\frac{T_{e0}}{n_{e0}^{\gamma_e - 1}} \nabla(n_e T_e) + e n_e \nabla\phi - e n_e \boldsymbol{u}_e \times \boldsymbol{B} - m_e n_e \nu_e \boldsymbol{u}_e \tag{2.27}$$

In the continuity equation (2.26) the term S_i represents plasma creation by ionization and ν_e represents the effective electron momentum collision frequency due to elastic

collisions (with ions and neutrals) and inelastic collisions (excitation, ionization). For the moment, we dismiss the collisional contribution to the electron momentum equation. In a latter section we will obtain the leading order corrections to the collisionless equations in order to justify this choice.

It is useful to note that for any polytropic species the following relation holds:

$$\frac{1}{n_e}\nabla(n_e T_e) = \frac{\gamma_e}{\gamma_e - 1} T_{e0} \nabla\left(\frac{n_e}{n_{e0}}\right)^{\gamma_e - 1},$$

and that we can write the electron velocity as function of its components in the magnetic vector basis as:

$$\boldsymbol{u}_e = u_{\parallel e}\mathbf{1}_b + u_{\perp e}\mathbf{1}_\perp + u_{\xi e}\mathbf{1}_\xi. \tag{2.28}$$

In a magnetic nozzle, electrons are strongly magnetized and therefore $u_{\perp e} \ll u_{\parallel e}, u_{\xi e}$ Taking all this into account we can write the conservation of momentum for electrons as:

$$\begin{aligned} 0 = &-\nabla\left\{\frac{\gamma}{\gamma - 1}\left[\left(\frac{n}{n_0}\right)^{\gamma-1} - 1\right] - \phi\right\} \\ &- B(u_{\parallel e}\mathbf{1}_b + u_{\perp e}\mathbf{1}_\perp + u_{\xi e}\mathbf{1}_\xi) \times \mathbf{1}_\parallel. \end{aligned} \tag{2.29}$$

Which can be written in terms of the thermalized potential H_e

$$H_e = \frac{\gamma_e}{\gamma_e - 1}\left[\left(\frac{n}{n_0}\right)^{\gamma-1} - 1\right] - \phi, \tag{2.30}$$

as

$$0 = -\nabla H_e - B(u_{\parallel e}\mathbf{1}_b + u_{\perp e}\mathbf{1}_\perp + u_{\xi e}\mathbf{1}_\xi) \times \mathbf{1}_\parallel.$$

The projection of this equation onto its components in the magnetic vector basis renders:

$$\frac{\partial H_e}{\partial \mathbf{1}_\parallel} = 0 \tag{2.31}$$

$$u_{\xi e} = \frac{-1}{B}\mathbf{1}_\perp \cdot \nabla H_e \tag{2.32}$$

$$u_{\perp e} = 0 \tag{2.33}$$

The out-of-plane electron velocity $u_{\xi e}$ can be computed from the map of ∇H_e and equation (2.25):

$$u_{\xi e}(\psi_B) = -\frac{1}{B}\frac{\partial H_e}{\partial \mathbf{1}_\perp} = -\zeta(r)\frac{\mathrm{d}H_e}{\mathrm{d}\psi_B} = -\zeta(r)H_e'. \tag{2.34}$$

This $u_{\xi e}$ results from the sum of the diamagnetic (i.e., pressure-driven) and $\boldsymbol{E} \times \boldsymbol{B}$ drifts, which are the only first-order drifts in the problem (and indeed, they scale as

$1/B$). The function H_e, its derivative H_e', and consequently $u_{\xi e}$, can be computed from the boundary conditions at $z = 0$ on each magnetic line. This computation can be done a priori, i.e. before solving the rest of the plasma problem. Observe that only one value of H_e may be imposed per magnetic line, and this restricts the set of valid boundary conditions elsewhere. Clearly, the parallel velocity of electrons is decoupled from the rest of the system of equations and will be obtained in the postprocessing stage by solving the parallel projection of the steady-state continuity equation:

$$\boldsymbol{B} \cdot \nabla \left(\frac{n u_{\parallel e}}{B} \right) = S_i. \tag{2.35}$$

The solution of the electron continuity equation is heavily influenced by the choice of boundary conditions. In the typical ranges of operation of a magnetic nozzle where ions are mildly magnetised, current ambipolarity i.e., $\boldsymbol{j} = 0$ can only be satisfied in a given section of the expansion. In a steady state situation in space operation where net zero charge in the spacecraft must be maintained, a natural choice is to impose ambipolarity in the nozzle throat, however, in certain situations in testing facilities it could be natural to impose ambipolarity in the downstream region of the plume. In the collisionless limit, this choice does not affect the expansion as, as explained before, electron continuity is solved after the solution of the ion-neutral equations. However, the collisional corrections that induce a perpendicular drift of the electrons with respect to the magnetic streamlines can be severely affected by this choice. Particularly, downstream ambipolarity reduces heavily the electron parallel velocity in the external part of the plume and, therefore, enhances electron cross transport subsequently increasing the divergence of the plume. In subsection 2.3.1 we explore the effect of this choice on electron and total currents.

2.3.1 Collisional corrections to electron momentum equation

The collisionless limit of electron momentum equation (2.29) allowed us to decouple its solution from the rest of the system leading to an algebraic solution [20]. In order the justify the choice of dismissing collisions in the electron momentum equation we come back to its collisional form (2.27) . Following an approach analogous to the one in the previous section 2.3 we arrive at the collisional form of equations (2.31)-(2.32) which read:

$$\frac{\partial H_e}{\partial \mathbf{1}_\parallel} = -B\chi^{-1}u_{\parallel e} \tag{2.36}$$

$$u_{\perp e} = \chi^{-1}u_{\xi e} \tag{2.37}$$

$$u_{\xi e} = \frac{-1}{B}\mathbf{1}_\perp \cdot \nabla H_e - \chi^{-1}u_{\perp e} = \frac{-1}{B}\mathbf{1}_\perp \cdot \nabla H_e - \chi^{-2}u_{\xi e} \tag{2.38}$$

Here one can appreciate clearly that collisions in the electron momentum equation act as corrections in powers of χ^{-1} to the collisionless case, with $\chi^{-1} = m_e\nu_e/eB$ the inverse of the Hall-parameter. Let us explore in more detail each equation separately. Equation (2.36) states that in the absence of collisions H_e is conserved along electron streamlines, collisions therefore act as a loss term for electron momentum along these streamlines. Equation (2.37) states, that electron collisionality induces a perpendicular velocity on the electron fluid that breaks the assumptions of perfect magnetization taken in [20], one key feature of this equation is that in a propulsive magnetic nozzle where electron azimuthal current is positive, collisional detachment of electrons from magnetic streamlines is always radially outwards [46]. Finally, in equation (2.38) collisions can be seen as an azimuthal momentum loss term due collisional drag for the otherwise conserved (along magnetic streamlines) azimuthal frequency $u_{\theta e}/\zeta$. Finally, Note that in equations (2.36) and (2.37) collisional corrections are of order χ^{-1} while in equation (2.38) they are of order χ^{-2}. In a typical magnetic nozzle scenario the inverse of the Hall parameter is in the range of 10^{-3}. In this high Hall-parameter regime the collisional correction to electron aimuthal momentum is regarded as negligible as it will be $\mathcal{O}(10^{-6})$ everywhere in the domain. The effect of these collisional corrections in an axisymmetric magnetic nozzle are explored further in chapter 5.

2.4 Ion Model

This section is devoted to the development of the ion models which are solved in chapters 4 and 5. These models are very similar and based on the ones exposed in [20]. Hereafter, we obtain the more general model that is solved in 5 and then, making further assumptions, we obtain the model solved in 4 and that was employed in [28].

Under the assumption that, for heavy species and particularly ions, the convection of thermal energy dominates over conduction the heat-flux vector in (2.19) vanishes. As a closure, we start by choosing a warm plasma model in which the equation for the internal energy of ions is retained. We remind that the balance law for the internal energy of some species α reads:

$$\partial_t\left(\frac{3}{2}n_\alpha T_\alpha\right) + \nabla\cdot\left(\frac{5}{2}n_\alpha T_\alpha \boldsymbol{u}_\alpha\right) = \boldsymbol{u}_\alpha \cdot \nabla n_\alpha T_\alpha + \mathcal{Q}_\alpha \tag{2.39}$$

where $\mathcal{Q}_\alpha$ includes collisional contributions to the internal energy and we have taken a zero-heat flux closure and a we have substituted the pressure tensor for a scalar pressure as corresponds to any Maxwellian species, the response of ions in a paraxial MN to non-Maxwellian features in their VDF was explored in [47]. Consequently, the transport equations for the ion fluid read:

$$\partial_t n_e + \nabla \cdot (n_e \boldsymbol{u}_i) = S_i, \tag{2.40}$$

$$\partial_t n_e \boldsymbol{u}_i + \nabla \cdot (n_e \boldsymbol{u}_i \boldsymbol{u}_i + \frac{1}{m_i} n_e T_i) = -\frac{e n_e}{m_i} \nabla \phi + \frac{e n_e}{m_i} \boldsymbol{u}_i \times \boldsymbol{B} + S_i \boldsymbol{u}_n + S_{CEX}(\boldsymbol{u}_n - \boldsymbol{u}_i) \tag{2.41}$$

$$\partial_t \left(\frac{3}{2} n_e T_i \right) + \nabla \cdot \left(\frac{5}{2} n_e T_i \boldsymbol{u}_i \right) = \boldsymbol{u}_i \cdot \nabla n_e T_i + S_i \left(\frac{3}{2} T_n + \frac{m_i}{2} (\boldsymbol{u}_i - \boldsymbol{u}_n)^2 \right) + S_{CEX} \left[\frac{3}{2} (T_n - T_i) + \frac{m_i}{2} (\boldsymbol{u}_i - \boldsymbol{u}_n)^2 \right] \tag{2.42}$$

Here the term S_{CEX} represents the volumetric rate for CEX collisions. The expressions for the rates of all collisions included in this study can be found in 5.A.

To normalize the equations we have used the ion mass m_i, the elementary charge e, the radius of the plasma exit R. We also use the properties in the centre of the nozzle n_0 and T_{e0} to normalize all densities and temperatures.

Although, experiments [48] and simulations have shown that ion temperature increases downstream due to late ionization, the temperature of electrons is several orders of magnitude larger than that of the ions in electron driven MNs. Electron temperatures are in the range of tens of eV [49], [50], [45] while ions show lower temperatures of the order of hundreds of Kelvin [51]. For this reason, in a first approximation one could consider the ion fluid to be completely cold by neglecting its internal energy. Moreover in good vacuum conditions the mean free path of collision with neutral atoms should be small enough to neglect collisional terms with them. In such conditions the fluid equations of the ions can be reduced to:

$$\partial_t n_e + \nabla \cdot (n_e \boldsymbol{u}_i) = 0, \tag{2.43}$$

$$\partial_t n_e \boldsymbol{u}_i + \nabla \cdot (n_e \boldsymbol{u}_i \boldsymbol{u}_i) = -n_e \nabla \phi + n_e \boldsymbol{u}_i \times \boldsymbol{B} \tag{2.44}$$

This is the ion model solved in chapter 4 and in [28] and is equal to the one developed by Ahedo and Merino for the Dimagno code in [20].

2.5 Neutral Model

In some cases the dynamics of neutral atoms might play an important role in the performance and the operation of the magnetic nozzle [52, 53] and in other electric

propulsion devices [54]. The neutral model included in the studies shown in chapter 5 assumes that the neutral VDF is, as that of the ions, maxwellian. This assumption is supported by the fact that the residence time of neutrals is much longer than that of the ions in virtue of their lower thermal pressure. Therefore their internal energy is given by (2.39) and their transport equations:

$$\partial_t n_n + \nabla \cdot (n_n \boldsymbol{u}_n) = -S_i, \tag{2.45}$$

$$\partial_t n_n \boldsymbol{u}_n + \nabla \cdot (n_n \boldsymbol{u}_n \boldsymbol{u}_n + p_n) = -S_i \boldsymbol{u}_n + S_{CEX}(\boldsymbol{u}_i - \boldsymbol{u}_n) \tag{2.46}$$

$$\begin{aligned} \partial_t \left(\frac{3}{2} n_n T_n\right) + \nabla \cdot \left(\frac{5}{2} n_n T_n \boldsymbol{u}_n\right) &= \boldsymbol{u}_n \cdot \nabla n_n T_n \\ &\quad -S_i \frac{3}{2} T_n + S_{CEX}\left[\frac{3}{2}(T_i - T_n) + \frac{1}{2}(\boldsymbol{u}_i - \boldsymbol{u}_n)^2\right] \end{aligned} \tag{2.47}$$

In order to reduce the dimensionality of the system one can make further assumptions, in partiular we assume, that neutrals are introduced in the domain without any out-of-plane velocity, ($u_{\xi n} = 0$), hence, the only mechanism that could induce a rotational velocity in the neutral fluid is the exchange of azimuthal momentum with ions via CEX collisions and, as the swirl current (following the notation in [20]) in electron driven nozzles tends to be small, we disregard the azimuthal component of the neutral momentum equation.

2.6 Self Induced magnetic field

Plasmas are a complex system in which a plethora of physical phenomena take place. EPTs are usually operated in a low β parameter regime in which the plasma currents are small compared to the ones generating the MN. For this reason, we can usually disregard the contribution of their induced magnetic field on the total one. However, in the downstream region in which the applied field decreases, the effect of plasma induced fields become larger opening the magnetic field lines, creating a separatrix line downstream and allowing plasma detachment [46, 55]. In closed line configurations such as the Magnetic Arch Thruster [56, 28] the self-induced magnetic field is expected to change the topology of the applied one by stretching the lines to and opening the arch topology. To evaluate this effect we, iteratively, solve the Ampere-Maxwell equation which together with Gauss' law governs the behaviour of the magnetic field:

$$\nabla \times (\mu^{-1} \boldsymbol{B}_p) = -\partial_t \boldsymbol{D} + \boldsymbol{J} \tag{2.48}$$

$$\nabla \cdot \boldsymbol{B}_p = 0 \tag{2.49}$$

where $\boldsymbol{D}$ is the displacement vector and $\boldsymbol{J}$ is the electric current. In the static limit we can drop the time derivative of the displacement current and therefore the plasma-induced magnetic field is only determined by the electric currents in the plasma. As the magnetic field is divergence free, it can be written as the rotational of a vector field which is known as the magnetic vector potential $\boldsymbol{A}$. We can then write:

$$-\nabla \cdot (\mu^{-1} \nabla \boldsymbol{A}) = \boldsymbol{J} \tag{2.50}$$

where we have used the gauge freedom in the vector potential to fix $\nabla \cdot \boldsymbol{A} = 0$, this choice is known as Coulomb's gauge. If we are only interested in the in-plane components of the magnetic field this reduces to a scalar problem for the out-of-plane component of the magnetic vector potential that can be written as:

$$-\nabla \cdot (\mu^{-1} \nabla A_\xi) = J_\xi \tag{2.51}$$

The elliptic nature of the Poisson equation for the magnetic potential (2.51) poses a problem for the simulation of static magnetic fields for unbounded domains. Far away from any sources, the gradient of A_ξ should decay so that its gradient is identical to zero. In fact, thanks to the gauge freedom of the potential, one could define A_ξ so that it vanishes away from currents. In practice, to simulate such scenarios one is forced to solve equation (2.51) in a very large domain whose boundaries are set to an homogeneous boundary condition. This is problematic in a coupled problem as the one we deal with here as solving A_ξ in a bigger domain would imply solving the plasma equations in the same domain with the subsequent numerical cost. In order to tackle this problem we add an anisotropic Perfectly Matched Layer (PML) to the boundaries of the computational domain following [57]. This PML can be seen as an absorbing region in which the magnetic potential decays much faster than in free space without introducing new currents; this way the transition to infinity can be compressed in a smaller domain.

Chapter 3

POSETS: Plume SOlver for Electrodeless Thruster Systems

This chapter describes the Plume SOlver for Electrodeless Thruster Systems (POSETS) that has been built during the development of this thesis. The code is composed of a set of libraries for the simulation of the expansion of magnetized plasmas. The code includes several utilities that are described in the following, between these utilities there is the possibility of building non-uniform unstructured meshes, the solution of several fluid models both in planar and axisymmetric geometries with an imposed magnetic field and the iterative solution of the plasma expansion taking into account its self induced magnetic field. The fluid solver included in the code is based on the Discontinuous Galerkin finite element method (DGFEM). This method combines the advantages of the Finite Element Method (FEM), such as ease of use in non-uniform meshes and hp-adaptivity with the advantages of Finite Volume Methods (FVM) such as the handling of conservation laws and the exact local conservation of physical magnitudes.

3.1 Design goals and capabilities

POSETS is intended to be a fast simulation code to assess several physical mechanisms taking place in magnetic nozzles. Therefore, the main goal of the code is the simulation of magnetised plasmas in the parameter range that characterizes of EPTs. The code has the following capabilities:

- Meshing:
  - Create irregular meshes on rectangular domains with specified non-constant cell size.

- Fluid Solver:
  - Definition of fluid boundary conditions such as supersonic inflow, outflow, or wall.
  - Definition of the semi-discrete weak form of the problem and specification of initial conditions.
  - Time evolution and solution to steady state equations.
  - Iterative solution of the fluid problem with self induced magnetic field.
- Magnetic field solver:
  - Imposition of anisotropic perfectly matched layers in the domain boundary for the simulation of unbounded domains.
  - Imposition of Dirichlet or Newman at desired boundaries.
  - Solution of Poisson equation for the magnetic vector potential in 2D.
- Postprocess:
  - Interpolation into `Numpy` arrays for plotting.
  - Evaluation of volume and surface integrals for conservation of different magnitudes.

3.2 Numerical Integration

3.2.1 The DGFEM weak form

The Discontinuous Galerkin (DG) method was first introduced in 1973 by Reed and Hill to solve the linear transport equation in the context of neutron transport [58]

$$\sigma u + \nabla \cdot (\boldsymbol{a} u) = f. \tag{3.1}$$

In the 90s the Discontinuous Galerkin method gained prominence as it was further extended to non-linear hyperbolic conservation laws and multidimensional systems of conservation laws by Cockburn and Shu [39].

Discontinuous Galerkin methods are rooted in a combination of ideas coming from Finite Volume methods and Finite Element (or Spectral Element) methods. Let's briefly summarize the discretization process of an hyperbolic system of balance laws by the DG method. Let us write this hyperbolic system as:

$$\partial_t \boldsymbol{q} + \nabla \cdot F(\boldsymbol{q}) = \boldsymbol{f}, \tag{3.2}$$

here $\boldsymbol{q}$ is the vector of conserved variables F will be the flux function of the system and $\boldsymbol{f}$ is a generic forcing term. To obtain the DG discretization of this system let us first discretize the domain Ω in a set of cells D_k and consider that, in each cell of the discretization, we can write an approximation to the solution vector of the system q as:

$$\boldsymbol{q}(\boldsymbol{x},t) \simeq \boldsymbol{q}_h(\boldsymbol{x},t) = \sum_{i=0}^{p} \boldsymbol{\alpha}_i(t)\boldsymbol{\phi}_i(\boldsymbol{x}), \tag{3.3}$$

where $\boldsymbol{\phi}$ is a set of basis functions defined in a single cell D_k and $\alpha_i(t)$ is a set of time-dependant expansion coefficients, lastly N is the the number of elements in our function basis. Armed with these definitions we take our system of conservation laws and multiply by a set of test functions ψ_i which using the Ritz-Galerkin projection is contained in the same function space as the basis functions, and indeed, $\psi_i = \phi_i$. The choice of this function space will be discussed in more detail later in the text, however, it is key to point out that here we do not impose continuity between contiguous basis functions. After multiplication by the test function, we integrate over the volume of the cell D_k to obtain:

$$\int_{D_k} \partial_t q_{i,h}\phi_i \mathrm{d}x + \int_{D_k} (\nabla_j F_{ij})\phi_i \mathrm{d}x - \int_{D_k} f_i\phi_i \mathrm{d}x = 0 \tag{3.4}$$

Where Einstein's notation for summation is being used and we have dropped dependency on space, time and conserved variables for the sake of clarity. Integrating by parts the second term in (3.4) we obtain:

$$\int_{D_k} \partial_t q_{i,h}\phi_i \mathrm{d}x - \int_{D_k} F_{ij}\nabla_j\phi_i \mathrm{d}x + \int_{\partial D_k} F_{ij}\phi_i n_j \mathrm{d}s - \int_{D_k} f_i\phi_i \mathrm{d}x = 0 \tag{3.5}$$

Here ∂D_k is the boundary of element D_k and $\boldsymbol{n}$ is the outward pointing normal at each of the facets of the element. Summation over all elements of the discretization leads to:

$$\int_{\Omega} \partial_t q_{i,h}\phi_i \mathrm{d}x - \int_{\Omega} F_{ij}\nabla_j\phi_i \mathrm{d}x + \int_{\Gamma_{ext}} \hat{F}_{ij}\phi_i n_j \mathrm{d}s + \int_{\Gamma_{int}} \hat{F}_{ij} n_j(\phi_i^+ - \phi_i^-)\mathrm{d}s - \int_{\Omega} f_i\phi_i \mathrm{d}x = 0 \tag{3.6}$$

Here $\Gamma_{ext} = \partial\Omega$ is the external boundary of the domain Ω and Γ_{int} is the set of internal boundaries between facets of the discretization, therefore $\Gamma_{int} = \{\partial D_k : \partial D_k \notin \Gamma_{ext}\}$, and n_j is the j-th component of the outward facing normal vector $\boldsymbol{n}$. At this point we must remember that no restriction of continuity is imposed on the solution in the interfaces between cells, consequently one must be careful when evaluating the third and fourth term in equation 3.6, let us then take a closer look at them. Both the third and fourth term contain the object $\hat{F}_{ij}$ which is usually called the numerical trace trace of the flux F_{ij}. This numerical trace appears due to the fact that the flux does not have a uniquely defined value in the interface between two contiguous cells if the solution is discontinuous there. To assign a value to this numerical trace we use a so-called numerical flux which is just an

approximate Riemann solver for the Riemann problem between the two cells. Some of the most commonly employed numerical fluxes are local and global Lax-Friedrichs flux, the Roe flux and the Harten-Lax-van Leer, Einfeldt (HLLE) flux [59, 60]. Nevertheless, it is usually argued that the choice of the numerical flux does not have a significant impact in the discretization for high order numerical schemes [61, 62]. In the following we use the local Lax-Friedrichs flux:

$$\hat{F}_{ij}(\boldsymbol{q}^+, \boldsymbol{q}^-) = \frac{1}{2}(F_{ij}(\boldsymbol{q}^+) + F_{ij}(\boldsymbol{q}^-)) + \frac{\alpha}{2}(\boldsymbol{q}^+ - \boldsymbol{q}^-) \tag{3.7}$$

with α computed as the maximum of all eigenvalues of the normal flux Jacobian $(\nabla\mathcal{F} \cdot \mathbf{1}_n)$ evaluated in each side of the facet. With this definition we can write the third term in 3.6 as:

$$\int_{\Gamma_{ext}} \hat{F}_{ij}(\boldsymbol{g}, \boldsymbol{q}^-)\phi_i n_j ds \tag{3.8}$$

where $\boldsymbol{g}$ is the prescribed boundary condition in the external facets.

3.2.2 Discretization of the parabolic terms in the energy equation

When considering the energy equation of ions and neutrals is we have introduced some terms that are not fully conservative as the evaluation of the right hand side in equations (2.42) and (2.47) requires the evaluation of gradients of the pressures of ions and neutrals respectively. These terms, while of minor relevance (the temperatures of ions and neutrals are orders of magnitude below that of electrons), cannot be adequately evaluated with the current DG discretization, as elements are not continuous across cell boundaries. In this work we instead project the pressure of ions and neutrals onto a continuous function space of order 2 and its gradient is then evaluated in this space. The numerical tests in subsection 3.4.6 verify the suitability of this approach, and show that this projection step recovers the expected convergence of the solution with element order p and element size h.

3.2.3 Choice of Finite Element Family

As stated before, one key element to the discretization of the system of equations is the basis functions used. In this sense it is common to define two types of DG methods, *Modal-DG* and *Nodal-DG* methods. In the former, the solution in equation 3.3 is represented by local sums of modal coefficients multiplied by a set of polynomials, in this case ϕ_i is usually chosen to be a set of orthogonal polynomials such as the Legendre polynomials. On the other hand, nodal DG methods reconstruct the solution by interpolation on a series of nodes , therefore, ϕ_i is usually a set of Lagrange polynomials defined over a set of nodes, for further discussion on these possible choices see [63]. In the case of this work we choose the latter Nodal

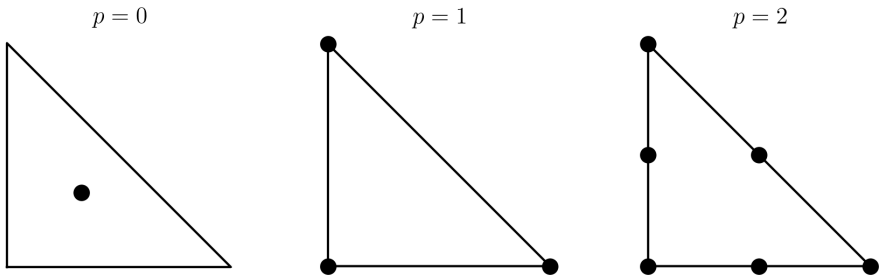

Figure 3.1: Position of nodal degrees of freedom for different order elements in a reference triangle.

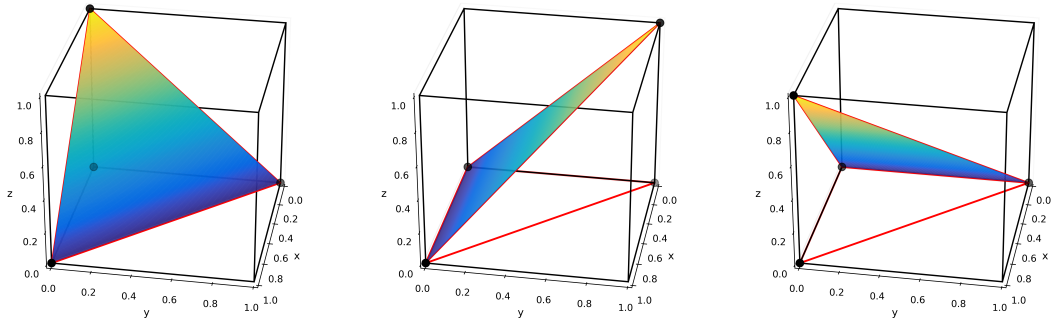

Figure 3.2: Lagrangian basis functions of order $p = 1$ on a reference triangular element.

basis, the position of the nodes of the Lagrangian basis is depicted in figure 3.1 for elements of order 0, 1 and 2 defined on a reference triangle.

An order 0 discretization has one degree of freedom per cell and its node is chosen to be located at the centre of the cell. One degree of freedom per cell creates a piecewise constant polynomial basis that renders a discretization equivalent to a finite volume method (FVM) where the value of the function at the node is equal to the the cell average of said FVM. A $p = 1$ discretization uses 3 nodes and, therefore, piecewise linear polynomial functions as its basis; this basis functions are depicted in figure 3.2. Finally a $p = 2$ discretization uses 6 nodes per triangular cell and a set of six quadratic functions as a base.

The key feature of the DG method is the fact that it does not require any continuity between contiguous elements, therefore the communication between cells happens only through the numerical flux that is usually chosen to only take into account contributions from the nearest neighbours allowing for a compact stencil, a property that makes DG methods very interesting for parallelization purposes.

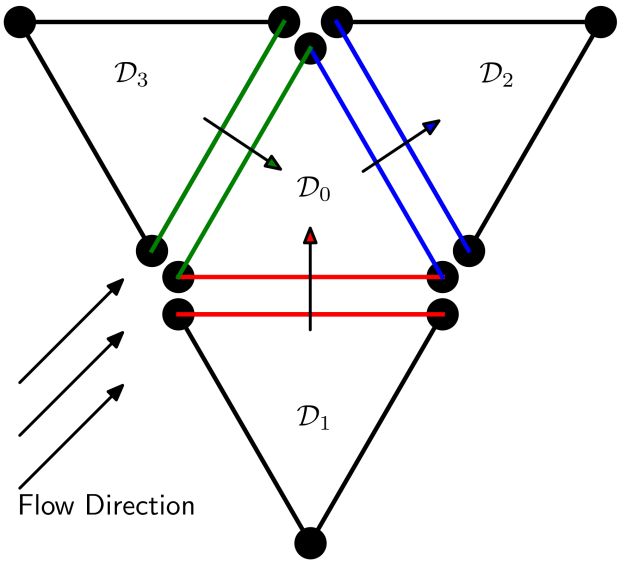

Figure 3.3: Example of inter-cell communication via the numerical fluxes. The black arrows, represent the direction of the flux, for example in an external 'ghost' cell and the coloured arrows represent the interelement flux that communicates cell $\mathcal{D}_0$ with its nearest neighbours.

3.2.4 Temporal Evolution

DG methods can be evolved in time using different schemes including space-time discretizations [64], such as forward/backward Euler methods or Runge-Kutta methods. The *POSETS* code comprises three different propagators, two of them being explicit, the forward Euler and the Strong Stability Preserving Runge-Kutta scheme(SSPRK) and one implicit, the backward Euler method. Runge-Kutta Discontinuous Galerkin methods (RKDG) were introduced by Cockburn and collaborators in a series of five papers from 1987 to 1998, there they developed these kind of schemes for 1D scalar conservation laws to multidimensional systems of conservation laws and proved them to be stable when a SSPRK of order $p+1$ was used on a discretization with polynomials of order p. For this reason we use from now on a three-stage strong-stability-preserving Runge-Kutta method by Shu and Osher [65]. The time step is chosen to be:

$$\Delta t = \frac{0.5}{2p+1} \min_j \frac{h_j}{|a_j|} \tag{3.9}$$

Where, h_j and a_j are the cell size and the maximum wave-speed at cell j respectively. This is a rather conservative value as the CFL number necessary for L_2 stability is close to $1/(2p+1)$ [66, 67].

In reality and in some of our problems the time-step can be much higher than

that. This is due to the fact that the velocity restriction is usually the one imposed by the ion fluid which is the one with the shortest time-scale. For this reason, when the simulations include both ions and neutrals and after a sufficient amount of time for which the ions are fully expanded, the time step is increased up to 10 times the initial time-step as the characteristic velocity of the neutrals is roughly ten times smaller than that of ions in our simulations.

3.2.5 Shock-Capturing

A simple energy analysis on the discretization 3.6 shows that the DG method is stabilized by the discontinuities between cells. This is, the second term on 3.7 in the presence of discontinuities between cells acts like a diffusive term that stabilizes the solutions in the presence of shocks. However, it can be shown that this natural dissipative mechanism introduced through the jump terms is only sufficient to stabilize the solution in the presence of shocks when piecewise constant (i.e. $p = 0$) discretizations are used. When higher order discretization are used, one may need to introduce further dissipation to obtain stable solutions. In our case, the stabilization mechanism chosen is that introduced by Hartmann and Houston [40]. This stabilization mechanism consists in the introduction of artificial viscosity in the discretization in the locations where the solution has higher gradients. In practice, this reduces to the appearance of a so-called shock capturing term in the discretization 3.6, this shock capturing term can be written as:

$$\int_{\Omega} \varepsilon \nabla \boldsymbol{q}_h \cdot \nabla \boldsymbol{\phi} \mathrm{d}\boldsymbol{x}. \tag{3.10}$$

Here, ε is the artificial viscosity matrix defined by:

$$\varepsilon = C_\varepsilon h^{2-\beta} |\nabla \cdot F(\boldsymbol{q_h})| I_d \tag{3.11}$$

where C_ε and $\beta \in (0, 1/2)$ are positive constants and I_d is the d-dimensional unit matrix. In the results shown in chapters 4 and 5 numerical diffusion was not added as the solutions where stable. However, this might be mandatory in time-resolved simulations with stronger shocks as exemplified in 3.4.1.

3.2.6 Finite Element Weak Form of Elliptic Problems

The DGFEM method is particularly well-suited for convective or convection-dominated problems. One of the requirements of our code is the solution of the Poisson equation for the magnetic vector potential in order to obtain the plasma-induced magnetic field. This problem is clearly of elliptic nature, for this reason, we solve it with a

standard finite element scheme using continuous Lagrangian elements. The obtain the weak form of this problem we start by writing the Poisson equation of the form:

$$-\nabla \cdot (D(\boldsymbol{x})\nabla q(\boldsymbol{x})) = f(\boldsymbol{x}). \tag{3.12}$$

Here $D(\boldsymbol{x})$ is a diffusion matrix which can be considered a scalar if the medium being treated is isotropic; in the case of the Poisson equation for the magnetic vector potential the diffusivity is equal to the inverse of the magnetic permeability.

Now we take 3.12 and multiply it by a test function ϕ contained in the space of Lagrange polynomials of order p and integrate over the full domain. Note that in this case we do enforce continuity between elements and therefore, the number of degrees of freedom for a problem with the same number of cells is greatly reduced in comparison with the case in which discontinuous Lagrange elements are used. After this we integrate over the whole domain and apply integration by parts on the result to get rid of second order derivatives to obtain:

$$-\int_\Omega \nabla \cdot (D\nabla q)\phi \mathrm{d}\boldsymbol{x} = \int_\Omega f\phi \mathrm{d}\boldsymbol{x} \tag{3.13}$$

$$\int_\Omega D\nabla q \cdot \nabla\phi \mathrm{d}\boldsymbol{x} - \int_{\partial\Omega} (\boldsymbol{n} \cdot D\nabla q)\phi \mathrm{d}s = \int_\Omega f\phi \mathrm{d}\boldsymbol{x} \tag{3.14}$$

Here the second term is responsible for the implementation of the Newmann boundary conditions in the part of the domain where it is needed, this part of the boundary is designated by Γ_N. On the other hand, Dirichlet boundary conditions are enforced simply by taking the test function equal to zero in the parts of the boundary Γ_D where these must be imposed [68], with this choice the second term vanishes on the Dirichlet boundary.

3.3 Numerical Implementation

3.3.1 Finite Element Libraries

In order to implement the discretizations described above, one could take two possible paths, one is to implement the whole assembly of the discretization of the problem in a given programming language of choice. However, the assembly of the matrix problem emerging from a finite element discretization is rather complex. First, it involves mapping each element in the mesh of the computational domain to a reference element where basis functions and quadrature rules are defined. Then, local stiffness matrix and load vectors are computed and become entries of the global matrix of the bilinear form and the RHS term. Additionally, one must enforce the

desired boundary conditions and solve the resulting linear problem by either iterative method or matrix inversion. This process, which is common in most FEM libraries, involves $\mathcal{O}(10^4)$ lines of code and is therefore necessarily a collaborative effort. For this reason, the POSETS code is based on the open-source library FEniCS [69]. FEniCS is one of the many freely available finite element libraries (`deal.ii` [70], `DUNE`[71], `MFEM`[72], `Gridap`[73], `Trixi.jl` [74], etc.) However FEniCS stands out for both its Python bindings and the possibility of using the Unified Form Language (UFL) to write weak-forms for PDEs in a manner that closely resembles that of mathematical notation. For this reasons the POSETS code is based on FEniCS.

3.3.2 Code Structure

POSETS' architecture is intended to be easily extendable with new physics. Thus, the implementation of the weak forms, the stabilization algorithms, the time stepping and all other mathematical aspects are separated from the modules that implement the different physical models. As explained before, the code is based on the FEniCS environment and, as a matter of fact, it can be understood as a higher level of abstraction that uses FEniCS' Unified Form Language (UFL) in order to write DGFEM discretizations for plasma flows and solves them using the solvers included in FEniCS. Several solvers can be used depending on the setting of the problem, for linear systems this includes PETSc's built in LU solver, UMFPACK, GMRES, and others. Non linear problems are solved via Newton iteration. In the low level FEniCS includes C++ classes for finite element computations but allows the user to work using mostly its Python interface. For the postprocesing stage the code mainly uses Numpy and Matplotlib for their widespread use. The list of modules included in the POSETS code is the following:

- `MeshModule`
  - `MeshCreator.py`: Creates a two-dimensional irregular unstructured meshes prompting Gmsh[75].
  - `MeshReader.py`: Transforms `.msh` meshes into FEniCS readable `.xdmf` meshes.
- `PhysicalModels.py`: Contains the base class for the model employed. This class defines the system of equations to be solved by defining the physical flux F and the forcement term $\boldsymbol{f}$ appearing in equation 3.2 for each different model. It also defined the characteristic velocities of the problem and its boundary conditions. Parent class to ones defined in:
  - `Plasma2D.py`: Module containing the model for the two-fluid model solved in chapter 4.

  - `Plasma_2D_energy.py`: Module containing an extension of the previous model considering the internal energy equation for the ions.
  - `Plasma_2D_neutrals.py`: This module contains a three-fluid model including warm, adiabatic and isentropic ions and neutrals.
  - `Plasma_2D_neutrals_energy.py`: This module contains the three fluid model considered in chapter 5.

- Thermodynamic Models: In these files we define classes for each species containing their non-dimensional thermodynamic properties such us temperatures and sonic speeds.
  - `Electrons.py`
  - `Neutrals.py`
  - `Ions.py`

- `BFields.py`: Computes analytically the imposed magnetic field and the magnetic stream-function produced by a set of conductors.

- `B_induced.py`: Contains a function `self_B` that computes the self induced magnetic field of the solution.

- `Collisions.py`: This contains the class `CollisionModels` that defines methods for the computation of the adimensional collision frequencies and other properties for the different collisions included in the model.

- Discretization:
  - `WeakForms.py`: Defines volume and surface integrals for the different terms appearing in the discretization 3.6.
  - `NumericalFluxes.py`: This module contains the definition of different numerical fluxes employed in the discretization.

- `MathAux.py`: Defines useful mathematical functions such as maximum, maximum absolute value, etc. without branching.

- `Propagators.py`: Definitions for the different time-stepping procedures implemented, namely: Forward and Backward Euler and third order SSPRK.

- `Simulations.py`: This module defines a `Simulation` class with methods that allow to easily call the different simulation strategies such us use of time integrators, solving steady state equations, refining the mesh and others.

- Postprocess:

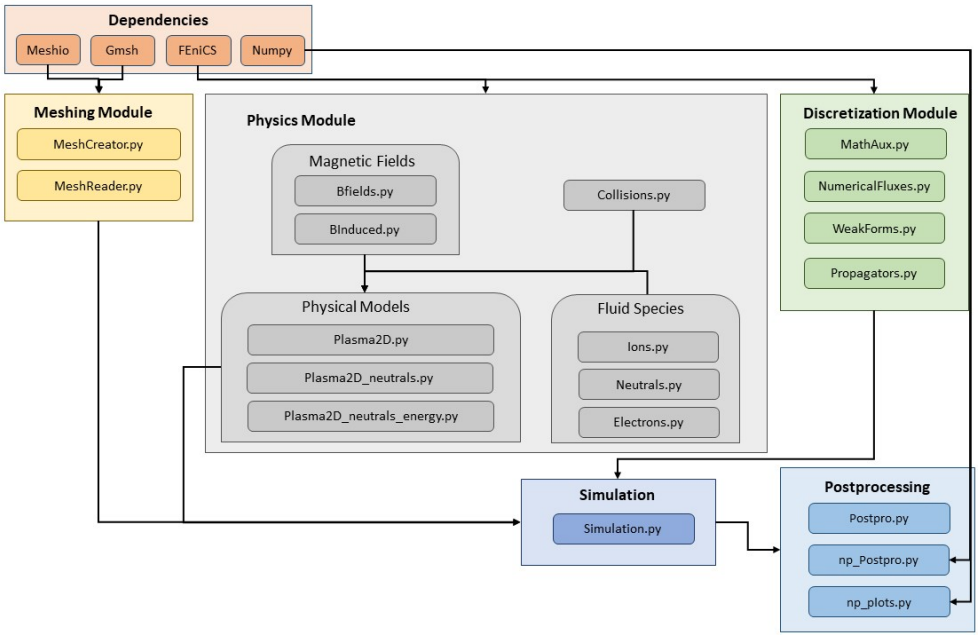

Figure 3.4: Structure of the `POSETS` code.

- `PostProc.py`: This module contains several useful functions to perform preliminary postprocessing of the solutions such as computing fluxes through the boundaries and others.
- `np_postproc.py`: Is in charge of obtaining `Numpy` arrays from the `FEniCS` solution in order to analyze them and plot them.
- `np_plots.py`: Defines functions to plot some typical plasma variables from the arrays proportioned by `np_postproc.py`.

The architecture of the code is illustrated in figure 3.4, there, the arrows indicate functional dependency. The typical workflow is seen in the figure from the upper-left corner to the lower-right corner, this is, one can create a script which loads all the different packages to first call the meshing module and create the required mesh. Then, one defines the `PhysicalModel` needed defining the different physical parameters such as the number of species and the types of collisions to be included. Finally, a time propagator and a numerical flux are chosen. This information is provided to a simulation object which is inherits from the `simulation` class the methods to solve the time evolution and the steady state solution to the discretization. The solution can be saved into an `.xdmf` file which is latter read and analysed using the functions included in the post-processing module.

3.4 Verification Tests

In order to check the correct functioning and integration of the different components of the code, several tests have been performed on them. These tests are based on

known analytical solutions or numerical solutions of the established DIMAGNO [20] code. Table 3.4 summarizes the major verification tests performed on the code. The fist two tests are purely fluid-dynamic, this is, the fluids are not magnetised and therefore the right-hand side of the conservative system is identical to zero. The following two tests verify the correct interaction of the LHS and RHS of the conservative system. Finally, the behaviour of the solver for the self-induced magnetic field is checked.

Test name	Success criterion
Shock Tube	Matching to analytical solution of an isentropic 1D shock-tube
Prandtl-Meyer Expansion	Correct convergence to analytical Mach number after a Prandtl-Meyer expansion.
Planar Plasma Column	Expected zero radial momentum up to tolerance, correct convergence to analytical solution.
Magnetic Nozzle Expansion	Matching to Dimagno's Solution
Double Infinite conducting wire	Matching to analytical solution.

3.4.1 Sod's shock tube problem:

The problem of the expansion of a gas in a unidimensional tube is one of the most common problems in compressible gas dynamics and a typical textbook example on Riemann Problems. The simulation consist of a tube filled with gas closed in both extremes. The gas inside the tube is initialized with a discontinuity in the middle, that separates the left state $(\rho_l, u_{zl}) = (1.0, 0.0)$ and the right state $(\rho_r, u_{zr}) = (0.125, 0.0)$. With time evolution this problem develops a left rarefaction wave and a right moving shock wave [76]. In figure 3.5 we show the numerical solution to this problem using different order polynomials. In order to avoid spurious oscillations in the solution the shock-capturing numerical diffusion scheme (3.10) was included in the simulations with $p \neq 0$ as the diffusion introduced by the Lax-Friedrichs flux does not suffice to stabilize the solution in these cases. In both cases $C_\varepsilon = 0.01$ and $\beta = 0$ where used. In order to show the effect of this stabilization mechanism we show in figure 3.6 the solution with polynomials of order one without stabilization (figure 3.6 a) and with stabilization (figure 3.6 b), clearly the stabilized solutions shows great reduction in the Runge-Gibbs phenomenon around discontinuities while maintaining sub-cell resolution of the shock and maintaining high accuracy away from it.

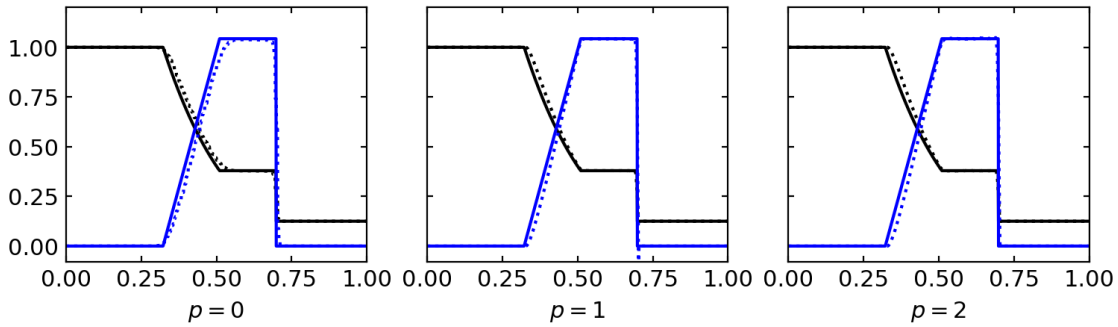

Figure 3.5: Density and velocity solution to Sod's shock tube problem after 0.15 units of elapsed time. In all plots the solid lines represent the analytical solution for density (in black) and velocity (in blue) while the dashed line represents the numerical solution for polynomials of order 0, 1 and 2 from left to right. These three cases were obtained using a mesh with 128 elements.

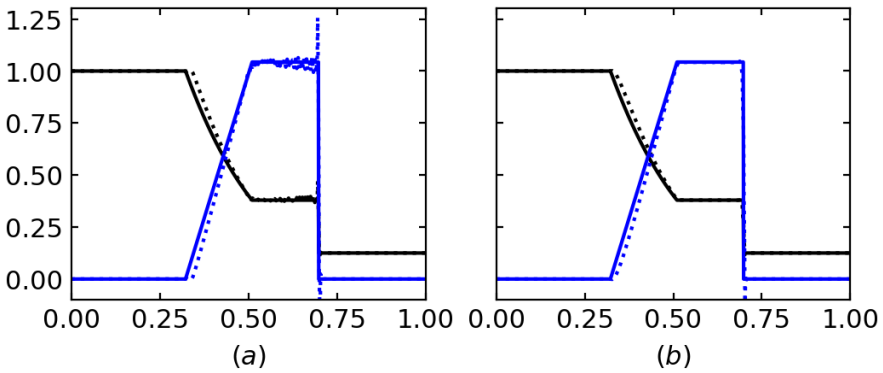

Figure 3.6: Example of the stabilization mechanism using polynomials of order one. The stabilized solution (right) shows decreased oscillations particularly in the velocity field.

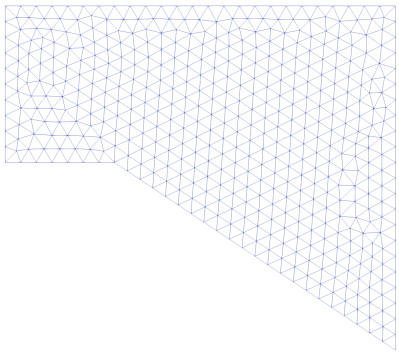

Figure 3.7: Mesh used for the Prandtl-Meyer expansion test.

3.4.2 Prandtl-Meyer Expansion:

The solver we employ is two dimensional, therefore it is necessary to test it in a scenario closer to that of the application of the code. To this end we solve the typical Prandtl-Meyer expansion of a supersonic flow into a convex corner.

The solution to this problem consists in two distinct areas, the low Mach number area with prescribed inlet boundary conditions and the high Mach number area after the corner. These two areas are connected by an expansion fan consisting of an infinite number of expansion waves with increasing Mach number and decreasing density. The value of the final Mach number can be written in terms of the turn angle and the incoming Mach number as:

$$\theta = \nu(M_2) - \nu(M_1) \tag{3.15}$$

Where ν is the Prandtl-Mayer function:

$$\nu = \sqrt{\frac{\gamma+1}{\gamma+1}} \arctan \sqrt{\frac{\gamma-1}{\gamma+1}(M^2-1)} - \arctan \sqrt{M^2-1} \tag{3.16}$$

As a test case we use a turning angle of $\theta = 2/3$ radians with an incoming Mach number of 1.1 and unit density. Solving M_2 from equations 3.15 and 3.16 with an adiabatic coefficient of $\gamma = 1.4$ gives a Mach number of ~ 2.33 after the expansion. This problem is solved on an unstructured mesh shown in figure 3.7.

In order to check the correct convergence of the simulation we choose a functional of the solution and compare its analytical value against that obtained in the simulation. The functional chosen in this case is the value of the Mach number after the expansion which is calculated analytically as explained before and sampled in the simulation in a point after the shock. Then we define the quadratic error as $(\mathcal{F} - \mathcal{F}_h)^2$ with $\mathcal{F}$ the analytical functional and $\mathcal{F}_h$ the numerical one. With these definitions the problem is solved for multiple mesh sizes and polynomial orders 0 and

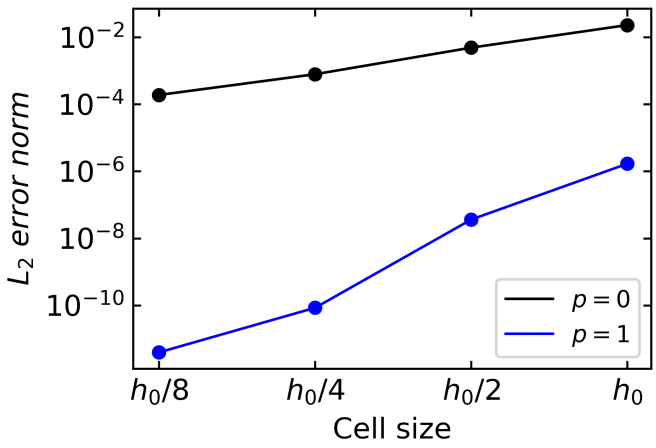

Figure 3.8: Convergence rates for the Prandtl-Mayer problem.

1 to compute the convergence plot found in figure 3.8. It is worth mentioning that the number of degrees of freedom, which is a direct measure of the computational cost, is 894976 in the most refined case with order zero polynomials, while the least refined order one case is 41952, which is a twenty-fold decrease in the number of degrees of freedom with a 100-fold reduction of the quadratic error.

3.4.3 Planar Plasma Column:

As mentioned in chapter 2 the main driver of the expansion of the plasma is the magnetic force on the electrons. This magnetic force guides electrons along the magnetic streamlines and the expansion of electrons creates an ambipolar electric field confining and accelerating the ions. In the limit of non-magnetised ions the balance between this confining electric field and the electron pressure is exact in the throat of the nozzle. To test the behaviour of electron magnetization along the expansion we consider the following test case:

- Constant axial magnetic field: $\mathbf{B} = B\mathbf{u_z}$
- Gaussian profile for the density at the inlet.
- Sonic ions at the throat.
- Polytropic electrons $\gamma = 1.2$.
- Symmetry plane (wall) in $x = 0$.

We can obtain an analytical solution as the equilibrium between magnetic and pressure forces is maintained in the whole domain and therefore the Gaussian profile at the inlet is transported downstream without deformation. This also implies that

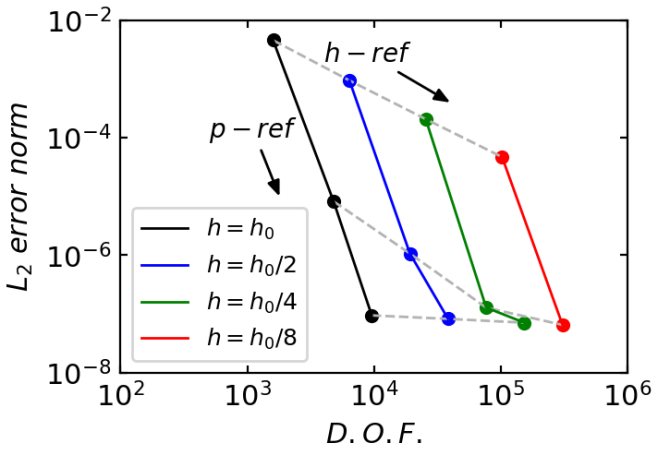

Figure 3.9: Convergence of the plasma column problem with h and p refinement.

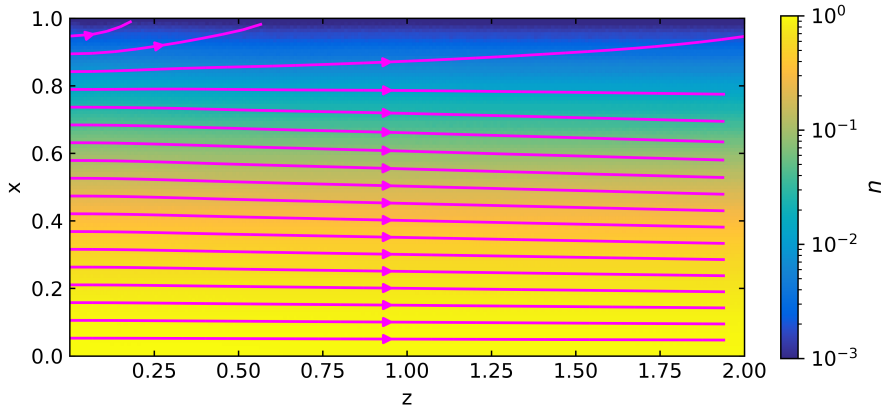

Figure 3.10: Density and streamlines for the planar plasma column with polynomials of order 1 and refinement 3.

the radial momentum must be zero everywhere in the domain. Figure 3.9 the convergence behaviour of the test with h (cell size) refinement and p (polynomial order) refinement. For this test several simulations where run with polynomial orders ranging from 0 to 2 and four different mesh refinements. Clearly, polynomial refinement is far more beneficial than mesh refinement in terms of accuracy per degree of freedom, this situation is common for high order methods and particularly DGFEM [77]. In the case of our problem the situation is even more critical particularly with order 0 polynomials as this means no degrees of freedom are located in the symmetry axis and , therefore, force balance is not attainable in that region for piecewise-constant solutions. It is clear however that the error stagnates at around $10^{-7} - 10^{-8}$, this is due to the imposition of the upper boundary as an outflow boundary. This implies the boundary conditions require a normal flux of mass in the $x = 1$ boundary, this forces a radial flux outwards in a thin layer at $x = 1$ making the solution we are comparing to inexact in that region, this can be appreciated in figure 3.10 where in the region $x > 0.8$ the streamlines are seen to bend upwards.

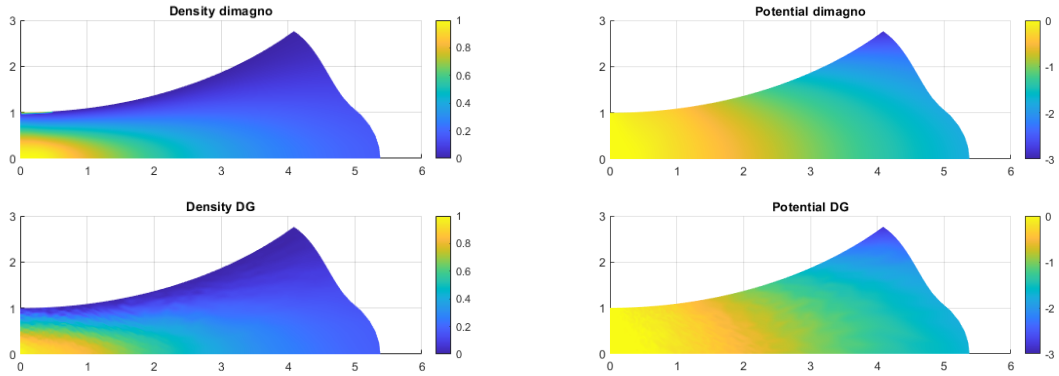

Figure 3.11: Plasma density and electric potential calculated with the Dimagno code and the Discontinuous Galerkin method.

3.4.4 Dimagno Verification Tests

As discussed before, Dimagno is a fluid simulation code that appeared in the 2010s [20]. The models included in`POSETS` supersede and go beyond the one solved by Dimagno. It is, therefore, natural to compare the code used in this work against the output of Dimagno. To this end a simulation following the next indications. Plasma expansion in a divergent-planar magnetic nozzle generated by two infinite wires located at $(z, r) = (0, \pm 2.5)$ with a gaussian density profile with sonic velocity entering the domain in the $r \in [0, 1]$. In the next figure the plasma density and electric potential of the Discontinuous Galerkin and the Dimagno solution are compared.

We observe that the error in the density profiles is negligible everywhere in the domain except for the lateral part close to the source. This difference can be explained by the fact that Dimagno uses the method of characteristics in order to solve the equations and therefore only solves the region connected to the source. Moreover, Dimagno forces the last ion magnetic streamline to be tangential to its corresponding magnetic streamline. The combination of these two differences in the solution mechanism explains the matching of the solutions in the bulk and the appearance of a clear discrepancy in the lateral part of the plasma.

3.4.5 Magnetic Field Solver

The magnetic field solver transforms Ampere's law in a second order equation (2.51) using the magnetic vector potential 2.6. For the test in this subsection we use a simple problem consisting of two wires of radius 1 carrying current in the y axis direction. Both wires carry a current density of 1 and therefore a total current of π. The first wire is centered at $(z, x) = (4, 4)$ and carries current in the positive direction of the y axis and the second current is centered in the $(z, x) = (-4, -4)$

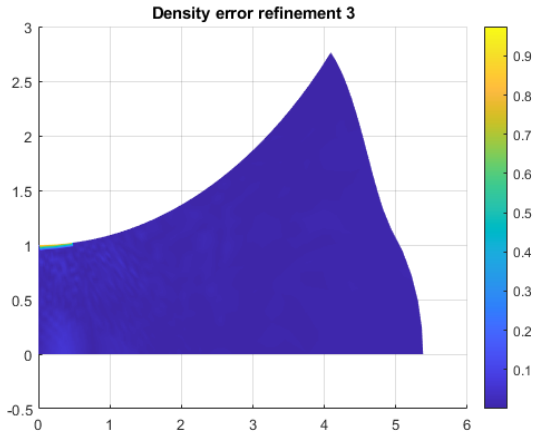

Figure 3.12: Difference between the density solution obtained with DIMAGNO and with the POSETS code.

and carries current in the negative y direction. All currents can be cast as $\boldsymbol{J} = J_y \mathbf{1}_y$ and therefore, equation 2.51 transforms into a scalar equation in two dimensions for the out-of-plane component of the magnetic vector potential $\nabla^2 A_y = -\mu J_y$. The analytic magnetic field generated by this setup can be easily calculated using Biot-Savart's law. To gauge the accuracy of our magnetic field solver we check two different properties, first the transition to infinity using the PML and the accuracy of the finite element solution.

To test the former we solve the problem described before in a 30×30 domain, a 20×20 domain and in a 12×12 domain. In the smaller domain the region $|x| \in [10, 12] \cup |z| \in [10, 12]$ is occupied by a 4 layer PML as specified in [57], while the other two have vacuum everywhere in the domain. We obtain the magnetic potentials in all three cases $A_{\xi,30}$ $A_{\xi,20}$ and $A_{\xi,PML}$ respectively. All cases are solved with the same cell size and polynomial order in the elements.

In figure 3.13 we show the isolines of the out-of-plane component of the magnetic vector potential in all three cases mentioned above. If we take the solution with the 30×30 domain as a reference we observe clearly that the solution with the absorbing layers performs equally or better than the 20×20 solution everywhere in the domain while allowing for almost a four-fold reduction on the size of the problem. This is particularly important in the case where this problem is coupled to the plasma transport as an increase in the size of the domain for the magnetic field solver would require solving the fluid equations in the same domain.

Moreover, we compare the magnetic field of the solution with the PML againt the exact solution for the magnetic field along the $x = 0$ axis in figure 3.14. We observe that the normalized L_2 error reaches a maximum of $\mathcal{O}(10^{-2})$ close to the boundaries while being $\mathcal{O}(10^{-4})$ in most of the domain.

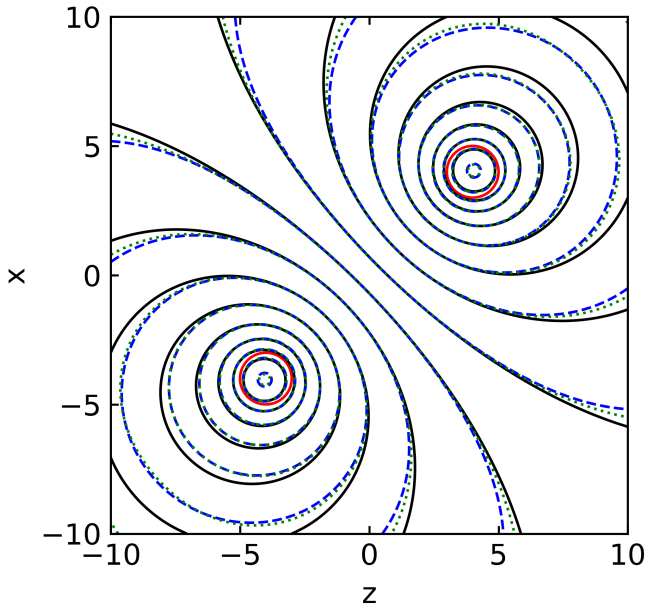

Figure 3.13: Vector potential isolines calculated in the 30×30 domain (solid-black lines), 20×20 domain (dashed-blue lines) and the 12×12 domain (dotted-green lines).

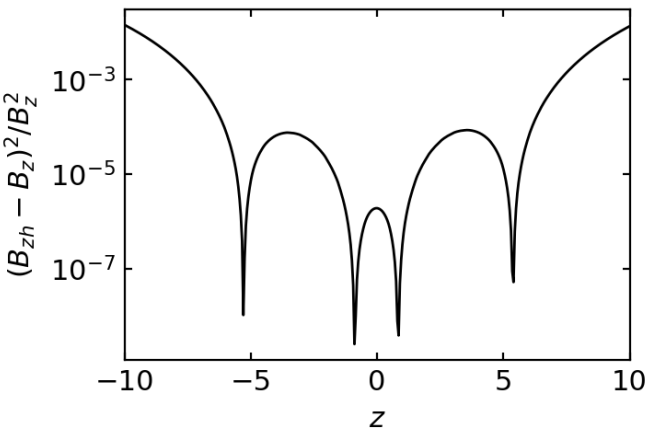

Figure 3.14: Normalized quadratic error for the magnetic field along the $x = 0$ line for the test problem with a PML as described in the text.

Polynomial degree	Cell size	L_2 error	Convergence rate
0	0.2	0.0041	1.6
	0.15	0.0025	
	0.1	0.0014	
1	0.2	0.0025	2.2
	0.15	0.0013	
	0.1	0.00053	

Table 3.1: Summary of convergence results for cell size and polynomial degree in the test for ion and neutral energy equations.

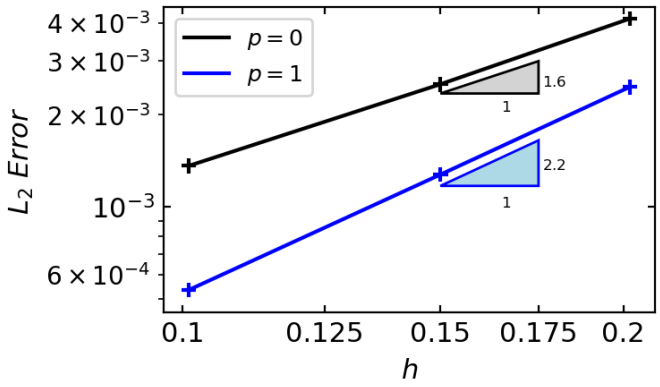

Figure 3.15: Convergence plot for the numerical test considering ion and neutral energy.

3.4.6 Convergence of the discretization of the energy equation

Discontinuous Galerkin methods are, by construction, locally conservative for systems of hyperbolic equations [39]. However, as explained previously, we have introduced some minor, yet non-conservative terms in the discretization of the energy equation for both ions and neutrals 3.2.2. In this regard, our integration method departs from the typical DG methods and therefore we find necessary to check the effect of h (cell size) and p (polynomial order) refinement in our solution. To this end we run a reference simulation considering ion and neutral energy with three different cell sizes and for polynomial orders 0 and 1. We then run a fifth simulation with an even finer cell size and order 1 elements, and take that solution as exact. In table 3.1 we show the global L_2 error of the different simulations, the corresponding convergence plot is found in figure 3.15. We observe a convergence rate of 1.6 for the order zero discretization and 2.2 for the order one discretization; the expected asymptotic convergence rate for DG methods is $\mathcal{O}(h^{p+1})$.

Chapter 4

Plasma Expansion in a Magnetic Arch

The presents chapter studies the feasibility of the extraction of plasma from a closed lined magnetic topology, so-called, magnetic arch. First, a description of the model used is presented. Second, the physical setup for the simulations is explained and the simulation results are presented. In this section we first show that plasma can be extracted from a magnetic arch configuration in the $\beta = 0$ limit albeit with a loss of ion momentum when traversing the closed line topology. After that we show that, in this configuration, plasma induced magnetic field is beneficial for thrust generation as it opens the magnetic streamlines allowing for a higher electron current to be extracted. The content of this chapter is a verbatim reproduction of the peer-reviewed article [28] appearing in Plasma Sources Science and Technology and is one of the contributions of this thesis to the ZARATHUSTRA project. Kindly excuse any redundant information which might be present in the former chapters of this work, particularly in the introduction and the model sections. These offer however, deeper detail into the technicalities of the topic in question in the present chapter.

4.1 Introduction

Magnetically-guided plasma expansions are a central part of the operation of electrodeless plasma thrusters (EPTs) [2, 1, 17, 78]. A magnetic nozzle (MN) is commonly used to externally expand and accelerate the plasma generated by the source [20, 79, 80, 81]. This is the case of e.g. the helicon plasma thruster (HPT) [82, 83, 84, 85] and the electron-cyclotron plasma thruster (ECRT) [86, 87, 88]. Additionally, non-axisymmetric MNs have been proposed for contactless thrust vector control [21, 89].

When the plasma consists of warm electrons and relatively cold ions, as in the devices listed above, the MN is termed 'electron-driven.' These MNs work by perpendicularly confining the expansion of the warm plasma electrons, which must be well magnetized. This confinement occurs thanks to the applied magnetic field $\boldsymbol{B}_a$ and the diamagnetic azimuthal electron current density $j_{\theta e}$ that forms as a consequence of the existence of a perpendicular electron pressure gradient and the $\boldsymbol{E} \times \boldsymbol{B}$ drift. This current density gives rise to a magnetic force density in the plasma. Part of this force density is directed radially inward ($j_{\theta e} B_{az}$), while the other part is axially outward ($-j_{\theta e} B_{ar}$). The former balances the electron pressure (and the electric force) in the radial direction; the latter gives rise by reaction to the magnetic thrust, which is the force felt by the thruster magnetic circuit due to the magnetic field induced by the electric current density in the plasma. In turn, the parallel electron pressure is balanced by the self-consistent ambipolar electrostatic field that forms in the MN. This field confines electrons and accelerates ions, converting the electron thermal energy into directed kinetic ion energy [20].

Downstream, the plasma jet must eventually separate from the turning magnetic lines to prevent the increase of plume divergence and the cancellation of thrust [79]. It should be noted that, at least for hot-electron and cold-ion plasmas, ions do not need to be magnetized for the MN to operate as intended; indeed, a high ion magnetization is generally undersirable, as it makes plasma detachment occur farther downstream, increasing plume divergence angle, and promoting the appearance of a paramagnetic azimuthal ion current density $j_{\theta i}$ in the plasma that results in magnetic drag [20]. However, special devices, such as the variable specific impulse magnetoplasma rocket (VASIMR) [90], rely on the expansion of hot ions, where ion magnetization is a necessity.

A single cylindrical EPT creates a magnetic dipole moment that may induce secular torques on the spacecraft in the presence of the geomagnetic field. Flying EPTs in pairs with opposite magnetic polarities, such that the net dipole moment cancels out, is a straightforward and natural way to avoid this issue. Also, the use of more than one thruster (known as 'clustering') is a simple way of scaling thrust levels for larger space missions. A pair of EPTs has the additional benefit that, if each unit can be throttled independently, some degree of thrust vector control can be achieved without moving parts. In this configuration, the two MNs interact and their lines connect, resulting in a new magnetic topology that here we term 'magnetic arch' (MA), sketched in figure 4.1a.

Similarly, the MA is an intrinsic part of some novel EPT geometries, such as the magnetic arch thruster (MAT) concept, where the cylindrical discharge chamber of traditional EPTs is replaced by a "C"-shaped chamber, enveloped by coils that create a magnetic field essentially parallel to the walls, as represented in figure 4.1b [91, 56]. By removing the rear wall that exists in cylindrical EPTs and ensuring full magnetic shielding of the remaining walls, it is hypothesized that this geometry

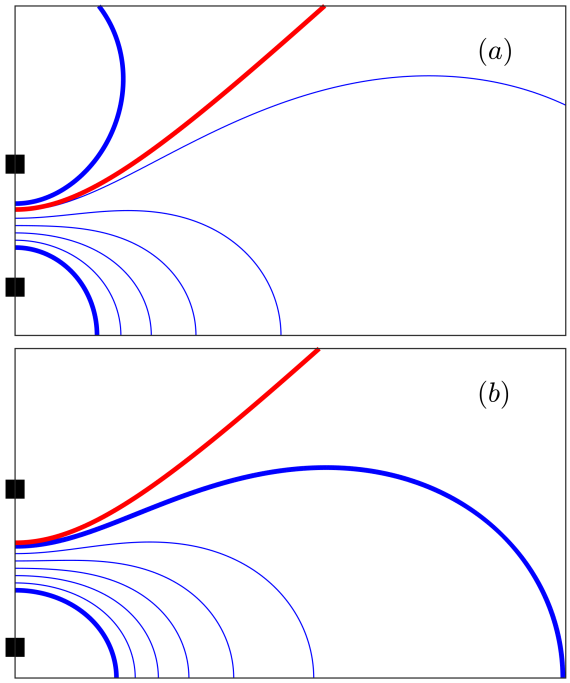

Figure 4.1: Sketch of the magnetic lines of two cylindrical EPTs firing in parallel with opposite magnetic polarities, forming an external MA (a). Sketch of the magnetic lines of the conceptual MAT (b), which also features an MA in the plasma expansion region. In red, the location of the ionization chambers; in black, the position of magnetic coils; and in blue, selected magnetic lines.

could bring advantages with regards to losses, while reducing the appearance of external magnetic torques on the spacecraft.

The plasma expansion in an MA is radically different to that in an axisymmetric MN: while in a single MN the plasma flux is roughly parallel to the applied field $\boldsymbol{B}_a$ (at least before detachment is well under way), in an MA the flux is only parallel initially; downstream, where the lines of the two MNs connect, the plasma flux must necessarily traverse the applied field roughly perpendicularly. Also, while the plasma currents in the axisymmetric MN are predominantly diamagnetic (i.e., thrust producing), they are expected to be diamagnetic and paramagnetic in the upstream and downstream regions of the MA plasma expansion, respectively. Relatedly, while in a MN the plasma-induced magnetic field $\boldsymbol{B}_p$ plays a secondary role in deforming the shape of the lines, increasing divergence minimally if the MN is well-designed [55], it can play a more important role in the MA, potentially changing the line topology of the total field, $\boldsymbol{B} = \boldsymbol{B}_a + \boldsymbol{B}_p$, with respect to that of the applied one alone, $\boldsymbol{B}_a$. Finally, the interaction of the two plasma jets coming from each end of the device may lead to collisionless shock-like structures in the plume, not found in smooth MN plasma expansions [20].

The objective of this work is to present a first model of the MA plasma expansion to examine the viability of this magnetic topology for plasma acceleration and discuss its main physical mechanisms, in particular behind ion acceleration and magnetic thrust production. By examining the the zero plasma-beta expansion, $\beta = \mu_0 n T_e / B_a^2 = 0$, and expansions with small $\beta \neq 0$, the effects of the plasma-induced magnetic field on the shape of the MA and the generated thrust are discussed. The model is of application to clusters of two cylindrical EPTs and to the novel MAT configuration described above. Finally, we identify the main physics currently outside of the present model that should be included in the future. Nevertheless, the major limitations of the study can be already stated from the outset: firstly, we shall only study a 2D planar version of the MA, rather than a full 3D geometry. Secondly, we shall ignore plasma kinetics, and employ a collisionless multi-fluid plasma model with a simple polytropic closure for the electron pressure.

The rest of the document is structured as follows. Section 4.2 presents the mathematical model of the plasma expansion in the MA and describes the approach followed to integrate it numerically. Section 4.3 contains the results of the first MA simulation using this model in the $\beta = 0$ limit, including plasma density, ion velocity, electrostatic potential, plasma currents, and magnetic thrust. Subsection 4.3.2 then discusses the plasma-induced magnetic field for $\beta \neq 0$, and how its presence alters the expansion and magnetic thrust with respect to the $\beta = 0$ case. The limitations of the model and its results are reviewed in section 4.4. Finally, section 4.5 briefly summarizes the main points of this work. A preliminary version of this work was recently presented in [91].

4.2 Model

A two-dimensional, two-fluid (ions i and electrons e) model of the steady-state plasma flow in an MA is considered. The model takes the following assumptions:

1. Quasineutral, collisionless, fully-ionized plasma.
2. Inertialess, quasi-Maxwellian, perfectly-magnetized electrons with a polytropic closure relation.
3. Cold, singly-charged ions, with arbitrary magnetization, emitted from each source exit. Moreover, ions are assumed to remain cold downstream, neglecting the effects of any shock-like discontinuities on ion temperature/distribution that may exist in the solution.
4. Planar-symmetric geometry, as an intermediate step toward the actual three-dimensional geometry of the device. We consider the meridian plane of the plume and assume an infinite plasma with uniform properties in the perpendicular direction.

To normalize the model, we select the ion mass m_i, the electron charge q_e, and the radius R of one of the plasma thruster exits. And, using the properties at the center of one of the two symmetric thruster outlets (where variables are marked with subindex 0), the electron temperature T_{e0} (in energy units) and the plasma density n_0 used for injection. Note that, even if flux coming from one outlet ever arrives at the other, T_{e0} and n_0 are defined from the single-beamlet injection properties. This point of the outlets is also chosen as the origin of the electrostatic potential, where $\phi_0 = 0$. In the following, all symbols are already appropriately dimensionless. In particular, the dimensionless magnetic field strength at the center of the outlet, B_0, is normalized with $\sqrt{m_i T_{e0}}/(eR)$, and coincides numerically with the dimensionless ion gyrofrequency Ω_{i0}, and defines the (initial) ion magnetization degree.

Figure 4.2 sketches the problem domain. We define a right-handed reference frame with the plane Oxy coincident with the exit plane of the plasma sources, and the Oz axis pointing downstream. The plane under study is the Oxz plane, and in the 2D expansion the plasma is infinite and uniform in the y direction. The plane Oyz is a symmetry plane, and thus only the upper half of the plane ($x \geq 0$, shown in the figure) will be simulated. Without loss of generality, $\boldsymbol{B}$ is taken to point axially downstream in this part of the MA. We introduce the Cartesian vector basis $\{\mathbf{1}_x, \mathbf{1}_y, \mathbf{1}_z\}$ and the magnetic vector basis $\{\mathbf{1}_b, \mathbf{1}_\perp, \mathbf{1}_y\}$, with $\mathbf{1}_b = \boldsymbol{B}/B$ and $\mathbf{1}_\perp = \mathbf{1}_y \times \mathbf{1}_b$. Both bases are right-handed and orthonormal.

The applied magnetic field $\boldsymbol{B}_a$ is generated by a set of thin, infinite electric wires w, each carrying an electric current I_w along the $\mathbf{1}_y$ direction. The arrangement of wires and their electric currents is antisymmetric about the Oyz symmetry plane, and the sum of the I_w over all the wires equals zero. The magnetic streamfunction of a *single wire* w is given by

$$\psi_{Bw} = -\frac{\mu_0 I_w}{2\pi} \ln \rho_w, \tag{4.1}$$

where ρ_w is the polar distance from the wire. Summing over the wire contributions we obtain the streamfunction ψ_{Ba} of the applied field.

The plasma-induced magnetic field $\boldsymbol{B}_p$ has the streamfunction ψ_{Bp} given by Ampère's equation, which reduces to a manifestly elliptic partial differential equation:

$$\frac{\partial^2 \psi_{Bp}}{\partial z^2} + \frac{\partial^2 \psi_{Bp}}{\partial x^2} = -\mu_0 j_y \equiv -\beta_0 B_{a0}^2 j_y, \tag{4.2}$$

where j_y is the out-of-plane plasma electric current and $\beta_0 = \mu_0/B_{a0}^2$ is the β parameter at the centerpoint of the thruster outlet, already normalized with n_0 and T_{e0}.

The total magnetic field $\boldsymbol{B}$ is the sum of the applied and plasma-induced ones, with $\psi_B = \psi_{Ba} + \psi_{Bp}$, and

$$\boldsymbol{B} \equiv \boldsymbol{B}_a + \boldsymbol{B}_p = \nabla \psi_B \times \mathbf{1}_y. \tag{4.3}$$

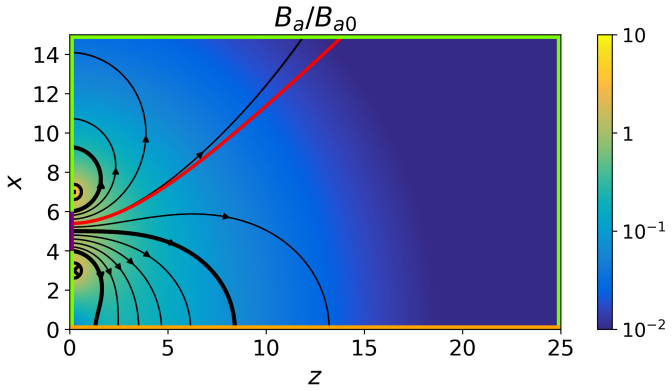

Figure 4.2: Sketch of the problem domain of the 2D planar MA plasma expansion. Only one half of the MA is simulated, taking advantage of the symmetry plane Oyz (in orange). The plasma source is located on the left of the domain (purple line), where plasma inflow conditions are prescribed. The second plasma source is located below the symmetry plane and is not visible in the sketch. The rest of the boundaries are free (supersonic) outflow boundaries (green lines). The applied magnetic field $\boldsymbol{B}_a$ strength (colormap) and streamlines (black lines) are shown. Magnetic lines connecting with the source edges and center are shown as thicker lines. The symbols $\otimes$ and $\odot$ are used to denote the location of electric wires generating the field, with electric current going into and out of the paper, respectively. The magnetic sepatratrix line of the applied field, given by $\psi_{Ba} = 0$, is plotted in red.

When $\beta_0 = 0$ the plasma-induced magnetic field $\boldsymbol{B}_p$ is negligible with respect to the applied one $\boldsymbol{B}_a$, and the total field coincides with the latter. Then, equation (4.2) may be dropped from the model. This is the case analyzed in the first part of section 4.3.

Note that $\mathbf{1}_\perp \equiv \nabla\psi_B/B$ and, for any single-variable function $f(\psi_B)$,

$$\nabla f = \frac{\partial f}{\partial \mathbf{1}_\perp}\mathbf{1}_\perp = B\frac{\mathrm{d}f}{\mathrm{d}\psi_B}\mathbf{1}_\perp.$$

The relevant collisionless fluid equations of electrons and ions are

$$\frac{\partial n}{\partial t} + \nabla\cdot(n\boldsymbol{u}_e) = 0, \tag{4.4}$$

$$0 = -\nabla(nT_e) + n\nabla\phi - n\boldsymbol{u}_e \times \boldsymbol{B} \tag{4.5}$$

$$\frac{\partial n}{\partial t} + \nabla\cdot(n\boldsymbol{u}_i) = 0, \tag{4.6}$$

$$\frac{\partial n\boldsymbol{u}_i}{\partial t} + \nabla\cdot(n\boldsymbol{u}_i\boldsymbol{u}_i) = -n\nabla\phi + n\boldsymbol{u}_i \times \boldsymbol{B} \tag{4.7}$$

where we have already imposed plasma quasineutrality,

$$n \equiv n_e = n_i. \tag{4.8}$$

The electrons are assumed polytropic with the law $T_e = n^{\gamma-1}$ on the whole domain, with fixed exponent γ. We note that

$$\frac{1}{n}\nabla(nT_e) = \frac{\gamma}{\gamma-1}\nabla n^{\gamma-1},$$

where the equality holds for $\gamma \neq 1$. Observe that the relevant dimensionless sound speed is $c_s = \sqrt{\gamma T_e}$.

Under the assumption of full electron magnetization, electron streamlines coincide with magnetic lines. Indeed, from equation (4.5) we infer that, since there are no pressure gradients nor electric fields in the uniform $\mathbf{1}_y$ direction, there is no electron fluid velocity along $\mathbf{1}_\perp$. Therefore we write the electron fluid velocity as:

$$\boldsymbol{u}_e = u_{ye}\mathbf{1}_y + u_{\parallel e}\mathbf{1}_b. \tag{4.9}$$

With these premises, equation (4.5) becomes

$$0 = -\nabla\left[\frac{\gamma}{\gamma-1}(n^{\gamma-1}-1) - \phi\right] - u_{ye}B\mathbf{1}_\perp. \tag{4.10}$$

Integrating this equation along the magnetic lines, we find that the electron energy H_e is conserved along them,

$$H_e(\psi_B) = \frac{\gamma}{\gamma-1}(n^{\gamma-1}-1) - \phi. \tag{4.11}$$

The function $-H_e$ can also be understood as a thermalized potential for the electron dynamics.

The out-of-plane electron velocity u_{ye} can be computed from the map of ∇H_e [20]:

$$u_{ye}(\psi_B) = -\frac{1}{B}\frac{\partial H_e}{\partial \mathbf{1}_\perp} = -\frac{\mathrm{d}H_e}{\mathrm{d}\psi_B} = -H_e'. \tag{4.12}$$

This u_{ye} results from the sum of the diamagnetic (i.e., pressure-driven) and $\boldsymbol{E}\times\boldsymbol{B}$ drifts, which are the only first-order drifts in the problem (and indeed, they scale as $1/B$). The function H_e, its derivative H_e', and consequently u_{ye}, can be computed from the boundary conditions at $z = 0$ on each magnetic line. This computation can be done a priori, i.e. before solving the rest of the plasma problem. Observe that only one value of H_e may be imposed per magnetic line, and this restricts the set of valid boundary conditions elsewhere.

Lastly, we note that $u_{\parallel e}$ does not appear in equations (4.5)–(4.7), and is effectively decoupled from the rest of the problem. Indeed, it can be computed from equation (4.4) and the boundary conditions a posteriori, after all other variables have been solved for. In the steady state, and for zero perpendicular electron velocity ($u_{\perp e} = 0$), this equation reduces to

$$\frac{\partial}{\partial \mathbf{1}_b}\left(\frac{nu_{\parallel e}}{B}\right) = 0. \tag{4.13}$$

There are two different types of magnetic lines in the MA: *inner lines* that connect the two plasma sources through the symmetry plane, and *outer lines* that go around the upper part of the domain without intersecting it. In the $\beta_0 = 0$ case, the separatrix between these two behaviors corresponds with the magnetic line labeled by $\psi_B = 0$ (see figure 4.2), inner lines have $\psi_B < 0$, and outer lines have $\psi_B > 0$.

In steady state, the electron current on inner lines must be zero due to the symmetry of the problem, and therefore $u_{\parallel e} = 0$ there. This sets an additional consistency requirement on the electron velocity boundary conditions on these lines. On the other hand, outer lines can carry electron current, and $u_{\parallel e} \neq 0$ is allowed on them. For a globally-current free MA, the total electron current leaving the plasma sources along these magnetic lines must equal the total ion current emitted by the sources. This aspect of the model is discussed in more detail in section 4.4.

The electron equations have therefore been reduced to (1) a conservation law for H_e, (2) an algebraic expression for u_{ye}, (3) a line-wise differential equation for $u_{\parallel e}$. Equation (4.11) may be regarded as the law that provides the electrostatic potential on each magnetic line as a function of the electron density and the magnetic streamline function:

$$\phi(n, \psi_B) = \frac{\gamma}{\gamma - 1}[n^{\gamma-1} - 1] - H_e(\psi_B). \tag{4.14}$$

Introducing relation (4.14) into the ion momentum equation (4.7) to eliminate ϕ and using (4.12) to eliminate u_{ye} results in the following set of differential equations for n, u_{zi}, u_{xi}, and u_{yi}:

$$\frac{\partial n}{\partial t} + \frac{\partial n u_{zi}}{\partial z} + \frac{\partial n u_{xi}}{\partial x} = 0 \tag{4.15}$$

$$\frac{\partial n u_{zi}}{\partial t} + \frac{\partial n u_{zi} u_{zi}}{\partial z} + \frac{\partial n u_{xi} u_{zi}}{\partial x} + \frac{\partial n^\gamma}{\partial z} = -n\left(H_e' + u_{yi}\right) B_x, \tag{4.16}$$

$$\frac{\partial n u_{xi}}{\partial t} + \frac{\partial n u_{xi} u_{zi}}{\partial z} + \frac{\partial n u_{xi} u_{xi}}{\partial x} + \frac{\partial n^\gamma}{\partial x} = n\left(H_e' + u_{yi}\right) B_z, \tag{4.17}$$

$$\frac{\partial n u_{yi}}{\partial t} + \frac{\partial n u_{yi} u_{zi}}{\partial z} + \frac{\partial n u_{xi} u_{yi}}{\partial x} = n(u_{zi} B_x - u_{xi} B_z). \tag{4.18}$$

In the steady state, each species admits a streamfunction ψ_j such that $\nabla\psi_j = -n u_{xj}\mathbf{1}_z + n u_{zj}\mathbf{1}_x$, for $j = e, i$. For the magnetized electrons, ψ_e is a function of ψ_B. For ions, which are non-magnetized or only partially-magnetized, streamlines may differ from magnetic lines.

The last ion equation (4.18) can be integrated to yield (see [20] for the analogous equation in the axisymmetric MN):

$$u_{yi} + \psi_B = D(\psi_i), \tag{4.19}$$

where $D(\psi_i)$ depends only on the ion streamfunction and can be determined from the boundary conditions at the thruster outlet.

Observe that, if $u_{yi} = 0$ at injection, the ion out-of-plane velocity u_{yi} develops only when ion streamlines separate from their initial magnetic field lines; this u_{yi} is positive if the ion streamline detaches inwardly from the magnetic field lines (i.e. along $-\mathbf{1}_\perp$), and negative if separation is outwardly (i.e., along $+\mathbf{1}_\perp$). Nevertheless, when ion magnetization is weak ($B_0 \leq O(1)$), the last term in the ion momentum equations (the ion magnetic force) is typically small. Then, if $u_{yi} \ll 1$ initially, it remains so everywhere else, and the electron magnetic force dominates in the right hand side of equations (4.16) and (4.17).

Finally, we define the in-plane ion velocity as $\tilde{\boldsymbol{u}}_i = u_{zi}\mathbf{1}_z + u_{xi}\mathbf{1}_x$, and the in-plane ion Mach number as $M_i = \tilde{u}_i/\sqrt{\gamma T_e}$.

4.2.1 Numerical integration

The differential ion equations (4.15)–(4.18) are in conservative form, and can be formally written as

$$\frac{\partial \boldsymbol{Q}}{\partial t} + \nabla \cdot \mathcal{F} = \boldsymbol{R}, \tag{4.20}$$

where

$$\boldsymbol{Q} = \begin{bmatrix} n \\ nu_{zi} \\ nu_{xi} \\ nu_{yi} \end{bmatrix},$$

$$\mathcal{F} = \begin{bmatrix} nu_{zi} & nu_{xi} \\ nu_{zi}^2 + n^\gamma & nu_{zi}u_{xi} \\ nu_{zi}u_{xi} & nu_{xi}^2 + n^\gamma \\ nu_{zi}u_{yi} & nu_{xi}u_{yi} \end{bmatrix},$$

$$\boldsymbol{R} = \begin{bmatrix} 0 \\ -n\left(H_e' + u_{yi}\right) B_x \\ n\left(H_e' + u_{yi}\right) B_z \\ n(u_{zi}B_x - u_{xi}B_z) \end{bmatrix}.$$

The equations are discretized using a discontinuous Galerkin (DG) method, which for zeroth-order polynomials coincides with the finite volume method. The main advantage of the DG approach is that it enables easily improving the accuracy of solution by refining the mesh size h and/or increasing the order of the polynomials p. After multiplying equation (4.20) by a test vector $\boldsymbol{V}$, integrating in an element D_k with boundary ∂D_k, and using integration by parts, the following weak form is obtained:

$$\int_{D_k} \boldsymbol{V} \cdot \frac{\partial \boldsymbol{Q}}{\partial t} \mathrm{d}\Omega + \int_{\partial D_k} \boldsymbol{V} \cdot \mathcal{F} \cdot \mathbf{1}_n \mathrm{d}S - \int_{D_k} \mathcal{F} : \nabla \boldsymbol{V} \mathrm{d}\Omega = \int_{D_k} \boldsymbol{V} \cdot \boldsymbol{R} \mathrm{d}\Omega,$$

where $\mathrm{d}\Omega$ is the area differential and $\mathbf{1}_n \mathrm{d}S$ is the outward-oriented area vector differential. Upon summation over all elements D_k of the domain, the second integral must be substituted by the corresponding numerical flux integral on all internal boundaries, taking into account the jump conditions across neighboring elements:

$$\int_{\Gamma_{int}} \boldsymbol{V} \cdot \mathcal{F} \cdot \mathbf{1}_n \mathrm{d}S = \int_{\Gamma_{int}} (\boldsymbol{V}^+ - \boldsymbol{V}^-) \cdot \tilde{\mathcal{F}} \cdot \mathbf{1}_n \mathrm{d}S \tag{4.21}$$

where Γ_{int} are the internal facets of the discretization, symbols '+' and '−' indicate the values of a discontinuous variable on one side and the other side of an internal facet, with $\mathbf{1}_n$ pointing toward the + side, and $\tilde{\mathcal{F}}$ is a numerical flux function. In this work a local Lax-Friedrichs flux is chosen, given by

$$\tilde{\mathcal{F}} = \frac{1}{2}(\mathcal{F}(\boldsymbol{Q}^+) - \mathcal{F}(\boldsymbol{Q}^-) + \alpha(\boldsymbol{Q}^+ - \boldsymbol{Q}^-)), \tag{4.22}$$

with α computed as the maximum of all eigenvalues of the normal flux Jacobian $(\nabla\mathcal{F} \cdot \mathbf{1}_n)$ evaluated in each side of the facet.

A similar treatment is applied on the external boundary facets, denoted by Γ_{ext}, except that on those facets the + side corresponds to the weakly imposed boundary conditions. The external boundary is further decomposed into Γ_{in}, Γ_{out}, and Γ_{sym} for supersonic inflow, supersonic outflow and symmetry plane boundaries respectively (see figure 4.2). At the inflow boundary, the $\boldsymbol{Q}^+$ vector on the + side is determined by the desired inflow conditions. At the supersonic outflow boundary, the $\boldsymbol{Q}^+$ vector is taken equal to $\boldsymbol{Q}^-$ (i.e., the value of $\boldsymbol{Q}$ on the corresponding boundary element of the domain, and finally, at the symmetry plane the $\boldsymbol{Q}^+$ vector equals $\boldsymbol{Q}^-$ in the density and parallel flux, and zero perpendicular flux is imposed (i.e., $nu_{xi} = 0$).

The discretized plasma problem is initially integrated in time using a third order Strong Stability Preserving Runge-Kutta scheme given in [39]. As initial conditions for the time integration, any gross approximation of the expected steady state flow can be used to speed up the convergence. After a sufficient amount of time steps, the steady state version of the equations are solved for.

In $\beta_0 \neq 0$ cases, the plasma-induced magnetic field problem is integrated using the continuous Galerkin method using first order (Lagrange) elements on the same mesh as the plasma problem. The weak form of (4.2) is

$$\int_\Omega \nabla V \cdot \nabla \psi_{Bp} \mathrm{d}\Omega = -\beta_0 B_{a0}^2 \int_\Omega V j_y \mathrm{d}\Omega \tag{4.23}$$

where V is a test function The boundary conditions used are $B_{pz} = \partial\psi_{Bp}/\partial x = 0$ at the symmetry plane $x = 0$ as indicated above, and $B_{px} = -\partial\psi_{Bp}/\partial z = 0$ at the thruster exit plane $z = 0$. On the rest of the boundary, and on the outside of the plasma domain shown in figure 4.2, a thin absorbing layer with artificial anisotropic magnetic permeability is defined following [57], a method that is equivalent to a coordinate stretching, to better approximate the transition to infinity of $\boldsymbol{B}_p$.

Notwithstanding this, it must be noted that the electric currents inside the thruster discharge chambers and beyond the simulation domain (i.e. further downstream) also affect the value of $\boldsymbol{B}_p$; as these currents are unknown, and to partially mitigate their influence on the results, the peripheral part of the domain is cut off from the shown results whenever $\beta_0 \neq 0$.

The self-consistent plasma and magnetic field solutions are determined using an iterative procedure: The plasma flow is first solved for the $\boldsymbol{B} = \boldsymbol{B}_a$ (i.e., ignoring the plasma-induced field). This yields a first approximation to the out-of-plane plasma electric current j_y, that is used to compute ψ_{Bp} for the next iteration using (4.2). The plasma flow is then recomputed for the new total field $\boldsymbol{B} = \boldsymbol{B}_a + \boldsymbol{B}_p$, and this process is repeated until plasma variables and ψ_{Bp} vary less than a prescribed tolerance from iteration to iteration, at which point convergence is reached.

The numerical implementation of the model employs GMSH [75] and FENICS [69] as open-source building blocks. The code has been verified successfully by simulating two simple cases: (1) a plasma flowing in a straight, uniform magnetic field; and (2) a 2D planar MN, and comparison against the existing DIMAGNO code [20]. Mass and momentum are successfully conserved in the simulation. A convergence study with mesh size and polynomial order was also conducted and confirmed the correct behavior of the code.

4.3 Simulation results

The applied magnetic field used for the simulations presented in this section is generated by four identical wires contained in the Oxy plane, located at $x = 3, 7, -3, -7$, as shown in figure 4.2. The thruster outlet in this half of the MA is located on the Oxy plane and goes from $x = 4$ to $x = 6$, and the normalized magnetic field at the center point of the thruster outlet, $(z, x) = (0, 5)$, is $B_0 = 1$ (mild initial ion magnetization).

The boundary conditions at the thruster outlet are modeled as follows:

$$
\begin{aligned}
&u_{zi}(0,x) = c_s(0,x); && n(0,x) = 10^{-3(x-5)^2};\\
&u_{xi}(0,x) = 0; && \phi(0,x) = 0;\\
&u_{yi}(0,x) = 0; && u_{\parallel e}(0,x) = \begin{cases} 0 & \text{for } \psi_B < 0 \\ U_{\parallel e} & \text{for } \psi_B \geq 0 \end{cases};
\end{aligned}
$$

i.e., the plasma density profile is assumed Gaussian, centered on $x = 5$ falling three orders of magnitude at the edges of the outlet, and the axial velocity is given as a function of the local sound velocity such that the in-plane ions are sonic at the magnetic throats ($M_{i0} = 1$) [20]. In the last expression, $U_{\parallel e}$ is a constant electron parallel velocity imposed on outer magnetic lines (i.e., those that can carry electron

current), computed such that the net electric current emitted by the plasma source is zero.

The electron polytropic exponent is set to $\gamma = 1.2$, a value commonly found empirically in MNs [92]. The out-of-plane electron velocity at the outlet of the thruster is given by equation (4.12) evaluated at $z = 0$ and the conditions above,

$$u_{ye}(0, x) = \frac{1}{B_z} \frac{\gamma}{\gamma - 1} \frac{\partial n^{\gamma - 1}}{\partial x}. \tag{4.24}$$

This choice of boundary conditions means that, at the outlet, there is no x-directed electric field, and the electron pressure and the electron magnetic force are in equilibrium.

For a smoother numerical solution and to prevent regions of zero plasma density, we extend these conditions all the way from $x = 3$ to $x = 7$, where the thin wires that generate the magnetic field are located. This completely determines the value of H_e on the whole the domain.

A mesh with cell diameter $h = 0.29$ and elements of order $p = 1$ were used to obtain the solutions shown below.

4.3.1 Plasma expansion in the $\beta_0 = 0$ limit

We begin with the analysis of the plasma expansion when $\beta_0 = 0$, and the total magnetic field $\boldsymbol{B} = \boldsymbol{B}_a$.

The map of $H_e(\psi_B)$ plays a crucial role in the plasma response as its derivative H_e' fixes the out-of-plane electron velocity u_{ye}, which defines the electron magnetic force. The resulting profile of H_e and the u_{ye} that follows from the boundary conditions are plotted in figure 4.3. The direction of the gradient of H_e causes the electron out-of-plane velocity u_{ye} to be positive and negative below and above the magnetic centerline of the plasma outlet, respectively, resulting in a magnetic force that confines the expanding electrons to their respective magnetic tubes. This change of sign contrasts with the typical situation in an electron-driven MN, where the out-of-plane electron velocity u_{ye} has the same sign everywhere [20].

Figure 4.4 displays the steady-state solutions for the plasma density n, electron temperature T_e, electrostatic potential ϕ, in-plane ion velocity $\tilde{\boldsymbol{u}}_i$, and in-plane ion Mach number M_i. Several aspects of these results stand out. Firstly, and similarly to a MN, the plasma expansion is initially guided by the magnetic field, and as the (essentially unmagnetized) ions accelerate, their streamlines do not adhere to the magnetic lines, separating inward with respect to $\boldsymbol{B}$, as in the axisymmetric MN case [79]. The plasma density, electron temperature, and electrostatic potential all decrease axially as the plasma expands in this first fraction of the domain. Secondly, ion streamlines on the periphery of the MA become essentially straight.

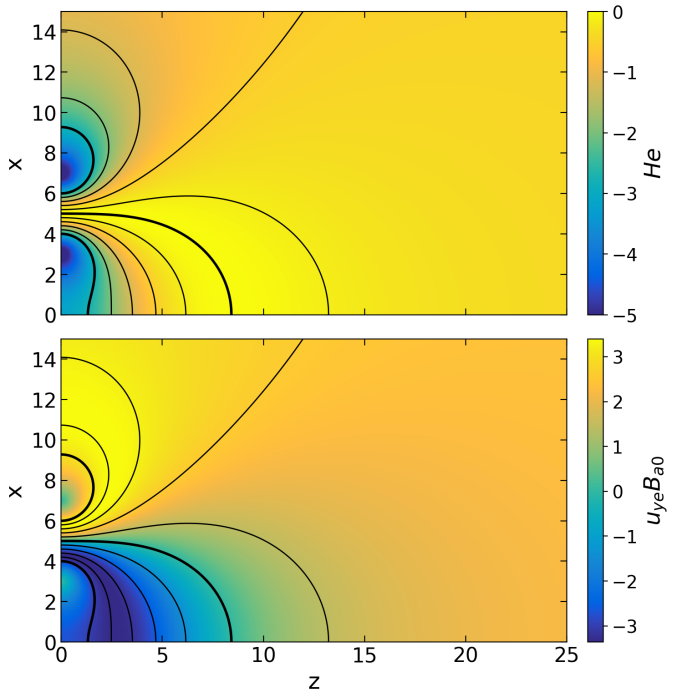

Figure 4.3: Dimensionless H_e function and electron out-of-plane velocity u_{ye} resulting from the applied magnetic field and the upstream plasma conditions (normalized with B_{a0}). Magnetic lines (black) are included in the plots for reference (thicker lines correspond to edges and center of the plasma source).

Inward detachment proceeds as in an MN for outer magnetic lines above the separatrix $\psi_B = 0$, which curve back and around the upper part of the domain. However, for inner magnetic lines below $\psi_B = 0$, which eventually curve downward and intersect the symmetry plane, ion trajectories must traverse magnetic lines in the outward direction. This changes ion detachment from being inward-directed to being outward-directed in part of the domain, in contrast to what occurs in an MN. Thirdly, closer to the symmetry plane, an oblique shock structure form, at the location where ion streamlines coming from the two thruster outlets would meet. Ion streamlines are deflected at the shock, and plasma density, electron temperature, and electrostatic potential rise across it. In-plane ion velocity and Mach number, which increase in the first part of the expansion, fall through the oblique shock. Ions remain supersonic downstream of it.

A major conclusion arising from these results is that the unmagnetized ions are not confined by the MA magnetic field, but are able to form a jet that propagates beyond it to infinity. This last observation is crucial to the validity of the MA concept and for the operation of a cluster of two cylindrical EPTs with opposing magnetic polarities.

Figure 4.5 displays the in-plane electric current density, $\tilde{\boldsymbol{j}} = n(\tilde{\boldsymbol{u}}_i - u_{\parallel e}\mathbf{1}_b)$, taking a uniform distribution of electron macroscopic velocity on the outer magnetic lines

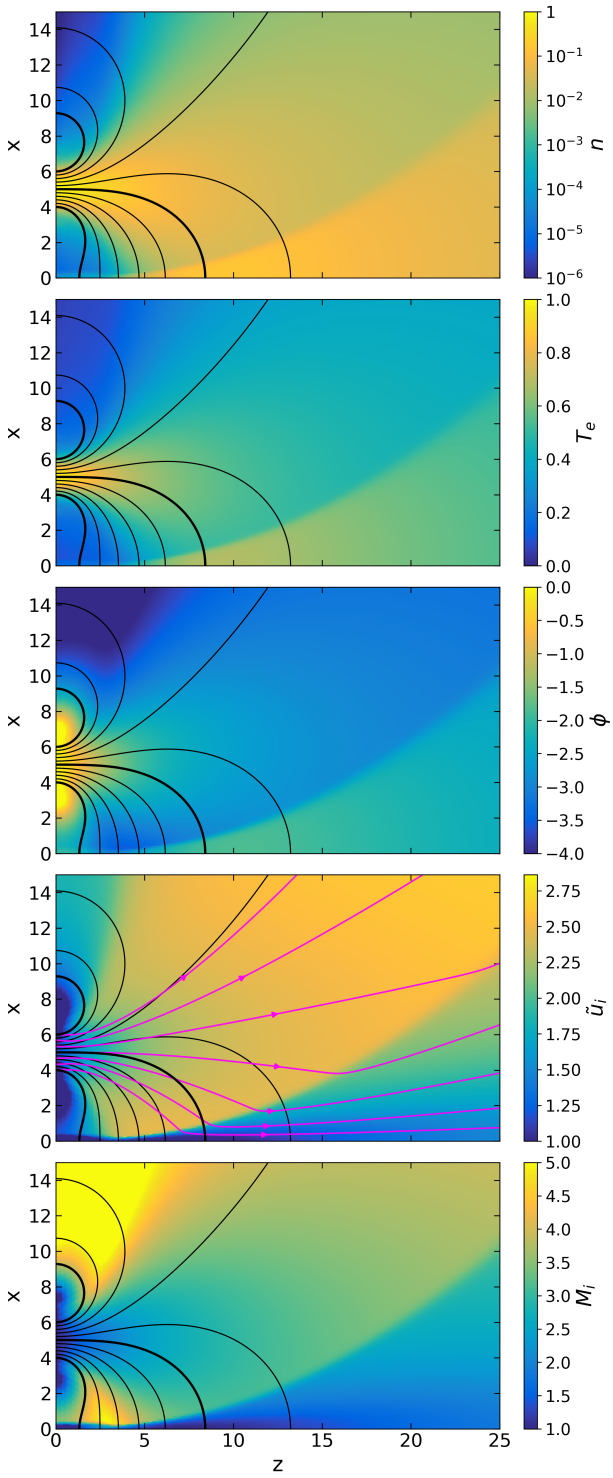

Figure 4.4: Dimensionless plasma density n, electron temperature T_e, electrostatic potential ϕ, in-plane ion velocity $\tilde{\boldsymbol{u}}_i$ and in-plane ion Mach number M_i. Selected ion streamlines (purple arrowed lines) are shown in the $\tilde{\boldsymbol{u}}_i$ plot. Magnetic lines (black) are included in the plots for reference (thicker lines correspond to edges and center of the plasma source).

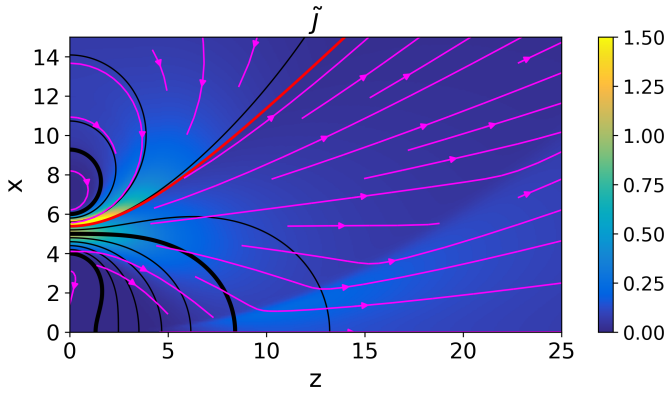

Figure 4.5: Dimensionless in-plane electric current density $\tilde{\boldsymbol{j}} = n(\tilde{\boldsymbol{u}}_i - u_{\|e}\mathbf{1}_b)$ (background color and purple arrowed lines). The separatrix line $\psi_B = 0$ is shown in red. Magnetic lines (black) are included in the plots for reference (thicker lines correspond to edges and center of the plasma source).

($\psi_B > 0$) to yield a globally current-free solution. As the electron flux on inner magnetic lines ($\psi_B < 0$) must be zero, the $\tilde{\boldsymbol{j}}$ in this region results solely from the ion current. Above the separatrix line $\psi_B = 0$, the strong compensating electron current responsible for making the system globally-current-free dominates. Clearly, the location of the separatrix line $\psi_B = 0$ with respect to the thruster outlet is a major defining aspect of the MA plasma expansion with regard to the in-plane electric currents. This aspect is further discussed in section 4.4.

Figure 4.6 depicts the x and z magnetic force densities $j_y B_z$ and $-j_y B_x$, where $j_y = n(u_{yi} - u_{ye})$ is the out-of-plane electric current density. We note that j_y is dominated by the electron contribution everywhere in the domain, as ion magnetization is low. Observe that the product $j_{ye}B$ is essentially independent of the magnitude B_0 by virtue of equation (4.12). Indeed, this product depends essentially on the initial electron pressure gradient at the thruster outlets, which determines the profile of H_e.

The two components of the magnetic force density are largest near the thruster exit plane. The x force density, essentially perpendicular to the magnetic lines in the first part of the domain, confines the plasma expansion laterally. As it can be observed from figure 4.6a, this confining force points in the $x > 0$ direction in the innermost part of the arch (i.e. in the region between the two plasma sources), while it points along $x < 0$ everywhere else, helping reduce the divergence of the jet.

The z force density gives rise to magnetic thrust, and is seen to be large and positive at the beginning of the expansion, where n, T_e and B are large. A small negative contribution exists downstream on inner magnetic lines, beginning at the point where $B_x = 0$ and lines curve down toward the symmetry plane. This negative contribution is mostly noticeable in the region after the shock wave, where plasma density (and therefore the out-of-plane current density) increases locally

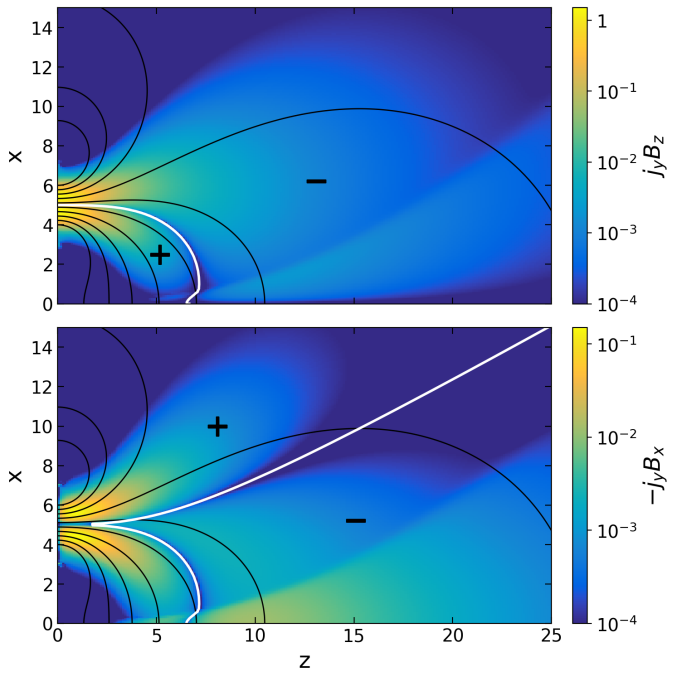

Figure 4.6: Magnetic force density in the axial ($-j_yB_x$) and radial (j_yB_z) directions. White lines separate regions with positive (+) and negative (−) values of the force densities. Magnetic lines (black) are included in the plots for reference (thicker lines correspond to edges and center of the plasma source). Mind the different color scales of each plot.

again. These characteristics are consequential on the magnetic force density and the generation of magnetic thrust: while positive thrust is generated initially in the region where they resemble a traditional MN, the magnetic force generates drag in the downstream region where the magnetic lines of each thruster connect, lowering the net thrust of the device.

As follows from the sum of the electron and ion momentum equations (4.5) and (4.7), the magnetic thrust force generated by the plasma contained in a rectangular control volume $\Omega(z)$ that spans the domain from the initial plane $z = 0$ to a variable axial position z can be equivalently computed as

$$\begin{aligned} F(z) - F(0) &= \int_{\Omega(z)} (-j_y B_x) \mathrm{d}\Omega \\ &= \int_{\partial\Omega(z)} [(nu_{zi}^2 + n^\gamma)\mathbf{1}_z + nu_{xi}u_{zi}\mathbf{1}_x] \cdot \mathbf{1}_n \mathrm{d}S, \end{aligned}$$

where $\partial\Omega(z)$ is the full boundary of the control volume. The first integral is the volume integral of the axial magnetic force density in figure 4.6b, while the second integral is the flux integral of total momentum on the boundaries of the integration domain. Observe that the relative importance of electron pressure thrust decreases to zero sufficiently far downstream, and that ion momentum dominates as the expansion converts electron thermal energy into ion kinetic energy.

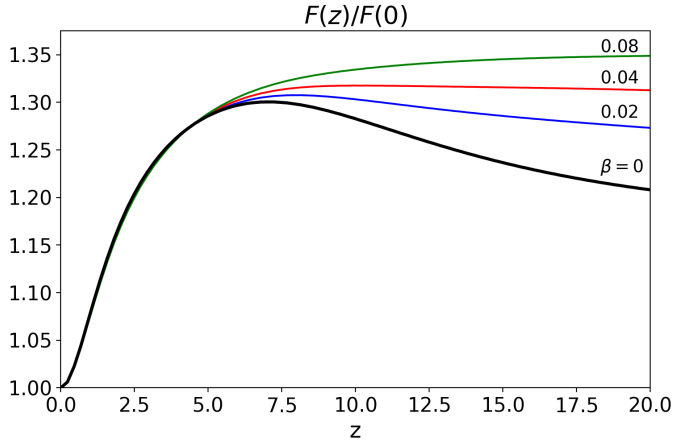

Figure 4.7: Thrust integral over z-const surfaces, as a function of z. The thick black line correspond to $\beta_0 = 0$. The other lines are for simulations with $\beta_0 = 0.02$ (blue line), 0.04 (red), 0.08 (green) as indicated in the plot. Values have been normalized with the total momentum flux at the thruster exit.

Figure 4.7 displays the thrust force $F(z)$ normalized with $F(0)$, the initial momentum flux of the plasma coming out of the sources (directed ion momentum plus electron thermal momentum). Positive magnetic thrust is produced initially, in the first part of the expansion. When the plasma approaches the bend in the magnetic lines and the shock, magnetic thrust plateaus, and thereafter, a minor contribution of negative thrust (i.e. magnetic drag) results by which $F(z)$ decreases by a small amount. As indicated above, this is a natural consequence of the closed shape of the inner magnetic lines and the maps of n, u_{ye}, which give rise to a negative axial magnetic force density near the symmetry plane in the second part of the expansion, as shown in figure 4.6. In the present simulation with $\beta_0 = 0$, the negative contribution decreases $F(z)/F(0)$ about an 8% at $z = 20$ with respect to its maximum, which occurs at $z \simeq 7$.

4.3.2 Effect of the plasma-induced magnetic field

Figure 4.8 displays the normalized plasma-induced magnetic field $\boldsymbol{B}_p/(\beta_0 B_{a0})$, computed from the j_y current density corresponding to the $\beta_0 \to 0$ limit. To mitigate the influence of the plasma currents beyond the simulation domain on the solution, the peripheral part of the results has been cut out from this and following plots.

As noted before, $j_y B_a$ is essentially independent of B_{a0} in the low ion magnetization regime under consideration. Consequently, by virtue of equation (4.2), the dimensionless group $B_p/(\beta_0 B_{a0})$ is also essentially independent of β_0 and B_{a0}. The direction of $\boldsymbol{B}_p$ opposes the applied one in the proximity of the symmetry plane, and points roughly axially downstream far from it. Hence, the trend of $\boldsymbol{B}_p$ is to stretch the MA downstream as β_0 increases.

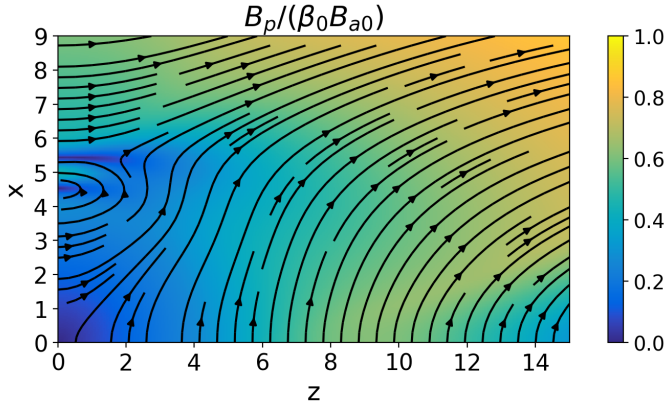

Figure 4.8: Induced magnetic field strength and lines derived from the out-of-plane plasma current j_y, normalized with $\beta_0 B_{a0}$.

Figure 4.9 displays the self-consistent total magnetic field $\boldsymbol{B} = \boldsymbol{B}_a + \boldsymbol{B}_p$ and the streamlines for $\psi_B = \psi_{Ba} + \psi_{Bp}$ for different values of β_0. As β_0 is increased from 0, $\boldsymbol{B}_p$ gains relative importance. The main effect is the modification of the geometry of the central lines of the MA, which are stretched downstream. The separatrix line displaces downward, and some inner magnetic lines that intersected the symmetry plane for $\beta_0 = 0$ are converted into outer lines that go around along the periphery of the domain. As the fraction of inner lines shrinks and the fraction of outer lines grows, more magnetic lines can carry electron current away from the device.

For the larger values of β_0 shown, a region of very low magnetic field strength forms near the symmetry plane and the separatrix eventually intersects with it, forming an 'X' point at which $\boldsymbol{B} = \boldsymbol{0}$, visible for $\beta_0 = 0.08$ in figure 4.9. This brings about a topology change of the MA, which now features a new magnetic region that forms beyond the 'X' point, whose magnetic lines are disconnected from the upstream plasma sources.

While the general characteristics of the plasma expansion are qualitatively similar to the $\beta_0 = 0$ case, the value of β_0 has a major effect on the generated magnetic thrust $F(z)/F(0)$. Figure 4.7 displays the evolution of the thrust force as a function of β_0. It is evident that, while the initial part of the curve roughly coincides for all cases, the stretching of the MA reduces the negative drag contribution that occurs downstream. Indeed, as β_0 increases, the magnetic thrust force generated within the domain rises. For $\beta_0 = 0.04$, $F(z)/F(0)$ remains almost flat after a weak maximum, and for $\beta_0 = 0.08$, the local maximum disappears altogether, with the relative thrust gain $F(z)/F(0)$ increasing by 10% at $z = 20$ with respect to $\beta_0 = 0$.

These results suggest that the plasma-induced field $\boldsymbol{B}_p$ plays a central role in shaping the expansion and the propulsive performance of the device.

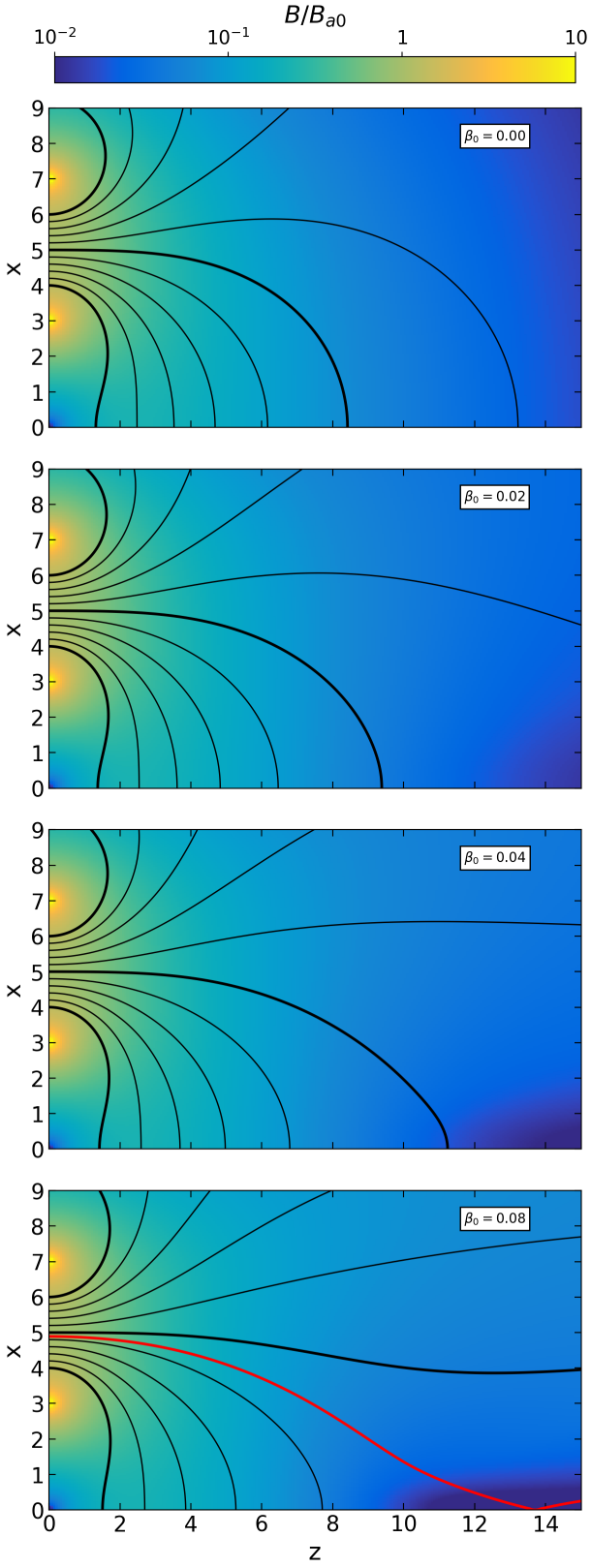

Figure 4.9: Dimensionless total magnetic field $\boldsymbol{B} = \boldsymbol{B}_a + \boldsymbol{B}_p$ strength and streamlines for $\beta_0 = 0$, 0.02, 0.04 and 0.08. Magnetic lines (black) are included in the plots for reference (thicker lines correspond to edges and center of the plasma source). The separatrix line in the last case is shown as a red line.

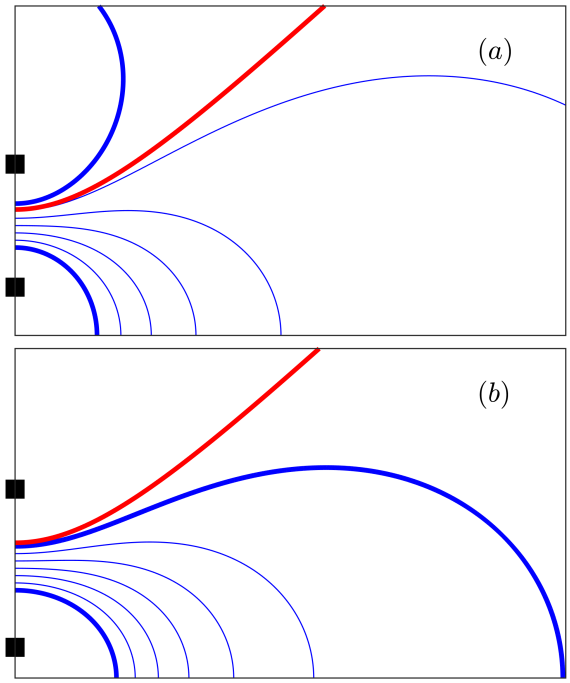

Figure 4.10: Sketch of two MA configurations with $\beta_0 = 0$: open arch (a) and closed arch (b). Lines represent magnetic field lines. Thicker blue lines correspond to the edges of the plasma source. The red line is the separatrix ($\psi_B = 0$). Black squares represent the position of the magnetic field generators.

4.4 Discussion

The results from the previous section merit additional discussion. Firstly, the location of the separatrix line and its effect on electron currents deserves closer inspection, as the global current-free condition is an essential one that must be satisfied by any plasma thruster operating in space. It is possible to distinguish different types of MA, depending on the connectivity of the magnetic lines passing by the plasma source exit with the symmetry plane:

1. If there are both inner lines and outer lines (as defined in section 4.2) passing through the plasma source, an *open arch* is formed as sketched in figure 4.10(a). This occurs when the separatrix falls within the limiting magnetic lines at the edges of the source, it is the relevant type of MA for tightly-packed magnetic generators around the sources, and the one simulated in this work. The plasma expansion in the MA can be globally current-free, as long as the electron current in the lines above the separatrix balances the emitted ion current. A variant of this configuration has the last magnetic line passing by the lower edge of the source intersecting the thruster exit plane, rather than

the symmetry plane.

2. If all magnetic lines passing through the outlet are inner lines, we have a *closed arch* as in figure 4.10(b). In this case, all plasma-carrying lines lie below the separatrix. No electron current can be extracted from the plasma thrusters in the fully-magnetized-electrons, collisionless, $\beta_0 = 0$; this is a consequence of electrons having zero perpendicular velocity, $u_{\parallel e} = 0$ in this limit. Hence, the 'closed' MA cannot be current-free without invoking additional effects. This configuration occurs e.g. for larger separation of the magnetic field generators from the source.

3. Yet another magnetic configuration could be discussed, if all the magnetic lines that pass through the outlet are outer lines. In this case (not sketched), there is no real "arch", and the separatrix falls below the lower edge of the plasma source. This situation would arise when e.g. the plasma sources are not concentric with the magnetic field generators, and is considered of lesser practical interest.

Interestingly, as shown in section 4.3.2 the downward displacement of separatrix line as β_0 is increased may cause a change of MA type. In particular, a closed arch is expected to become an open arch for a sufficiently high value of β_0.

Secondly, even in the strict $\beta_0 = 0$ limit, collisions and an out-of-plane electric field E_y are mechanisms outside of the present model that could relax the electron transport in the perpendicular direction, thus enabling $u_{\perp e} \neq 0$ and, as a side effect and as dictated by the continuity equation, allow $u_{\parallel e} \neq 0$ (and therefore electron current extraction from) even on inner magnetic lines.

The main effect of non-zero collisions on the in-plane electron transport can be understood by including a new term in electron momentum equation (4.5), which now becomes

$$0 = -\nabla(nT_e) + n\nabla\phi - n\boldsymbol{u}_e \times \boldsymbol{B} - \boldsymbol{R}_e, \tag{4.25}$$

where $\boldsymbol{R}_e = nm_e\nu_e\boldsymbol{u}_e$ is a simple representation of the collisional term. The y projection of this equation yields

$$u_{\perp e}B = \chi^{-1}u_{ye}, \tag{4.26}$$

with $\chi = B/(m_e\nu_e)$ the local Hall parameter. Hence, a perpendicular electron flux arises, with $\boldsymbol{u}_{\perp e} \neq 0$ pointing in the direction opposite to the confining $-eu_{ye}B\mathbf{1}_\perp$ force.

An electric field in the out-of-plane direction, $E_y\mathbf{1}_y$, can also enable perpendicular electron flux. The $\boldsymbol{E} \times \boldsymbol{B}$ drift induced by this field generates a collisionless $u_{\perp e}$. This mechanism may play a role e.g. in 3D MA expansions, where E_y may arise

if the plasma undergoes lateral polarization, but is not present in the 2D planar geometry studied here.

Thirdly, another major aspect to be discussed is the validity of the electron model. The profile of H_e that is defined at the upstream plane by the boundary conditions on n, T_e, and ϕ fully determines H_e in the rest of the domain, and therefore H_e', which dictates u_{ye} and defines the magnetic force density in the plume. The map of H_e, together with the map of n, also defines the electrostatic potential ϕ in the plume. As such, H_e has a central role on the MA plasma dynamics. However, while it is reasonable to prescribe H_e on the plasma-carrying magnetic lines that pass through the source, it is not evident what should be the condition on the external lines outside of this main magnetic tube where plasma density is negligible. Here, in this first simulation, we have opted to define H_e there by setting $n \simeq 0$ and $\phi = 0$ at the upstream plane for those lines. A similar problem arises in cases with $\beta_0 > 0$, if an 'X' point forms that bears a new magnetic regions beyond it, disconnected from the plasma sources, as discussed in section 4.3.2. In this case, we have extended the value of H_e on the last magnetic line before the 'X' point to this new region. Incidentally, note that if H_e were constant everywhere (which can always be achieved with the right choice of ϕ upstream), there would be no u_{ye} and hence no magnetic force on the electron fluid, and the magnetic guiding effect of the MA would disappear; this conclusion applies to traditional MNs too [20].

The electron model may need to be revisited and include inertia effects, finite Larmor radius effects, and/or more advanced closure relations based on a kinetic description, which may play a non-negligible role in some of the regions mentioned above. Altogether, these effects may modify the H_e conservation law and the parallel and perpendicular transport of electrons. Similarly, the assumption of quasineutrality may need to be dropped in favor of integrating Poisson's equation, in low density regions.

Fourthly, the applicability of the 2D planar MA model to describe the actual 3D MA remains to be assessed. While it is currently expected that the planar model captures the essence of the mechanisms at play in the actual MA, adding bounds to the plasma in the third dimension can have additional effects, such as the possible set up of a polarization E_y field that further changes the axial dynamics due to the $\boldsymbol{E} \times \boldsymbol{B}$ drift as discussed above. Bounds in the y direction also demand the closure of out-of-plane plasma currents j_y, which will modify the plasma solution and the plasma-induced magnetic field with respect to the 2D planar ones. Additionally, due to the additional dimension, the plasma expansion is stronger in 3D than in 2D, resulting in a faster-decreasing plasma density and electrostatic potential.

Fifthly, it is noted that the present model with cold ions neglects the ion temperature increase that is expected to occur across the shock structure seen in the solution. Including finite ion temperature and the ion energy equation in the model

would be a necessary first step to study these aspects consistently. Alternatively, ions could be modeled as two distinct species, representing the ion beams coming from each plasma source, and overlapping in the interaction region. Ultimately, the correct treatment of the collisionless shock requires a kinetic model.

Lastly, we note that while the MA model remains to be validated against experiment directly, it relies on similar hypothesis to those of the MN model of reference [20]. That model has shown good agreement with existing laboratory measurements in the literature, in particular the plasma expansion and magnetic thrust generation [93, 94], ion-inertia-driven plasma detachment [95], and the role of the plasma-induced magnetic field [96].

4.5 Summary

A MA is expected to form when the MNs of two EPTs with opposing polarities interact. It is also the topology of the magnetic accelerator in the novel MAT concept. A first model of the external expansion of a MA has been presented, which already describes much of its interesting plasma physics in spite of its simplifying assumptions.

The ions are seen to form a free jet that traverses the closed lines of the magnetic field, even if electrons are fully magnetized. An oblique shock structure forms when the two beams coming out of the two thruster outlets meet. Electron equations reduce to algebraic relations in the inertialess, fully-magnetized, polytropic, collisionless limit of the model, and describe how the out-of-plane electron velocity is fully determined by the magnetic field map and the upstream boundary conditions.

Electron current can only be extracted along magnetic lines that do not connect the two sources through the symmetry plane (i.e., outer lines), in the limits of the model. For a given applied magnetic field map, these lines are delimited by a separatrix line; the location of this separatrix with respect to the thruster outlet determines the type of MA. In the open MA considered here, a globally-current free solution of the plasma expansion is possible. If all the lines passing through the outlet connected with the symmetry plane, no electron current could be extracted in the strict fully-magnetized, collisionless, planar, $\beta_0 = 0$ limit of the electron model, and other mechanisms would need to be included to enable it.

Net positive magnetic thrust is produced from the interaction of the out-of-plane plasma currents and the applied field. These currents are dominated by the electron contribution at low and mild ion magnetization strengths. It is observed that most of the positive contribution to thrust comes from the initial stages of the expansion, while a small negative (drag) contribution results from the region where the magnetic lines bend back to the device.

The plasma-induced magnetic field $\boldsymbol{B}_p$ has been shown to stretch the MA downstream when $\beta_0 \neq 0$, and to increase the fraction of electron current-carrying magnetic lines that pass through the source. The stretched arch has a smaller negative drag contribution to thrust, and indeed a monotonically increasing magnetic thrust curve results already for moderate values of β_0. Hence, modeling the plasma-induced magnetic field is essential for the correct description of the MA dynamics. This contrast with the case of an axisymmetric MN, where the deformation of the field caused by $\boldsymbol{B}_p$ plays a rather secondary role in thrust generation at small β_0.

We conclude that the present preliminary analysis supports the feasibility of the MA topology for plasma acceleration and magnetic thrust generation, and therefore, we identify no showstopper to flying pairs of EPTs with opposing polarities or the novel MAT configuration. More advanced models and laboratory experiments must ensue to fully ascertain this claim.

Chapter 5

Neutral Dynamics and Facility Effects in Magnetic Nozzles

The following chapter investigates the effect of neutral dynamics and the so called facility effects on the behaviour of plasma expanding in a cylindrical nozzle. To begin with, the model used is introduced, this three-fluid model considers several inter-species collisions. Next, we present the different simulation scenarios that are considered, these different scenarios include the introduction of neutrals from a non-ideal source as well as the addition of a background of neutrals reproducing the existing conditions in the ground testing of EPTs. This way we show that the ion fluid is not strongly affected in the envisaged operating point in MNs. Attention is also paid to the effect of these collisions on the momentum of the electrons which are shown to be affected by the collisions particularly for some electrical boundary conditions. Moreover, we show strong collisional losses due to inelastic collisions of electrons with neutral that affect the thermodynamics of the electrons and reduce the performance of the nozzle. The content of this chapter is a verbatim reproduction of the submitted article [97] and is one of the contributions of this thesis to the ZARATHUSTRA project. Kindly excuse any redundant information which might be present in the former chapters of this work, particularly in the introduction and the model sections. These offer however, deeper detail into the technicalities of the topic in question in the present chapter.

5.1 Introduction

Electrodeless plasma thrusters (EPTs) have gained interest from the space propulsion community in the last decades thanks to their theorized advantages with respect to other well-established electric propulsion technologies[2, 17]. EPT devices such as

the Helicon Plasma Thruster (HPT) [98, 99, 100, 78, 85] and the Electron-Cyclotron Resonance thruster (ECRT) [15, 87, 101, 102, 50] are now under development. In these devices, plasma acceleration occurs in a so-called magnetic nozzle (MN) [103, 20] that, similarly to a de Laval nozzle in chemical propulsion, converts (electron) thermal energy into (ion) directed kinetic energy. The lack of electrodes and neutralizing cathode in EPTs offers a number of possible advantages compared to other, well-established propulsive technologies, such as potentially longer lifetimes, the possibility to use virtually any substance as propellant [104], simpler scalability to higher and lower power levels, wider thrust-specific impulse throttleability, and even the possibility to exert thrust vectoring without moving parts [21].

Several models have been employed to study the expansion of magnetized plasma in a MN. The most fundamental approach is the continuous kinetic modelling which solves the Vlasov equation directly and is usually limited to 1D scenarios [105, 38]. To overcome this inherent limitation of continuous kinetic modelling, full particle-in-cell (PIC) models [106, 107, 108] have been employed, these models are however usually limited to two dimensional geometries due to their high computational cost. Another alternative is the hybrid approach in which electrons are modelled as a fluid while ions and neutrals are modelled as particles [109, 110]. This approach has proved good agreement with experimental results and even simulations of the plasma-wave coupling has been achieved [111] . However, parametric studies require a computationally cheaper option, a role fulfilled by full-fluid simulations in which one solves the equations for macroscopic balance of mass, momentum and other momenta of the Boltzmann equation [20, 112, 36]. A good example of this is DIMAGNO, a collisionless two-fluid model which has been employed to study the mechanisms for magnetic thrust generation and MN efficiency [20], the detachment of ions [79], and the effect of the self-induced magnetic field at non-zero plasma beta [55].

However, while the collisionless assumption is a reasonable one in warm, fully-ionized plasma jets expanding into vacuum, it is questionable in current EPT laboratory experiments, where the mass utilization efficiency is not high, and where background pressure can affect the MN-plasma dynamics. The performance of other EP technologies such as HET has been shown to improve with varying background pressure [31, 113]. In the case of MNs the understanding of the behaviour of nozzle performance with background pressure is yet incomplete. Several experiments performed at ONERA [114, 26] and Michigan [52] have pointed towards thrust and efficiency losses due to increased background pressure, the latest authors attributed these losses to inelastic electron-neutral collisions that reduce available power to accelerate the ions. From the simulation point of view, Zhou and Sanchez-Arriaga [115] used a kinetic model to show that the thermodynamics of electrons is only lightly affected by electron collisionality in paraxial nozzles. Finally, full-PIC simulations [116] have shown performance losses MNs in very poor vacuum conditions;

however, significant performance losses where not observed at background pressures comparable to the ones observed in the aforementioned experiments. Despite the relevance of this work, some points such as the effect of the different collisions on the thrust characteristics of the nozzle and the comparison with the key experimental measurements in [52] where not assessed.

Another notable effect that facility testing may have on the expansion of plasma in the magnetic nozzle is that of finite chamber size. The electrically conducting wall of the vacuum chamber is expected to change the behaviour of the electron population. This effect was already mentioned in [20] where it was noted that a change in the electrical boundary conditions strongly affected the electron current found in the plume. Some experiments have been performed by Baldinucci and collaborators [117] where measurements showed that the addition of an electrically conducting barrier downstream decreased thrust by up to 10%.

The present article expands on the initial work by Ahedo and Merino [20] by, firstly, modelling the neutral population as an additional fluid and including the effect of ionization and charge-exchange (CEX) collisions on the heavy species. This allows us to gauge the importance of collisions in the MN plasma expansion and the propulsive performances when propellant utilization efficiency is not 100%, and in the presence of background pressure. The ion velocity distribution function (IVDF) is estimated in these cases a posteriori, showing the development of a slow, background ion population. We also go beyond that seminal work by solving the plasma equations in the peripheral region beyond the last plasma magnetic line in the MN, observing the buildup of a potential barrier. Secondly, under the assumption that collisions are non-dominant, we evaluate perturbatively the effect of excitation, ionization, and elastic collisions on the electron fluid, and discuss the influence of vacuum chamber boundary conditions (metallic or dielectric walls) on electron streamlines, postulating that this aspect can change the plume globally and affect its divergence angle; this study is an expansion of the one found in [46]. While a polytropic closure relation is employed in the electron model, the energy cost of inelastic collisions, and the enhancement of plasma mass flow in the plume, are taken into account to compute the MN efficiency consistently.

The following sections of this paper are organized as follows. Section 5.2 introduces the three-fluid model, making special emphasis in its improvements with respect to previous works. Numerical integration for the equations of the model is tackled in subsection 5.2.3. Section 5.3 describes the simulation setup, presents the results for the different cases considered, and analyzes the plasma response. Finally, section 5.4 gathers the main conclusions of the study.

5.2 Three-fluid Model

We consider a plasma jet of initial radius R_0 composed of electrons (e), singly-charged ions (i), and neutrals (n). The plasma is assumed quasi-neutral everywhere, $n_i = n_e$, as it expands from a set of prescribed upstream conditions, into a diverging, axisymmetric, applied magnetic field $\boldsymbol{B}$ that can be expressed through the derivatives of a magnetic stream function ψ,

$$\boldsymbol{B} = \nabla\psi \times \mathbf{1}_\theta. \tag{5.1}$$

Here we have introduced the unit vector in the azimuthal direction, $\mathbf{1}_\theta$. We further introduce two right-handed, orthonormal vector bases: the cylindrical $\{\mathbf{1}_z, \mathbf{1}_r, \mathbf{1}_\theta\}$, and the magnetic $\{\mathbf{1}_\parallel, \mathbf{1}_\perp, \mathbf{1}_\theta\}$, with $\mathbf{1}_\parallel = \boldsymbol{B}/B$ and $\mathbf{1}_\perp = \mathbf{1}_\theta \times \mathbf{1}_\parallel$ in the meridional plane. Lastly, we also introduce the unit normal pointing in the inward direction at the boundaries of the domain, $\mathbf{1}_n$. Without loss of generality, we shall assume that $\boldsymbol{B}$ points downstream at the MN throat.

5.2.1 Ions and neutrals

In the magnetic nozzles of HPTs and ECRTs the energy is transferred to the plasma in the form of electron thermal energy. Hence, they are characterized by electron temperatures of the order of tens of electronvolts [118, 119] and ion temperatures of a fraction of an electronvolt [48] and therefore $T_e/T_i \gg 1$. For this reason, ion temperature is usually neglected in fluid simulations [20] or considered constant [112]. However, a rising ion temperature is one of the main indicators of collisional effects in MNs, this is attributed to late ionization in the plume and other collisional processes which broaden the ion velocity distribution function (VDF). For this reason our model includes ionization and charge exchange (CEX) collisions and retains the equations for ion and neutral internal energy recognizing that the temperature of neither of the heavy species will play a major role in the expansion.

Under the assumption that the convection of thermal energy dominates over heat conduction the fluid equations for the conservation of mass, momentum and internal energy for both species can be written as:

$$\partial_t n_e + \nabla \cdot (n_e \boldsymbol{u}_i) = S_{ion}, \tag{5.2}$$

$$\partial_t n_e \boldsymbol{u}_i + \nabla \cdot (n_e \boldsymbol{u}_i \boldsymbol{u}_i + \frac{1}{m_i} n_e T_i) = -\frac{e n_e}{m_i} \nabla \phi + \frac{e n_e}{m_i} \boldsymbol{u}_i \times \boldsymbol{B} + S_{ion} \boldsymbol{u}_n + S_{CEX}(\boldsymbol{u}_n - \boldsymbol{u}_i) \tag{5.3}$$

$$\partial_t \left(\frac{3}{2} n_e T_i \right) + \nabla \cdot \left(\frac{5}{2} n_e T_i \boldsymbol{u}_i \right) = \boldsymbol{u}_i \cdot \nabla n_e T_i + S_{ion} \left(\frac{3}{2} T_n + \frac{m_i}{2} (\boldsymbol{u}_i - \boldsymbol{u}_n)^2 \right) + S_{CEX} \left[\frac{3}{2} (T_n - T_i) + \frac{m_i}{2} (\boldsymbol{u}_i - \boldsymbol{u}_n)^2 \right] \tag{5.4}$$

$$\partial_t n_n + \nabla \cdot (n_n \boldsymbol{u}_n) = -S_{ion}, \tag{5.5}$$

$$\partial_t n_n \boldsymbol{u}_n + \nabla \cdot (n_n \boldsymbol{u}_n \boldsymbol{u}_n + \frac{1}{m_i} n_n T_n) = -S_{ion} \boldsymbol{u}_n + S_{CEX}(\boldsymbol{u}_i - \boldsymbol{u}_n) \tag{5.6}$$

$$\partial_t \left(\frac{3}{2} n_n T_n \right) + \nabla \cdot \left(\frac{5}{2} n_n T_n \boldsymbol{u}_n \right) = \boldsymbol{u}_n \cdot \nabla n_n T_n - S_{ion} \frac{3}{2} T_n + S_{CEX} \left[\frac{3}{2} (T_i - T_n) + \frac{m_i}{2} (\boldsymbol{u}_i - \boldsymbol{u}_n)^2 \right] \tag{5.7}$$

Here the term S_{CEX} represents the volumetric rate for CEX collisions and we have used $m_n = m_i$. The expressions for the rates of all collisions included in this study can be found in the appendix 5.A.

Observe that collisional terms in eqs. (5.4) and (5.7) are not symmetric, this is due to the fact that collision between species with different fluid velocities tend to raise both of their temperatures.

We further assume that neutrals are introduced in the domain without any rotation, ($u_{\theta n} = 0$), hence, the only mechanism that could induce a rotational velocity in the neutral fluid is the exchange of azimuthal momentum with ions via CEX collisions and, as the swirl current (following the notation in [20]) in electron driven nozzles tends to be small, we disregard the azimuthal component of the neutral momentum equation.

The neutral density in the former equations has two different origins. Some neutrals are introduced in the domain at the nozzle throat simulating a plasma source with imperfect utilization efficiency. Moreover, we define a background density n_b which we manually set as a minimum density for the neutral fluid. This background density is defined by choosing a background pressure p_b which allows us to fix n_b through an ideal gas law $n_b = p_b/T_b$.

To integrate our model it is necessary to impose both boundary conditions (BCs) and initial conditions (ICs). For the ion and neutral fluids, we impose the values of all the conserved variables at the inlet, and no BCs at the outlet as the velocities are supersonic there. On the other hand we impose symmetry conditions on the axis $r = 0$.

5.2.2 Electrons

Electron inertia is assumed negligible, this is equivalent to retaining only zeroth-order Larmor radius effects. Moreover, a polytropic closure relation for electron temperature,

$$T_e = T_{e0}(n_e/n_{e0})^{\gamma_e - 1}, \tag{5.8}$$

is imposed, with a prescribed exponent γ_e. While the polytropic model ignores the kinetic features of the electron expansion, it is known to be a reasonable closure to the experimentally observed non-local electron thermodynamics in the MN[92, 38, 81]. Experimental evidence shows that a ratio of specific heats slightly above isothermal adequately describes the electron cooling rate in many EPTs [44, 45, 120]. On the other hand, kinetic evidence from the work of Zhou [115] shows that electron cooling is only weakly affected by collisionality in the envisaged ranges of operation of a magnetic nozzle with polytropic index varying from 1.218 in the collisionless case to 1.239 in the highest collisionality scenario. Moreover, full-PIC simulations by Andriulli *et al.* [116] demonstrated that the potential drop to infinity and therefore γ_e is very mildly affected by electron collisions against background neutrals in the expected ranges of chamber pressure.

The electron continuity and momentum equations then read:

$$\partial_t n_e + \nabla \cdot (n_e \boldsymbol{u}_e) = S_{ion}, \tag{5.9}$$

$$0 = -\frac{T_{e0}}{n_{e0}^{\gamma_e - 1}} \nabla n_e^{\gamma_e} + e n_e \nabla \phi - e n_e \boldsymbol{u}_e \times \boldsymbol{B} - m_e n_e \nu_e \boldsymbol{u}_e, \tag{5.10}$$

where S_{ion} is the ionization source term, and ν_e represents the effective electron momentum collision frequency due to elastic collisions (with ions and neutrals) and inelastic collisions (excitation, ionization). Collisional related parameters are defined in section 5.A. Dividing by $e n_e B$, the latter equation can be cast as

$$0 = -\frac{1}{eB} \nabla H_e - \boldsymbol{u}_e \times 1_\parallel - \chi^{-1} \boldsymbol{u}_e, \tag{5.11}$$

with $\chi = eB/(m_e \nu_e)$ the local Hall parameter, and H_e the Bernoulli function [20],

$$H_e = \frac{\gamma_e}{\gamma_e - 1} T_{e0} \left[\left(\frac{n_e}{n_0} \right)^{\gamma_e - 1} - 1 \right] - e\phi. \tag{5.12}$$

Writing $\boldsymbol{u}_e = u_{\parallel e} \mathbf{1}_\parallel + u_{\perp e} \mathbf{1}_\perp + u_{\theta e} \mathbf{1}_\theta$ and projecting (5.11) along $\mathbf{1}_\parallel$, $\mathbf{1}_\perp$ and $\mathbf{1}_\theta$ yields equations for $u_{\parallel e}$, $u_{\theta e}$ and $u_{\perp e}$ as functions of the gradient of H_e,

$$u_{\parallel e} = \frac{-1}{\chi^{-1}} \frac{1}{eB} \frac{\partial H_e}{\partial \mathbf{1}_\parallel}, \tag{5.13}$$

$$u_{\theta e} = \frac{-1}{1 + \chi^{-2}} \frac{1}{eB} \frac{\partial H_e}{\partial \mathbf{1}_\perp}, \tag{5.14}$$

$$u_{\perp e} = \frac{-\chi^{-1}}{1 + \chi^{-2}} \frac{1}{eB} \frac{\partial H_e}{\partial \mathbf{1}_\perp} = \chi^{-1} u_{\theta e}. \tag{5.15}$$

In propulsive MNs, electrons must be effectively magnetized for a correct behaviour of the device, which requires a large Hall parameter, $\chi \gg 1$. Otherwise, the confining and guiding effect of the MN breaks down [121]. This condition holds in free space even at low propellant utilization efficiencies in most of the MN, as in the region with the highest collisionality, i.e. the nozzle throat, electrons are strongly magnetized. It also holds in a vacuum chamber experiment, provided that the background pressure is sufficiently low and the relevant mean free paths are long enough. In the far plume, electron demagnetization can override this condition.

In the collisionless limit ($\chi^{-1} = 0$) considered in [20], H_e is uniform along magnetic lines by virtue of equation (5.11), therefore the Bernoulli function is only determined by ψ as $H_e = H_e(\psi)$ and $u_{\theta e}$ is solely dictated by ∇H_e (which points purely in the $\mathbf{1}_\perp$ direction and can be expressed as the derivative of H_e on the magnetic stream-function ψ),

$$u_{\theta e} = \frac{-r}{e}\frac{\mathrm{d}H_e}{\mathrm{d}\psi} \sim \frac{T_{e0}}{eB_0R_0}, \tag{5.16}$$

In this strong electron magnetization limit, the maps of H_e and $u_{\theta e}$ are fully determined by the upstream boundary conditions alone, and can be computed before solving any other aspect of the plasma expansion. Furthermore, $u_{\perp e} = 0$, and $u_{\parallel e}$ become uncoupled from the momentum equation and the rest of the problem, appearing only in the continuity equation, and its steady-state map can be solved for from it and the corresponding boundary conditions after a solution for n_e is found. Indeed, noting that $\nabla \cdot \boldsymbol{B} = 0$,

$$\partial_t n_e + \boldsymbol{B} \cdot \nabla \left(\frac{n_e u_{\parallel e}}{B} \right) = S_{ion}. \tag{5.17}$$

This was the limit electron model introduced in [20].

In the present work, in the understanding that χ^{-1} is small, we also solve the electron expansion to zeroth order in χ^{-1}. This electron solution, advantageous from the computational viewpoint, is then used to find the ion and neutral response. First-order corrections in χ^{-1} to the electron map are then discussed in section 5.3.4, following the perturbative approach introduced in [46]. For this approach to remain valid, we require that $u_{\perp e}/u_{\parallel e} \ll 1$, so that the perturbed electron streamlines do not deviate substantially from the collisionless ones.

Two different conditions for equation (5.17) are explore, namely one imposing local current ambipolarity LCA ($\boldsymbol{j} \cdot \mathbf{1}_n = 0$) at the throat, and another imposing it in the downstream boundary, observe that in the case in which ion magnetization is low this does not imply that global current ambipolarity (GCA) is satisfied as mentioned in [20].

5.2.3 Numerical Integration

At this point, we use equation (5.10) to eliminate the electric potential from the ion momentum conservation equation (5.3) . This way we can write a set of 9 differential equations for the plasma density, three-dimensional ion momentum, ion energy, neutral density, two-dimensional neutral momentum and neutral energy, these equations can be found in the appendix 5.B.

All of these equations are in conservative form, except for the internal energy equations for ions and neutrals, in which the pressure gradient term in the right hand side remains. Note that this situation is not solved by using the total energy equation instead, as in that case the electrostatic gradient term (Joule heating term) is present in the right hand side instead.

The spatial discretization and numerical integration of the problem follow a Discontinuous Galerkin (DG) scheme of order $p = 1$ which is evolved in time with a strong stability preserving Runge-Kutta (SSPRK) method [65] until steady state is reached. The problem is discretized on a triangular mesh of variable size. The cell size is chosen to be a function of $\mathrm{d}H_e/\mathrm{d}\psi$ and therefore is finer in the area close to the throat and becomes coarser downstream and in the side of the plume. The length of a cell edge is $h_{min} = 0.6$ mm in the nozzle throat and $h_{max} = 19$ mm in the downstream upper corner of the domain. The number of cells in the domain is 6017 are used for a total of 162459 degrees of freedom in the problem. The approach is analogous to the one used in [28], although the problem is now extended to include the neutral species, ion and neutral temperature, as well as ionization and charge exchange collisions.

In summary, we write the set of partial differential equations as a single system in quasi-conservative form:

$$\frac{\partial \boldsymbol{Q}}{\partial t} + \nabla \cdot \mathcal{F} = \boldsymbol{G}, \tag{5.18}$$

where

$$\boldsymbol{Q} = \left[n_e, n_e \boldsymbol{u}_i, \tfrac{3}{2} n_e T_i, n_n, n_n \boldsymbol{u}_n, \tfrac{3}{2} n_n T_n\right]^\top,$$

is the vector of unknowns, $\mathcal{F}$ is the flux tensor, and $\boldsymbol{R}$ is the vector containing the right-hand side forcing terms.

A major distinction with [28] is that here the system of equations is not fully in conservative form as indicated above, and the volume integral of $\boldsymbol{R}$ requires the evaluation of gradients of their respective pressures. These terms, while of minor relevance (the temperatures of ions and neutrals are orders of magnitude below that of electrons), cannot be adequately evaluated with the current DG discretization, as elements are not continuous across cell boundaries. In this work we instead project the pressure of ions and neutrals onto a continuous function space of order 2 and its

gradient is then evaluated in this space. The numerical tests in the appendix 5.C verify the suitability of this approach, and show that this projection step recovers the expected convergence of the solution with element order p and element size h.

In order to initialize the simulation the map of $\mathrm{d}H_e/\mathrm{d}\psi$ must be fixed before the equations for the heavy species are solved. To this end, we calculate analytically the value of the stream-function ψ for the whole domain. Since, in our model, the thermalized potential H_e and electron azimuthal angular velocity $eu_{\theta e}/r = -\mathrm{d}H_e/\mathrm{d}\psi$ are only functions of ψ, we can fix their values everywhere in the domain by interpolation of their values at the inlet boundary.

Then, at $t = 0$ we initialize the simulation with a low density background $n_e = 10^{-6} n_{e0}$ for the reference simulation while in the other simulations are initialized with the solution to the reference one. Convergence is reached when the time derivative of the solution vector calculated as

$$\sum_{\forall \text{ nodes}} \sum_{\forall i} \frac{|\boldsymbol{Q}_{i,n+1} - \boldsymbol{Q}_{i,n}|}{t_{n+1} - t_n}$$

with $\boldsymbol{Q}_i$ the components of $\boldsymbol{Q}$, and subindex n the temporal instant; is smaller than 10^{-10}. Once steady-state is reached we calculate the solution to the electron continuity equation using a DG-upwind scheme setting the appropriate boundary conditions in order to obtain current ambipolarity in the desired boundary.

5.3 Results

5.3.1 Simulation cases

In the following, we discuss the physical and numerical setting for the different simulation cases. In all simulations, the MN is generated by a circular current of radius $R_C = 2R_0$, with R_0 the radius of the plasma inlet, in our case $R_0 = 1.8$ [cm] which is in the range of common Helicon and ECR sources [44, 52, 50]. Both the coil and the plasma inlet are centered at $(z, r) = (0, 0)$ and the magnetic field, is chosen to be 200 G in that point, this value is representative of a 5.8 GHz ECR thruster [50], nonetheless, it is comparable to other electron-driven MN thruster prototypes [52, 44]. The applied magnetic field $\boldsymbol{B}_a$, is depicted in figure 5.1. Moreover, the electron temperature at the centre of the nozzle is set to $T_{e0} = 10$ eV and the electron polytropic exponent to $\gamma_e = 1.2$, in keeping with the discussion in the model section 5.2.

The domain of integration is depicted in figure 5.1 along with the different boundaries of the simulation in which the BCs are imposed.

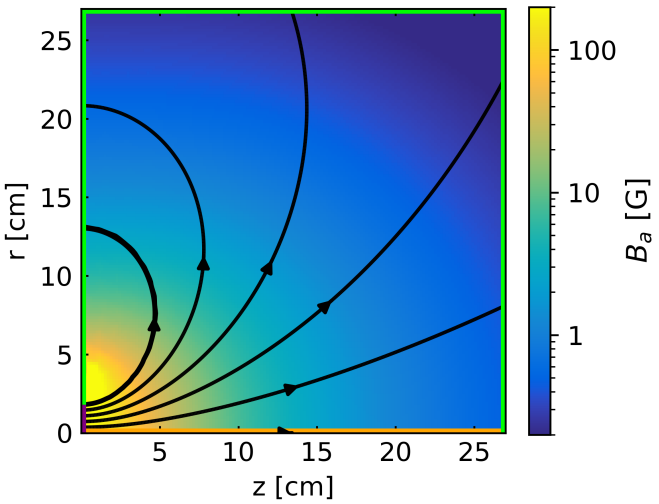

Figure 5.1: Applied magnetic field $\boldsymbol{B}$. Black lines depict magnetic streamlines, the thicker line depicts the magnetic streamline up to which 99.8% of plasma is injected. The purple line depicts the MN throat boundary conditions where plasma enters the domain, the orange line depicts the symmetry axis while the green lines represent the supersonic outlet.

In order to define all the boundary conditions we define first the utilization efficiency with the entrance plasma conditions, as:

$$\eta_{u0} = \frac{\dot{m}_{i0}}{\dot{m}_0} = \frac{\dot{m}_{i0}}{\dot{m}_{i0} + \dot{m}_{n0}} \tag{5.19}$$

Where $\dot{m}_{s0}$ is the mass flow rate for species s at the throat.

The values of the different background pressures are chosen to be in the range of those analyzed by Wachs and Jorns [52]. The values of utilization efficiency range from a perfect ionization case to an $\eta_u = 0.5$ case that is close to the the utilization observed in some prototypes [50, 16] although higher utilization efficiencies of around 0.6 have been observed [122].

The inlet boundary conditions are:

$$\begin{aligned} n_\alpha(0,r) &= n_{\alpha 0} 10^{-3(r/R_0)^2} &&, \boldsymbol{u}_\alpha(0,r) = M_{\alpha 0}\tilde{c}_\alpha(0,r)\mathbf{1}_z; \\ T_\alpha(0,r) &= 0.078 \text{ eV} &&, T_e(0,0) = 10 \text{ eV}; \\ \phi(0,r) &= 0; \end{aligned} \tag{5.20}$$

where the sub-index α refers to either ions or the neutrals. Note here that the relevant speed for ions here is $\tilde{c}_i = \sqrt{\gamma_e T_e/m_i}$ while that of the neutrals is $\tilde{c}_n = \sqrt{(5T_n)/(3m_i)}$ both of which are obtained by linearization of the system in equation (5.18). The ions are introduced with an axial velocity equal to a fraction of their local sound speed so that the ion Mach number is M_{i0} across the nozzle throat.

Plasma is then introduced at the nozzle with a Gaussian density profile which falls three orders of magnitude across the radius of the inlet. The values at the

centre of the throat for ion and neutral density are set according to the utilization efficiency of the source while keeping a fixed mass flow rate of $\dot{m}_0 = 0.015$ mg/s of xenon in the throat. As in previous work [28], the Gaussian inlet profile is extended up to the border of the coil ($r = 2R_0$) to avoid sharp gradients in the inlet boundary, however the ion flux entering the domain through the boundary from $r = R_0$ to $r = 2R_0$ represents less than 0.2% of the total flux, and therefore this does not change noticeably the global dynamics of the nozzle. Additionally, the neutral background temperature is chosen to be $T_b = 900$ K. The choice of a temperature higher than room is influenced by two factors. First, neutrals have a relatively large residence time in the ionization chamber and are therefore expected to thermalize with its wall which may be heated due to ion bombardment and other processes, in addition, the multiple wall-recombination and reionization processes will also rise neutral temperature.

In order to gauge the effect of background pressure and neutral density we perform simulations varying both p_b and η_u while keeping all other free parameters of the simulations fixed. A list of all the simulation cases can be found in the first few rows of table 5.1 in which the values for η_u and p_b are specified. There, simulations are labelled as *R* for the reference simulation without background pressure and with perfect utilization, *U1*, *U2* and *U3* designate the simulations with different source utilization efficiencies, while *B1*, *B2* and *B3* designate the simulations with different background pressures. Finally, simulation *UB* includes both effects.

The sonic point in the magnetic nozzle of EPTs is usually argued to be located at the nozzle throat [103]. However, some experimental measurements have shown that sonic transition happens downstream from the throat [123, 51, 124]. On the other hand, some simulations claim that the sonic transition is not strongly influenced by the position of the magnetic throat and can indeed take place upstream from it [110]. Some collisional simulations only solving the divergent part of the magnetic nozzle show a local drop in the ion velocity close to the throat [116]. This artifact is produced by the incorrect matching of the ionization chamber and the plume, in order to avoid this, M_{i0} is chosen such that the expansion is monotonic in the whole domain, in our case this happens for $M_{i0} = 0.4$. On the other hand, neutrals are introduced with an axial velocity equal to their sound speed and their density is also set to a Gaussian falling three orders of magnitude in the side of the nozzle throat.

5.3.2 Response of highly magnetized electrons

As described in subsection 5.2.2, our MN model employs a massless, collisionless electron solution to integrate the ion and neutral equations. In a latter section 5.3.4, the leading order corrections due to collisions and electron inertia are evaluated.

The main advantage of this approach is that it allows us to solve the electron

Simulation	R	$U1$	$U2$	$U3$	$B1$	$B2$	$B3$	UB
η_{u0}	**1.0**	**0.9**	**0.7**	**0.5**	1.0	1.0	1.0	**0.5**
p_b[mPa]	**0.0**	0.0	0.0	0.0	**0.5**	**2.0**	**4.0**	**4.0**
$n_{e0}[10^{17}m^{-3}]$	3.00	2.73	2.17	1.59	3.00	3.00	3.00	1.59
$n_{n0}[10^{17}m^{-3}]$	0.00	1.36	2.73	6.80	0.402	1.61	3.22	6.80
$u_i(z_L)$ [km/s]	7.399	7.374	7.369	7.363	7.343	7.187	6.983	6.938
$\dot{m}_i(z_L)/\dot{m}_{i0}$	1.000	1.008	1.023	1.039	1.013	1.056	1.121	1.126
$R_{95\%}(z_L)$ [cm]	11.78	11.87	11.87	11.96	12.05	12.59	13.50	13.41
P^*_{in} [mW]	191.2	163.3	112.4	68.48	191.3	190.5	189.5	68.09
P_{coll} [mW] (eq. (5.27))	0.000	1.523	3.737	4.719	6.148	26.50	56.80	30.81
P_{in} [mW] (eq. (5.24))	191.2	164.8	116.2	73.20	197.4	217.0	246.3	98.90
P_{coll}/P_{in}	0.000	0.009	0.032	0.064	0.031	0.122	0.231	0.311
$\tilde{\gamma}_e$ (eq. (5.28))	1.2	1.201	1.203	1.206	1.204	1.218	1.244	1.249
$F_i(0)$ [μN] (eq. (5.30))	15.78	13.81	10.87	7.92	15.44	14.97	14.45	7.73
$F_e(0)$ [μN] (eq. (5.30))	46.12	41.91	32.08	22.39	46.61	47.28	48.04	22.6
$F_n(0)$ [μN] (eq. (5.30))	0.0	0.56	1.68	2.80	0.0	0.0	0.0	2.87
ΔF_i [μN] (eq. (5.31))	70.0	67.8	54.5	40.5	71.8	73.4	74.9	40.11
ΔF_e [μN] (eq. (5.32))	-42.9	-39.5	-31.6	-23.4	-43.3	-43.8	-44.5	-23.7
ΔF_n [μN] (eq. (5.33))	0.0	-0.0169	-0.0411	-0.0510	0.278	1.13	2.24	1.04
F [μN] (eq. (5.30))	89.0	84.6	67.5	50.2	90.9	92.9	95.2	52.6
η_{MN} (eq. (5.34))	0.915	0.912	0.851	0.721	0.934	0.897	0.840	0.590
κ_{MN} (eq. (5.35))	0.851	0.951	1.178	1.439	0.889	0.924	0.963	1.418
κ_P (eq. (5.35))	1.000	0.991	0.968	0.936	0.969	0.878	0.769	0.689
κ_F (eq. (5.35))	1.076	1.075	1.074	1.072	1.085	1.106	1.134	1.207

Table 5.1: Free parameters of the simulation (first four rows) and relevant global performance parameters. In the fourth line $n_{n,max}$ represents the neutral density at the center of the throat in simulations *U1, U2, U3* and *UB* and the neutral background density in simulations *B1, B2* and *B3*, in all cases this is the maximum neutral density encountered in the domain.

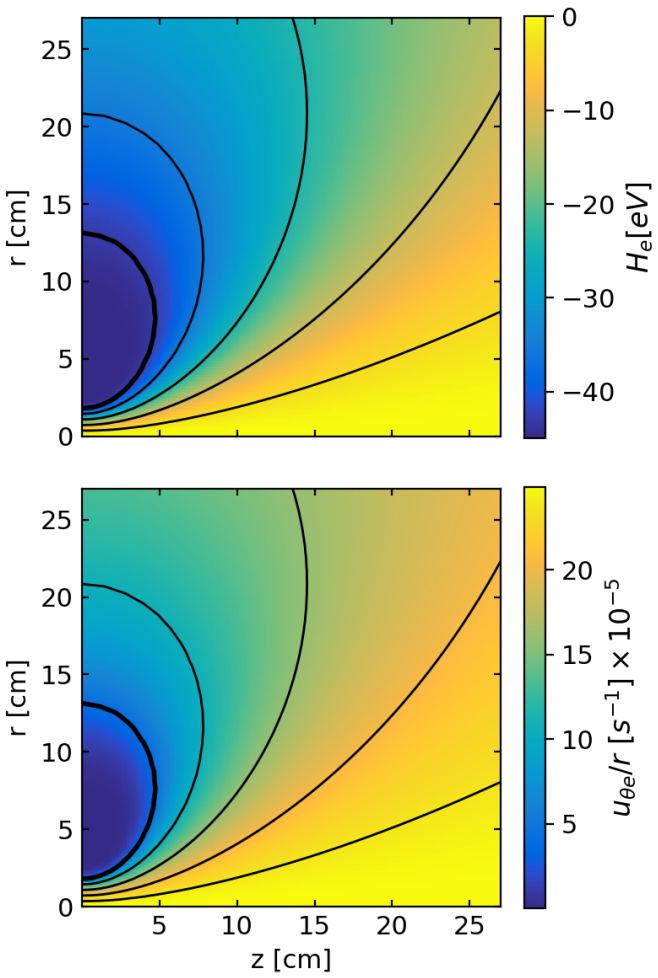

Figure 5.2: Maps of H_e and electron azimuthal angular velocity $u_{\theta e}/r$ fixed by the throat boundary conditions and the applied magnetic field in the $\chi^{-1} = 0$ limit.

momentum equation algebraically to find the map of H_e from the upstream boundary conditions, as this quantity is conserved along magnetic streamlines by virtue of the collisionless limit of (5.13). In turn, this fixes the electron azimuthal velocity, which is obtained from (5.14). Figure 5.2 shows the maps of H_e and $u_{\theta e}$, indicating that the resulting electron azimuthal velocity is positive everywhere in the domain resulting in a diamagnetic azimuthal current and therefore radial confinement and positive magnetic thrust [46].

5.3.3 Ion and neutral response

Remarkably, the ion expansion in the collisionless regime (R) and in the various explored collisional cases ($U1, U2, U3, B1, B2, B3, UB$) are very similar on first sight.

Figure 5.3 (a) shows the electric potential in simulation UB. As in previous studies, it is found that the potential drops axially and radially in the main plume. Here, we find that for the chosen boundary conditions, the potential also grows

radially in the peripheral region. A low potential region exists between the main plume and the lateral part. Figure 5.3 (b) shows the ion current density ($\tilde{\jmath}_i$) in the meridian plane. Most of the ion current is carried by the main plume and is inward-detached with respect to magnetic lines, meaning that the divergence angle of the former is less than that of the latter. The lower density plasma in the peripheral region is originated at the lateral of the throat, as we extend the plasma inlet up to the coil location; and by ionization events taking place in this region, this numerical artifact is not considered to affect the solution strongly as only 0.2% of the mass flow at the throat is provided by the periphery of the inlet (radii between R_0 and $2R_0$).

Figure 5.3 (c) and (d) show the collisional frequencies for ionization and charge-exchange. While ionizing collisions are more prominent in the surroundings of the nozzle throat, they decrease rapidly away from the source. CEX collisions, on the other hand, remain same-order everywhere in the domain, and thus represent the main collisional contribution on the heavy particles downstream and in the periphery. Even though it is not shown here, ion azimuthal velocity is negligible compared to its electron counterpart in all simulations as is expected for $T_e \gg T_i$ when ions are introduced without rotation[20].

As mentioned before the expansion is very similar in all the simulated scenarios. To quantify the effect of collisions on the radial behaviour of the plume, we show in table 5.1 the radius of the streamtube containing 95% of the ion current at $z = z_L$. This measures the radial expansion of the plume and is seen to increase by almost 15% in the simulations with the highest background pressure.

To further appreciate the effect of collisionality in the expansion we show, in figure 5.4the electric potential evaluated in two circular arcs at distances $6R_0$ and $10R_0$ from the centre of the throat, these arcs are the ones depicted in red in figure 5.3 (a). Radially, all the simulation cases exhibit a potential drop towards the side of the main plume and a sudden increase in the external part which is similar to structures observed in several experiments [125, 126]. Specifically, Little and Choueiri [80] argued that this structure is generated by ions with sufficient radial velocity overshooting the plasma-vacuum interface unlike the strongly magnetised electrons leading to a positive space-charge build-up and that finite electron Larmor radius effects (FELR) reduce the onset of this potential wall. In our case, this happens due to the ions coming from the side of the throat reaching the peripheral region leading to a spuriously high plasma density there. We also observe that increasing the presence of neutrals both through an increase in p_b and a decreased η_u reduces the lateral potential drop. This decrease is more apparent in simulations $B3$ and UB than in $U3$ as in this last case neutral density decreases very rapidly away from the source and therefore collisional effects are only relevant in the surroundings of the throat. For this same reason, simulations $B3$ and UB show very similar profiles, the strong rarefaction of the neutrals coming from the source makes background

neutrals dominant in simulation UB.

As expected from the setup of the different simulations, neutrals behave very differently in each of the scenarios. Figure 5.5 (a) shows the on-axis neutral density normalized with its maximum value. Simulations $B3$, $U3$ and UB show, respectively, an essentially constant neutral background, the expansion of injected neutrals and the injected neutral density decreasing until the background density dominates.

On the other hand, plasma density in figure 5.5 (b) is seen to follow the same trend in all simulations, this agrees well with [116]; as ϕ is uniquely determined by the ratio n_e/n_{e0} in equation (5.12) this implies the potential fall is very similar in all cases. Ion velocity is seen to increase to roughly seven times its initial value as potential energy is converted into ion kinetic energy, however, CEX collisions tend to slow down the ion fluid, for this reason, velocity profiles are seen to follow a trend similar to the radial potential in figure 5.4, this is, we see almost matching tendencies for simulations R and $U3$ and for simulations $B3$ and UB respectively, with the last two showing a 6% decrease in ion velocity with respect to the reference one, this does not imply a loss of momentum in the plasma as the loss of ion momentum via CEX leads to an equal gain of momentum by the neutral fluid. In table 5.1 we clearly observe that terminal velocity decreases monotonically with increasing p_b and decreasing η_u. This loss in ion velocity is noticeably smaller than the one reported in [52] which is of the order of $\sim 20\%$ for similar background pressures. PIC simulations[116] also observe a higher velocity loss of $\sim 22\%$ albeit using a higher background pressure of 10 mPa, higher power input and electron temperature. As a matter of fact extrapolating our data to the pressures used in the aforementioned study yields a decrease of 14% in final ion velocity. This is mainly due to the transfer of ion momentum to the neutral fluid via CEX collisions and to a minor extent due the addition of slow ions by virtue of ionization collisions. This gain in ion mass due to late ionization in the plume is given by

$$\frac{\dot{m}_i}{\dot{m}_{i0}} = 1 + \frac{1}{\dot{m}_{i0}} \int_\Omega S_{ion} m_i d\Omega, \tag{5.21}$$

where $\dot{m}_i$ is the integral of the ion flux leaving the domain and $\dot{m}_{i0}$ is the ion mass flow entering the domain at the throat given. This gain in ion mass flow is observed to be up to 12% of the initial mass in the scenarios with the highest background density, here Ω represents the whole domain.

Finally, in figure 5.5 (d), we plot the temperature of the ion fluid. Clearly ions remain cold in all cases in comparison to the electron fluid, the highest ion temperature is reached in simulation $B3$ with $T_{i,max} = 0.67$ eV compared to an electron temperature of 4 eV in that region. This ion temperature are comparable tot hose observed by [48]. Neutral temperature, on the other hand, is lower than 1100 K in all the simulated scenarios.

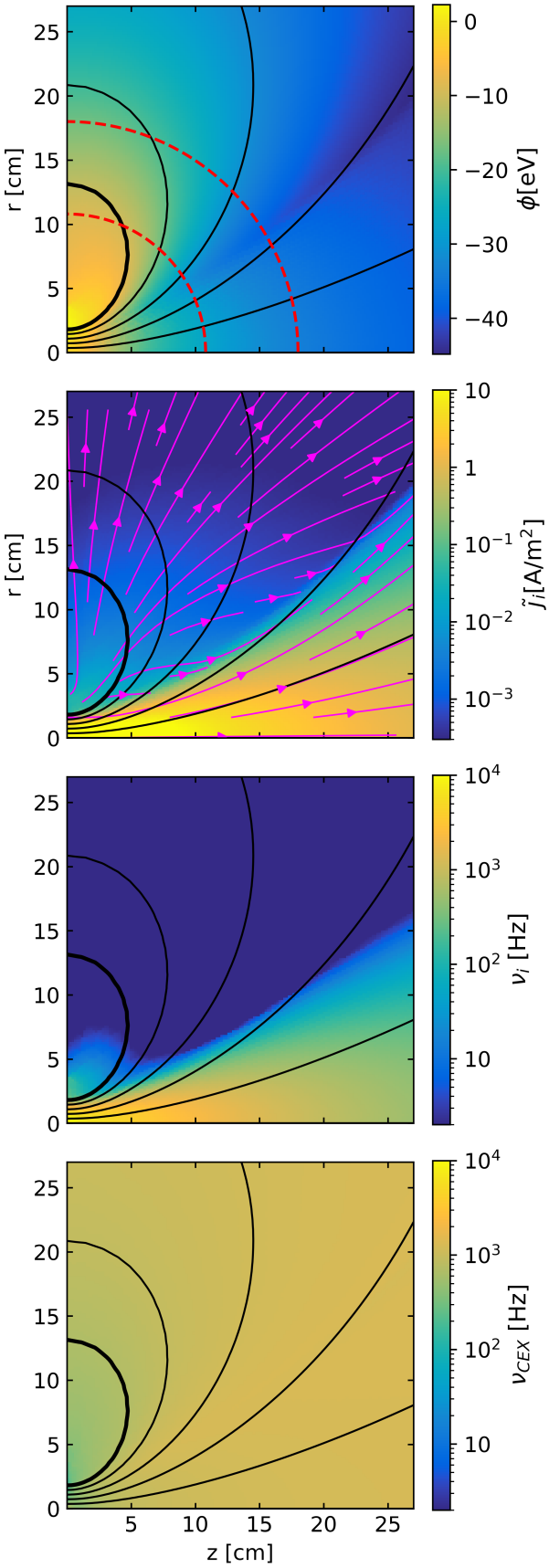

Figure 5.3: Map of electric potential ϕ, ion current in the meridian plane and ionization and CEX collision frequencies for the UB simulation. Magenta lines depict the streamlines of ion current.

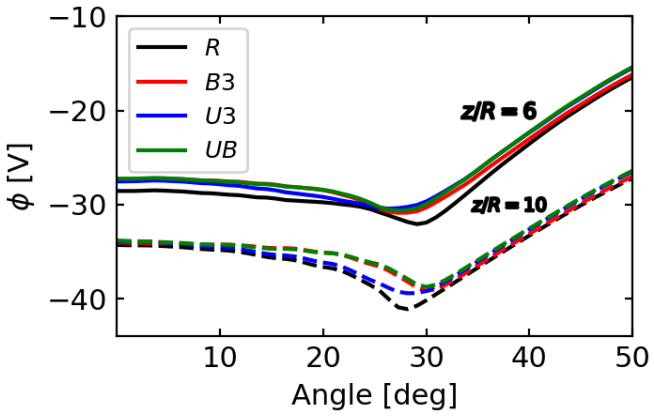

Figure 5.4: Electric potential measured in the arches depicted in figure 5.1 for simulations *R*, *U3*, *B3* y *UB*.

5.3.4 Role of collisions on the electron fluid

The collisionless electron model has allowed us to find an algebraic electron solution as in [20]. We next revisit this assumption discuss the effect of collisions on the geometry of electron streamlines, on the stream-wise conservation of H_e, and on the the electron heat flux at the throat,.

In order to evaluate the validity of our approach with the electron solution we come back to equations (5.14) and (5.15). We recall that the collisionless model yields $u_{\theta e}$ according to equation (5.16), and $u_{\perp e} = 0$. The inclusion of weak collisions adds a correction to this solution, scaling with the inverse Hall parameter χ^{-1} as:

$$\Delta u_{\perp e} = \chi^{-1} u_{\theta e} \sim \frac{m_e \nu_e T_{e0}}{e^2 B_0^2 R_0}, \tag{5.22}$$

$$\Delta u_{\theta e} = -\chi^{-2} u_{\theta e} \sim \frac{m_e^2 \nu_e^2 T_{e0}}{e^3 B_0^3 R_0}, \tag{5.23}$$

where $u_{\theta e}$ on the right hand sides is the one corresponding to the collisionless solution. For reference, figure 5.6 displays the map of χ^{-1} in the *UB* simulation. This parameter remains small everywhere, even in this low-utilization and relatively-large background pressure case. Equation (5.22) states that electron collisionality induces a first order correction $\Delta u_{\perp e}$ that points radially outward, i.e., it works toward increasing the plume divergence angle [46]. The correction $\Delta u_{\theta e}$ is only second order, and implies a negligible decrease of $u_{\theta e}$ in the range of interest.

We shall therefore only discuss the effect that $\Delta u_{\perp e}$ has on the expansion and the divergence of the plume this was already partially assessed. Indeed, this effect depends on the tangent ratio $\Delta u_{\perp e}/u_{\parallel e}$, which can be assessed using the $u_{\parallel e}$ solution of the collisionless model. Here we remind the reader that $u_{\parallel e}$ depends largely on the boundary conditions used to solve the electron continuity equation (5.9) [20]. To illustrate this, we consider two distinct boundary conditions of interest with the

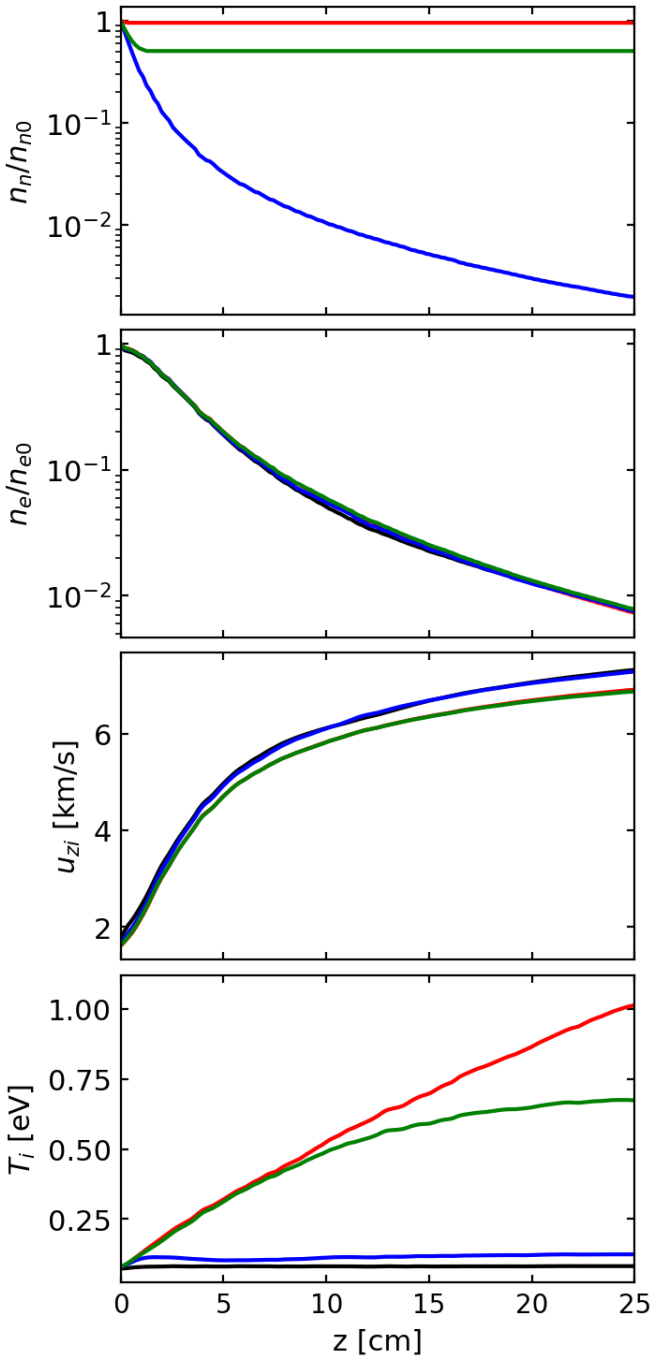

Figure 5.5: On axis values for neutral density, ion density, ion velocity and ion temperature. Colour code is the same as in figure 5.4.

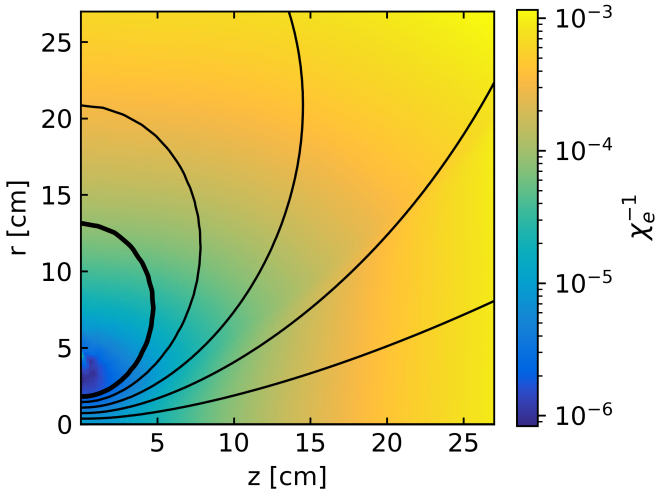

Figure 5.6: Inverse of electron Hall parameter for simulation *UB* withp_b = 4 mPa and $\eta_u = 0.5$ and a maximum magnetic field of 200 G in the center of the nozzle throat.

simulation *UB*: (1) local current ambipolarity (LCA) conditions imposed at the MN throat, representative of the operation of a short plasma source firing in space, and (2) LCA imposed at the downstream and lateral boundaries, representative of a device operating in a vacuum chamber with dielectric walls (or of a plasma source with MN used for material processing applications) [20]. Since LCA is not satisfied in the bulk of the plasma plume (because ions separate inward from the magnetic lines while electrons remain magnetized), these two conditions result in rather different maps of $u_{\parallel e}$: conditions (1) lead to a relatively large $u_{\parallel e}$ in the plume periphery, whereas conditions (2) concentrate a larger $u_{\parallel e}$ in the core of the exhaust.

Consequently, the tangent $\Delta u_{\perp e}/u_{\parallel e}$ remains rather small in the whole simulation domain in case (1), while a noticeable tangent develops in the plume periphery (where plasma density is nevertheless small) in case (2). This is an indication that a MN operating in free space and in a vacuum chamber can differ in the resulting plasma divergence angle, especially if the vacuum chamber wall material imposes the local current ambipolarity downstream. These two cases are depicted in the first row of figure 5.7 which shows the in-plane electron current $\tilde{j}_e = -en_e\tilde{u}_e$; the resulting total plasma currents, $\tilde{j} = \tilde{j}_e + \tilde{j}_i$ are shown in the second row. It can be noted that the magnitude of $\tilde{j}_e$ (and, accordingly, $\tilde{j}$) is large in the periphery of case (1), as dictated by the boundary conditions at the throat; as the plasma density in this regions is low, this translates into a few electrons having a large $u_{\parallel e}$ in this region [20]. In contrast, $\tilde{j}_e$ and $u_{\parallel e}$ are negligible in the periphery in case (2). The geometry of the $\tilde{j}$ lines in case (2) is the consequence of the rectangular shape of the domain, as the boundary conditions demand that these lines be tangent to the downstream and lateral edges (indeed, the change of behaviour across the magnetic lines that connect to the corners of the domain, in white, is noticeable).

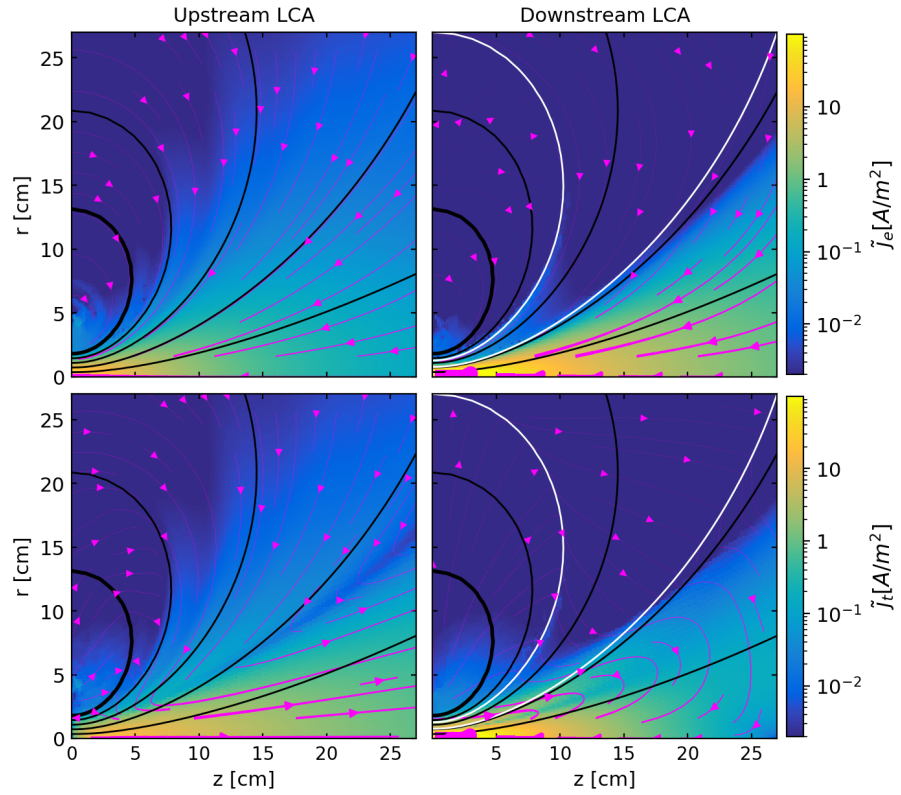

Figure 5.7: In-plane electron and total currents in simulation UB with ambipolarity imposed at the throat (left column) and ambipolarity imposed in the outflow boundaries (right column). In the right column white lines depict magnetic lines crossing the vertices of the domain.

With regards to the validity of using the collisionless electron solution to determine the electron properties and the electrostatic potential map ϕ, we conclude that boundary conditions of type (1) are better suited for this type of approximation, while the accurate solution of plasma expansions under type (2) conditions likely requires either to include this correction iteratively into the electron maps, or a complete, collisional electron model. Type (1) conditions better approximate those of a plasma plume expanding into space, although we clarify that the boundary conditions to be imposed in that case do not necessarily need to enforce LCA at the throat: the only strong requirement is that of *global* current ambipolarity (GCA), i.e., that the *integral* at the exit section of $\tilde{j}$ vanish. We also conclude that the effect of collisions is expected to lead to a larger plume divergence increase in situations better described by conditions (2).

Analyzing the scaling of equations (5.22) and (5.23) we observe that the relevant ratios for both collisional corrections $\Delta u_{\perp e}/u_{\parallel e} \propto \chi_e^{-1} B_0^{-1}$ and $\Delta u_{\theta e}/u_{\theta e} \propto \chi_e^{-2}$ scale with the squared inverse of B_0; observing that the maximum value of χ_e^{-1} is around 10^{-3} we conclude that a reduction of one order of magnitude in B_0 would make the perpendicular drift of the electrons comparable to their parallel velocity. This would imply $B_0 \sim 20$ G which is, in fact, a low magnetic field for the typical operation

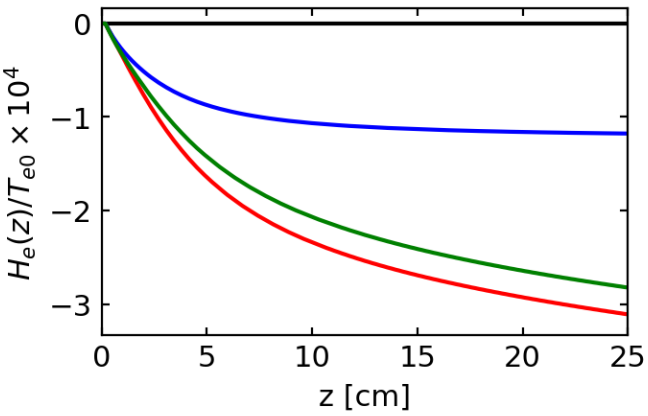

Figure 5.8: Axial value of H_e accounting for collisions in simulation UB with ambipolarity imposed in the downstream boundary. Colour code is the same as in figure 5.4.

conditions in EPTs, however the accumulated effect of the deflection of electron streamlines could appear at higher magnetic fields. Even lower values of B_0 would be necessary to affect the azimuthal velocity of electrons noticeably.

The second effect of collisions on the electron model stems from the parallel dynamics, as shown in equation (5.13): when parallel collisionality is included, H_e is not conserved along magnetic streamlines anymore, and moreover, $u_{\parallel e}$ becomes weakly coupled with the rest of the problem. The decrease of H_e along magnetic lines has the double effect of modifying $u_{\theta e}$, which depends on the perpendicular gradient of H_e, and reducing the total potential fall across the nozzle. These effects, however, are very minor in the simulation cases explored, as can be inferred from figure 5.8 which presents the variation of H_e along the axis of the MN (with LCA imposed downstream, which gives a larger decrease). The small effects of collisions on H_e are more prominent when background pressure is included, as a matter of fact one can observe that there is a faster decrease near the throat which does not plateau in the simulation domain when background density is included. The smallness of variation validates the modelling approach followed in this work for electrons.

Finally, another assumption of the electron model is that of negligible inertia (which are first-order finite Larmor radius effects). Given that $u_{\theta e}$ can be large and that for boundary conditions of type (1) the parallel electron velocity $u_{\parallel e}$ can become large in the periphery, it is reasonable to question the validity of this assumption. To gauge the influence of finite electron inertia, we proceed similarly to [127] and compute the following normalized electron inertia term from our zeroth-order solution:

$$\epsilon_{iner} = \frac{|\nabla(m_e n_e \boldsymbol{u}_e \boldsymbol{u}_e)|}{|\nabla p_e|}.$$

This compares locally the effect of electron inertia against the electron pressure force. This term is shown in figure 5.9 for simulation UB and for both electron boundary

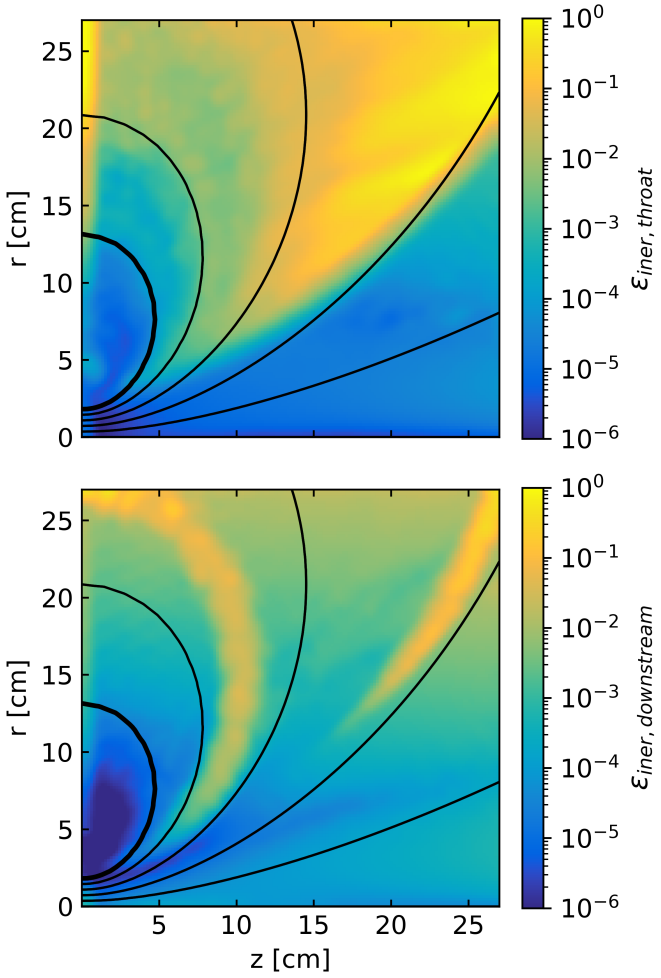

Figure 5.9: Absolute value of inertial terms of electron momentum equation.

conditions. In the case with LCA imposed at the throat, ε_{iner} is only greater than 10^{-3} in the periphery of the plume, where the plasma is very tenuous and electron pressure negligible. As the plasma density is very low in this region, this error has a presumably small effect on the computed results. In the case in which LCA is imposed in the downstream boundary, ϵ_{iner} is seen to reach values of the order of $10^{-3} - 10^{-2}$ already in downstream region of the main plume, indicating that, while still negligible, will affect the plasma expansion in the main jet earlier than in the upstream LCA case. In passing, we note that in order to make a comprehensive discussion of FLRE one would need to asses the effect of the so called gyroviscous force which is simply the divergence of the off-diagonal terms of the pressure tensor in a magnetized plasma also referred to as the gyroviscous tensor. A full study of this effects is not performed here as the complexity of these terms deserves a detailed study [128].

5.3.5 Effect of collisions on the electron power balance

The total power flowing into the MN P_{in} is the sum of the convective power carried by each of the species and the electron heat-flux at the throat,

$$P_{in} = P_{conv} + Q_{e0}, \tag{5.24}$$

where the convective power is:

$$\begin{aligned} P_{conv} = &\int_{S_0} \frac{5}{2} n_{e0} T_{e0} u_{zi0} \mathrm{d}S \\ &\int_{S_0} \left[\frac{m_i}{2} n_{e0} u_{zi0}^3 + \frac{5}{2} n_{e0} T_{i0} u_{zi0} \right] \mathrm{d}S \\ &\int_{S_0} \left[\frac{m_i}{2} n_{n0} u_{zn0}^3 + \frac{5}{2} n_{n0} T_{n0} u_{zn0} \right] \mathrm{d}S \end{aligned} \tag{5.25}$$

Note that the contributions due to the ion and neutral temperature, and due to neutral kinetic energy, are typically negligible.

From the viewpoint of electron thermodynamics, it is noteworthy that the chosen polytropic electron cooling model implies the existence of a nonzero heat flux Q_e into the plume that maintains that electron temperature profile in the plume, which is greater than in the adiabatic limit and can be calculated from the total balance of power in the plume [92], this heat flux corresponds to the first term in equation (5.26). In this study we are assuming that the the polytropic index and electron temperature at the throat are kept constant in all of the simulated scenarios. However, the existence of inelastic collisions in the plume removes energy from the electron population. The balance of power demands that the value of the electron heat flux at the MN entrance increases with respect to the collisionless case, to maintain the same γ_e and T_{e0},

$$Q_{e0} = \frac{3}{2} T_{e0} \eta_u \frac{\dot{m}}{m_i} \left(\frac{5/3 - \gamma_e}{\gamma_e - 1} \right) + P_{coll} \tag{5.26}$$

where the energy lost to inelastic collisions in the plume can be calculated as:

$$P_{coll} = \int_{\Omega} S_{ion} E_{inel} \mathrm{d}\Omega. \tag{5.27}$$

This power loss of the electron fluid is gauged a posteriori in our work and is, in the highest loss scenario, up to 31% of the inlet energy flux. Alternatively, using equation (5.26) , defining $\tilde{Q}_{e0} = Q_{e0} - P_{coll}$ and assuming the input power had been kept constant, power balance would require:

$$\tilde{Q}_{e0} = \frac{3}{2} T_{e0} \eta_u \frac{\dot{m}}{m_i} \left(\frac{5/3 - \tilde{\gamma}_e}{\tilde{\gamma}_e - 1} \right)$$

and thus we can find the effective polytropic cooling exponent of the expansion:

$$\tilde{\gamma}_e = \frac{5 + \dfrac{2m_i\tilde{Q}_{e0}}{T_{e0}\eta_u\dot{m}}}{3 + \dfrac{2m_i\tilde{Q}_{e0}}{T_{e0}\eta_u\dot{m}}}, \tag{5.28}$$

which is reported in table 5.1. This computation allows us to assess what is the expected change in the polytropic index as the importance of collisions in the plume varies; we note that $\tilde{\gamma}_e$ increases slightly with η_{u0} and p_b, indicating that, while minor — values in all the investigated scenarios are in the range of those reported in the literature [120]— collisions displace this parameter away in the direction of the adiabatic limit $\tilde{\gamma}_e = 5/3$.

With this variation in mind, we can now assert what would be the effects of inelastic collisions, if we had fixed P_{in} rather than T_{e0} in our simulations.

As P_{coll}/P_{in} increases, the initial electron temperature T_{e0} would need to decrease to maintain the power balance. Additionally, the larger polytropic index $\tilde{\gamma}_e$ would lead to a faster drop of the electron temperature downstream and a reduced potential drop to infinity, which is

$$\Delta\phi = -\frac{\tilde{\gamma}_e}{\tilde{\gamma}_e - 1}\frac{T_{e0}}{e}, \tag{5.29}$$

thus reducing the capability of the nozzle to accelerate the ions, and ultimately, thrust. As a matter of fact, for simulation UB this would imply $e\Delta\phi/T_{e0} \simeq -5$ in comparison to a value of $\simeq -6$ in simulation R. In our T_{e0}-constant simulations, this effect inelastic energy losses on thrust is not present, as P_{coll} is simply compensated by the larger P_{in} to keep the electron temperature at the entrance constrained. Nevertheless, the relevance of this balance is evident in the efficiency figures computed in section 5.3.6.

5.3.6 Propulsive performance

The sum of the steady-state momentum conservation equation for each species(5.10), (5.3) and (5.6) leads to an equation for the conservation of total momentum in the nozzle:

$$\nabla \cdot (n_e \boldsymbol{u}_i \boldsymbol{u}_i + n_n \boldsymbol{u}_n \boldsymbol{u}_n + p) = n_e(\boldsymbol{u}_i - \boldsymbol{u}_e) \times \boldsymbol{B},$$

where $p = p_e + p_i + p_n$ is the total pressure in the plasma. The integral of the axial component of this equation renders the total thrust produced by the nozzle up to

the end of the domain:

$$\begin{aligned} F &= F(0) + F_{mag} \\ &= \int_{S_0} (m_i n_e u_{zi}^2 + m_i n_n u_{zn}^2 + p_e + p_i + p_n) \mathrm{d}S \\ &+ \int_{\Omega} (-j_\theta B_r) \mathrm{d}\Omega, \end{aligned} \tag{5.30}$$

This is, thrust can be seen to be the sum of two contributions, the internal thrust produced in the source and equal to $F(0)$ and the external thrust produced by the magnetic force that the plasma exerts on the coils of the thruster. Both of this contributions can be further decomposed in the different species. The share of the external thrust for each species is given by:

$$\begin{aligned} \Delta F_i = \int_{\Omega} (&-e n_e \mathbf{1}_z \cdot \nabla \phi + j_{\theta i} B_r \\ &+ S_{ion} m_i \boldsymbol{u}_n + S_{CEX} m_i (\boldsymbol{u}_n - \boldsymbol{u}_i)) \mathrm{d}\Omega \end{aligned} \tag{5.31}$$

$$\Delta F_e = \int_{\Omega} (e n_e \mathbf{1}_z \cdot \nabla \phi + j_{\theta e} B_r - m_e n_e \nu_e \boldsymbol{u}_e) \mathrm{d}\Omega \tag{5.32}$$

$$\Delta F_n = \int_{\Omega} (-S_{ion} m_i \boldsymbol{u}_n - S_{CEX} m_i (\boldsymbol{u}_n - \boldsymbol{u}_i)) \mathrm{d}\Omega \tag{5.33}$$

These contributions can be found in table 5.1. We observe that, due to the subsonic velocity of the ions at the throat, the internal thrust is mostly delivered by the electron pressure with the neutral contribution being one order of magnitude smaller even in the lowest utilization scenario. The working principle of the magnetic nozzle observed in [20] holds in all the simulation cases: the flux of electron momentum decreases during the expansion due to their loss of thermal energy which, in turn, is converted into ion kinetic energy via the ambipolar electric field. For lower values of η_{u0}, both ΔF_e and ΔF_i are seen to decrease in magnitude due to the reduction in available energy in the form of electron pressure. Increasing p_b on the other hand, results in an augmented effective mass flow rate of ions and electrons due to ionization, which leads to an increase in their momentum, even if ion velocity is reduced. Neutral momentum gain is always small compared to the electron and ion one being essentially unaffected by η_{u0}; however, when background pressure is increased, the transfer of momentum to neutrals via CEX is evidenced. Indeed, CEX collisions do not directly incur in a loss of thrust as suggested in [116], since they merely transfer momentum from the ions to the neutrals. CEX collisions cause the entrainment of neutrals by the ions, and has the same effect as an increase in the total mass flow (total thrust increases, while ion velocity decreases).

We remark that our results predict the increase of thrust evaluated at the end of the domain $F(z_L)$ with increasing p_b. We find that this increase is contingent on keeping T_{e0} constant in our parametric analysis. As indicated in section 5.3.4, as η_{u0} is decreased and as p_b is increased, this requires increasing the power input to the

device. Keeping P_{in} constant instead would result in a different behaviour of $F(z_L)$. This may explain why finding experimental trends with p_b is a delicate matter, as they may depend on the detailed power balance of each setup. Indeed, thrust increase with p_b is reported in Hall thrusters as a steady discharge voltage can be maintained during operation [129], while the contrary is found in EPTs [114, 52, 26].

A more robust performance figure that is not affected by what is constrained to be constant in the analysis is the MN efficiency, defined as

$$\eta_{MN} = \frac{F^2}{2\dot{m}_0 P_{in}}. \tag{5.34}$$

Crucially, η_{MN} decreases in all simulations with the introduction of neutrals from any source, either due to an incomplete utilization at the entrance, or due to background pressure. In order to analyze the different mechanisms of performance loss in the nozzle we expand this efficiency as

$$\begin{aligned} \eta_{MN} &= \frac{\dot{m}_{i0}}{\dot{m}_0}\frac{P^*_{in}}{P_{in}}\frac{F^2}{F_i^2}\frac{{F_i}^2}{2\dot{m}_{i0}P^*_{in}} \\ &= \eta_{u0}\kappa_P\kappa_F\kappa_{MN}, \end{aligned} \tag{5.35}$$

where thrust forces are evaluated at z_L, and $P^*_{in} = P_{in} - P_{coll}$ is the inlet power disregarding collisional losses. In the factorization shown in 5.35 κ_F is the fraction of the force carried by the ion fluid while κ_{MN} incorporates several aspects of the ion acceleration such as the divergence and the dispersion efficiencies.

This factorization lets us identify two different trends. In the first ones, the reduction in efficiency is produced by the drop in η_u. This is, even if the ions expelled by the source are accelerated efficiently (κ_{MN} increases while κ_P and κ_F stay reasonably unchanged) these ions are not accelerated efficiently enough to compensate for the loss of ionization in the source. On the other hand, in the simulations with increasing p_b, κ_F is seen to grow when raising chamber pressure, this is, the ions the fraction of the force exerted by the ions is seen to decrease as the neutrals are entrained by CEX collisions; moreover, κ_{MN} is seen to increase due to the increased mass flow of plasma which is strongly related to the enhanced utilization efficiency given by (5.21). This effect might be responsible for the rise in performance in Hall effect thrusters [31] in poor vacuum conditions, however, in MNs the power needed to sustain the discharge grows quickly with background pressure and therefore the term κ_P decreases hindering the efficiency of the nozzle [114, 52].

Therefore, the decrease of efficiency can be attributed to inelastic collisions increasing severely the power needed to sustain discharge while the increase in magnetic thrust due to collisions does not increase enough to compensate this effect.

5.3.7 Ion distribution Functions

Some helicon thruster experiments with non-negligible background pressure show that the ion velocity distribution function (IVDF) is double-peaked [130, 52, 131]. The main peak is produced by the primary or beam ions expelled directly by the source, while a lower energy peak appears due to late ionization in the plume and other collisional effects in the plume region, which depend on the chamber pressure an the initial utilization efficiency. In some cases and depending on the position in the plume, the slow ions may become predominant [52].

Here, we present a method to estimate the IVDF of the ions that underwent collisional processes in the nozzle. This method is, of course, not self-consistent as the distribution function is a fully kinetic feature that can only be resolved with kinetic models. It is, however, an interesting addition to our analysis with a computationally cheaper fluid model.

We limit our discussion to the axis ($r = 0$). The rate at which slow ions are produced due to ionization and charge-exchange collisions is given by $S(z) = S_{ion}(z,0) + S_{cex}(z,0)$, per unit volume and unit time. Slow ions created at a position z reach a downstream measurement point z_m with a velocity v given by $v^2 = 2e[\phi(z) - e\phi(z_m)]/m_i$. This expression sets a univocal relation between v and z, and differentiating we find $v\mathrm{d}v = e\phi'(z)\mathrm{d}z/m_i$. Then, the flux of ions $g_i(v)$ at the measurement point satisfies the 1D continuity equation

$$g_i(v)\mathrm{d}v\mathrm{d}A_m = S(z)\mathrm{d}z\mathrm{d}A, \tag{5.36}$$

where $\mathrm{d}A$ is the area of an infinitesimal streamtube, and $\mathrm{d}A_m$ its corresponding area at z_m. Assuming for simplicity that the generated slow ions accelerate downstream and expand like the corresponding magnetic tube, $\mathrm{d}A_m/\mathrm{d}A = B(z_m)/B(z)$, and using the relation between $\mathrm{d}v$ and $\mathrm{d}z$ through ϕ',

$$g_i(v) = \frac{B(z_m)}{B(z)}\frac{m_i v S(z)}{e\phi'(z)}. \tag{5.37}$$

This is the slow ion flux distribution function that a device like a retarding potential analyzer can measure in the plume of a MN. The corresponding density distribution function at point z_m is then:

$$f_i(v) = \frac{B(z_m)}{B(z)}\frac{m_i S(z)}{e\phi'(z)} \tag{5.38}$$

Figure 5.10 shows the distribution functions for ions obtained as described above for the simulations with varying background pressure, along with the VDF of a drifting Maxwellian with total density and velocity equal to that of the ions at $z_m = z_L$ and temperature equal to their initial temperature. We observe that, in simulation $B3$, the maximum in the distribution of slow ions is one order of magnitude smaller than that of fast ions.

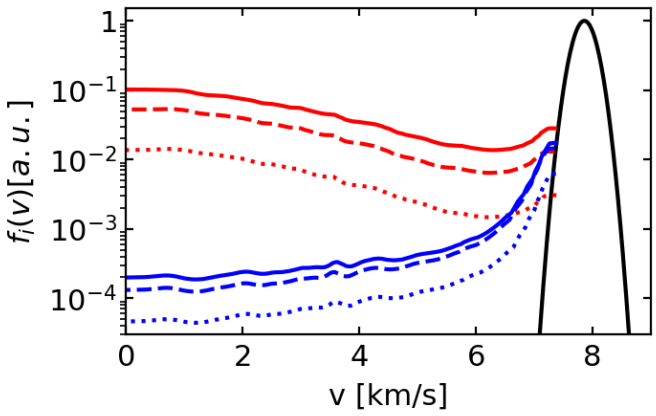

Figure 5.10: Recovered distribution functions at $z = z_L$. Simulations $B1$, $B2$ and $B3$ are represented by red dotted, dashed and solid lines respectively while the blue dotted, dashed and solid lines show simulations $U1$, $U2$ and $U3$, respectively. The black line represents the VDF of a drifting Maxwellian corresponding to the injected ions in simulation R.

All simulations with collisions show that f_i increases near the beam velocity. These ions are created by the high collisionality around the nozzle throat where plasma density is highest and are, in fact, responsible for the slight warming of the ion fluid observed in simulation $U3$ (see figure 5.5). This increase is the only remarkable feature in simulations $U1$-$U3$ without background pressure: the net effect of collisionality in these cases is to skew the IVDF of the beam toward lower velocities, what is equivalent to having a wide effective ionization region that extends from inside the source to the near plume. However, in simulations with background pressure, the IVDF presents a secondary peak at low velocities. Indeed, these are ions that result from the sustained ionization and charge-exchange collisions throughout the plume, this is observed experimentally in [52].

We note however that, in our estimation of the IVDF at the end of the expansion, slow ion populations are seen to be one order of magnitude less prominent than the fast ions even in the highest background pressure scenario at 4 mPa. This contrasts with the measurements of [52] where, downstream the slow ions are comparable to the fast ion beam coming from the source even with background pressures of 1.73 mPa. This difference can be attributed to the paraxial expansion we have assumed for the slow ion population, with $\mathrm{d}A_m/\mathrm{d}A = B(z_m)/B(z)$.

5.A Collision models

The simplified collision model employed in this work includes ionization, excitation, ion-neutral charge exchange, electron-ion and electron-neutral. In the following we describe the models used for the cross section of the different collisions included in

this work on each species. Following [132] we take the ionization source term to be:

$$S_{ion} = n_e \nu_{ion} = n_e n_n \tilde{c}_e \sigma_{ion} \tag{5.39}$$

with $\tilde{c}_e = \sqrt{8T_e/\pi m_e}$ and cross section

$$\sigma_{ion} = \sigma_{ion0}(1 + \frac{T_e E_i}{(T_e + E_i)^2}) \exp(\frac{-E_i}{T_e}), \tag{5.40}$$

where E_i is the first ionization energy for xenon (12.1 eV) and $\sigma_{ion0} = 5 \times 10^{-20}\mathrm{m}^2$.

On the other hand, the source term arising from charge exchange collisions reads [133]:

$$S_{CEX} = n\nu_{CEX} = n n_n c_{in} \sigma_{CEX}, \tag{5.41}$$

with $c_{in} = |\boldsymbol{u}_i - \boldsymbol{u}_n|$ and the collision cross-section given by:

$$\sigma_{CEX} = \sigma_{CEX0}\left(1 - 0.2 \log_{10} \frac{c_{in}}{1\mathrm{km/s}}\right), \tag{5.42}$$

where $\sigma_{CEX,0} = 81 \times 10^{-20}\mathrm{m}^2$.

We gauge the effect of collisionality in the electron momentum a posteriori. To this end, elastic electron-ion and electron-neutral collisions as well as ionization, and excitation collisions could be included in the electron momentum equation. However, the collisional rates of excitation and ionization are observed to be at least one order of magnitude smaller than those of elastic collisions [108] and therefore we take:

$$\nu_e \simeq \nu_{en} + \nu_{ei} \tag{5.43}$$

These collision frequencies are taken from [132] and [134] respectively:

$$\nu_{en} = n_n c_e \sigma_{en} \text{ with } \sigma_{en} = 27 \times 10^{-20}\ \mathrm{m}^2, \tag{5.44}$$

$$\nu_{ei} = n_e R_{ei}, \text{ with } \frac{R_{ei}}{10^{-12}\mathrm{m}^3\mathrm{s}^{-1}} = \left(\frac{2\mathrm{eV}}{T_e}\right)^{3/2} \ln\Lambda, \tag{5.45}$$

$$\log\Lambda \sim 9 + \frac{1}{2}\log[\left(\frac{10^{18}\mathrm{m}^3}{n_e}\right)\left(\frac{T_e}{1\mathrm{eV}}\right)]. \tag{5.46}$$

Finally, the effective electron energy loss due to inelastic collisions —ionization and excitation— is grouped together and taken to be:

$$E_{inel} = E_i\left[2 + \frac{1}{4}\exp\left(\frac{2E_i}{3T_e}\right)\right]. \tag{5.47}$$

5.B Full model equations

The ion and neutral equations to be solved by the model are the following:

$$\partial_t n_e + \nabla \cdot (n_e \boldsymbol{u}_i) = S_{ion}, \tag{5.48}$$

$$\partial_t n_e \boldsymbol{u}_i + \nabla \cdot (n_e \boldsymbol{u}_i \boldsymbol{u}_i + \frac{1}{m_i} n_e (T_i + T_e)) = \frac{e n_e}{m_i} (\boldsymbol{u}_i - \boldsymbol{u}_e) \times \boldsymbol{B} + S_{ion} \boldsymbol{u}_n + S_{CEX} (\boldsymbol{u}_n - \boldsymbol{u}_i) \tag{5.49}$$

$$\partial_t \left(\frac{3}{2} n_e T_i \right) + \nabla \cdot \left(\frac{5}{2} n_e T_i \boldsymbol{u}_i \right) = \boldsymbol{u}_i \cdot \nabla n_e T_i$$
$$+ S_{ion} \left(\frac{3}{2} T_n + \frac{m_i}{2} (\boldsymbol{u}_i - \boldsymbol{u}_n)^2 \right) + S_{CEX} \left[\frac{3}{2} (T_n - T_i) + \frac{m_i}{2} (\boldsymbol{u}_i - \boldsymbol{u}_n)^2 \right] \tag{5.50}$$

$$\partial_t n_n + \nabla \cdot (n_n \boldsymbol{u}_n) = -S_{ion}, \tag{5.51}$$

$$\partial_t n_n \boldsymbol{u}_n + \nabla \cdot (n_n \boldsymbol{u}_n \boldsymbol{u}_n + \frac{1}{m_i} n_n T_n) = -S_{ion} \boldsymbol{u}_n + S_{CEX} (\boldsymbol{u}_i - \boldsymbol{u}_n) \tag{5.52}$$

$$\partial_t \left(\frac{3}{2} n_n T_n \right) + \nabla \cdot \left(\frac{5}{2} n_n T_n \boldsymbol{u}_n \right) = \boldsymbol{u}_n \cdot \nabla n_n T_n$$
$$- S_{ion} \frac{3}{2} T_n + S_{CEX} \left[\frac{3}{2} (T_i - T_n) + \frac{m_i}{2} (\boldsymbol{u}_i - \boldsymbol{u}_n)^2 \right] \tag{5.53}$$

Note that the electron azimuthal velocity appearing in (5.49) is obtained from the azimuthal electron momentum equation in the collisionless limit (5.16).

5.C Cell size, order and domain convergence

Discontinuous Galerkin methods are, by construction, locally conservative for systems of hyperbolic equations [39]. However, as explained previously, we have introduced some minor, yet non-conservative terms in the discretization of the energy equation for both ions and neutrals 5.2.3. In this regard, our integration method departs from the typical DG methods and therefore we find necessary to check the effect of h (cell size) and p (polynomial order) refinement in our solution. To this end we run simulation UB in a smaller 5×3 (in units of R_0) domain with three different cell sizes and for polynomial orders 0 and 1. We then run a fifth simulation with an even finer cell size and order 1 elements, and take that solution as exact. In table 5.2 we show the global L_2 error of the different simulations. We observe a convergence rate of 1.6 for the order zero discretization and 2.2 for the order one discretization; the expected asymptotic convergence rate for DG methods is $\mathcal{O}(h^{p+1})$.

Furthermore, we test the possible effect of a domain size change by running simulation UB on a $10R_0 \times 10R_0$ domain with equal cell sizes as the original. Table 5.3 shows the final velocity and electric potential for the two domain sizes evaluated in the axis at $z = 10R_0$. The change among them is around 2% for the electric

Polynomial degree	Cell size	L_2 error	Convergence rate
0	0.2	0.0041	1.6
	0.15	0.0025	
	0.1	0.0014	
1	0.2	0.0025	2.2
	0.15	0.0013	
	0.1	0.00053	

Table 5.2: Summary of convergence results for cell size and polynomial degree.

	Domain size		Percentage change
	10×10	15×15	
$e\phi/T_{e0}(z = 10R_0)$	-3.48	-3.42	1.7 %
$u_{zi}/c_{s0}(z = 10R_0)$	2.422	2.430	0.32%

Table 5.3: Effect of domain size on main plasma variables.

potential and 0.3% for the final velocity, so we consider the domain size to play a small effect on the solutions discussed in the main text.

5.4 Summary

A two-dimensional, three-fluid model based on discontinuous Galerkin finite elements has been used to simulate the effects of non-ideal propellant utilization at the source η_{u0} and background pressure p_n on the plasma expansion in a MN. Ion expansion is seen to change little in the range explored; the main effect of collisions with neutrals are a mild decrease in final ion velocity and a small increase of divergence angle. Ions are seen to develop some temperature due to collisions with neutrals, up to ~ 1 eV in one of the simulation cases; an estimation of the resulting ion velocity distribution function has revealed the formation of a low-energy ion population, with distinct characteristics when varying η_{u0} or p_b. These effects are consistent with experimental observations [52] and are more marked in those cases that feature a background pressure, compared to those with an imperfect utilization efficiency. Indeed, in simulation UB, the role of background neutrals outweighs that of the neutrals coming from the source, whose effect is essentially restricted to the near plume.

One should analyze the effect of ion-neutral collisions according to their type (ionization, CEX) and the origin of the intervening neutrals (imperfect utilization, background density). The effect of near plume ionization of neutrals escaping from the source can be assimilated to a late increase in utilization efficiency. However, ions

generated outside of the source do not see the full potential drop, and are therefore less accelerated by it, lowering the fluid velocity of ions. Analogously, CEX collisions with escaping neutrals transfer momentum from the ion fluid to the neutral fluid, and play a similar role to having an increased ion mass . The momentum of the resulting fast neutrals contributes to thrust, while the resulting slow ion can re-accelerate by the remaining potential drop, and continue to contribute to propulsion. We note, nevertheless, that slow ions in the plume (be they the result of ionization or CEX) are prone to be accelerated radially faster than ions, and thus raise the ion fluid divergence angle. On the other hand, when the new ions from ionization or the fast neutrals from CEX come from the background density, they provide a 'free' additional mass flow rate to the jet, and can affect the conclusions of experimental studies if this effect is not taken into account.

Collisions are seen to affect somewhat the electron-confining potential barrier that exists at the plume edge, lowering its strength. Such barrier, which requires modelling the main and the peripheral plasma to be successfully studied, has been observed experimentally[80]. While our simple electron model only takes into account collisions perturbatively, our analysis has shown that electron streamline divergence is expected to increase due to collisions, albeit only minimally for upstream LCA boundary conditions (the ones that more closely resemble in-space operation). The effect becomes more noticeable at rather low magnetic field strengths and for LCA conditions downstream (representative of a plume expansion limited by a dielectric wall). This last aspect highlights the role another facility effect often disregarded, namely the influence of the vacuum chamber walls and their nature. On the other hand, the main assumption of our model (constant H_e along electron lines) seems robust in the parametric space considered here.

Collisions with neutrals lower the performance of the MN, in terms of their η_{MN} as defined in equation (5.34). This is in spite of the apparent rise of thrust force that originates in the extraordinary plasma generation that occurs in the plume, for a fixed value of the electron temperature upstream, T_{e0}. This increase is counterbalanced by the larger power expenditure incurred into, due to the inelastic collisions (which can also be interpreted as an increase of the polytropic electron coefficient with collisions). This trend allows us to conclude that collisions with neutrals (regardless of their origin) are detrimental for MN operation, and this may have an impact in interpreting existing laboratory experiments, especially when the background pressure is not sufficiently low to allow neglecting its effects.

The present model offers the possibility of "translating" laboratory MN experiments to in-space conditions, effectively discounting (some of) the facility effects. This could be accomplished by, first, fitting the model inputs to reproduce the laboratory measurements under a given background pressure, and then, carrying out the same simulation for an identical plume expanding into vacuum. This promising line of work is left for future research. Likewise, posing a complete electron model that

does not solve electron collision effects perturbatively and explores other closure relations beyond the polytropic assumption (perhaps at the heat flux level) should be a next step in the modelling of MNs.

Chapter 6

Conclusions

To conclude this work we gather here the main results of the thesis. A two-dimensional planar/axisymmetric multi-fluid code, named `POSETS`, has been developed for the simulation of the steady state behaviour of the magnetic nozzle in electron driven Electrodeless Plasma Thrusters. The models included in the `POSETS` code are based on the slow dynamics drift-diffusion approximation for the electron fluid and can be easily extended to include several physical mechanisms that have been proven to be of importance in the characterization of EPTs. This code harnesses the capabilities of the `FEniCS` [69] library in order to build and solve Discontinuous Galerkin (DG) discretizations of the model equations. These methods have become increasingly popular, particularly in the realm of computational fluid dynamics (CFD) thanks to the their local conservation properties, their convenience for the solution of convection-dominated problems, their compact stencil which is limited to the neighbouring elements and the ease in which *hp*-adaptivity is performed. Finally, the DG method is able to handle discretizations over unstructured grids, this property is particularly interesting in the simulation of plasma plumes as different regions exhibit a wide range of gradients and length scales. The code was verified against known fluid dynamics and plasma solutions verifying the effect $h-$ and $p-$ refinement on the error.

Chapter 4 presents the first simulations, to the best of the authors knowledge, of plasma expansion in a magnetic arch configuration. The results demonstrate that a free ion beam can be extracted from the source and expanded into a vacuum. Near the symmetry plane, an oblique shock forms, raising the electric potential and slowing the ion fluid. Plasma expansion initially resembles that of an axisymmetric nozzle, but the interaction of ion streamlines with the arch's closed geometry introduces a paramagnetic drag force in the shock region. Despite this, net positive thrust is achieved through the interaction of plasma currents with the applied magnetic field. Incorporating the self-induced magnetic field reveals that a the plasma-induce magnetic field pushes against the imposed magnetic lines, reducing drag and enhancing thrust. Magnetic thrust increases steadily even for moderate β_0

values, highlighting the significant role of the self-induced field in the magnetic arch configuration compared to its minor effect in axisymmetric nozzles. Ongoing experiments [135] are consistent with these findings, preliminarily providing experimental validation for the behaviour observed here.

An extension of the code including a neutral fluid, ion and neutral internal energy and several collisional processes was employed to study the effect of neutral dynamics and facility effects on the performance and operation of axisymmetric nozzles. This study is framed in the recent efforts of the space propulsion community to better characterize the effects of ground testing on the performance of EPTs. It has been shown in 5 that ion-neutral charge exchange collisions and ionization collisions do not affect strongly the acceleration of ions in a magnetic nozzle in the simulated scenarios. In fact, it was shown that the enhanced plasma mass flow provided by late ionization in the plume slightly increases the thrust produced by the nozzle at constant T_e. However, this effect is accompanied by a strong increase in the power needed to sustain the discharge with the same electron temperature. This power has to be supplied to the plume in the form of an increased electron heat-flux at the source and leads to a marked decrease in MN efficiency along with an increased effective cooling rate in the electron fluid. These findings align with experimental evidence, confirming that the performance loss in magnetic nozzles operating in poor vacuum conditions is primarily caused by electron inelastic collisions, which enhance the cooling rate of the electron fluid, reducing the amount of thermal energy available in the plume to be converted into ion kinetic energy, ultimately lowering overall performance.

Future lines of work

The possible lines of work that open from this thesis have been pointed out in the are two fold. On the one hand, the models employed in the `POSETS` solver are all based on the perfectly magnetised drift-diffusive model of the electrons. This model, despite its computational advantages is limited to the study of only zeroth-order finite electron Larmor radius effects, this model also limits the thermodynamics of electrons to a simple polytropic or isothermal model which, as we have shown, is a limitation in the case of high background pressures. Therefore, from the point of view of the models employed here, the most promising extension of the present work is the improvement of the electron model. The main change in the electron model should be the inclusion of electron collisionality on the electron momentum equation as it has been proved here that this effect is of higher relevance than electron inertia, this could be included in the equations as a generalized Ohm's law. This change would lead to a deep change in the electron module of the code but would be beneficial, particularly in the resolution of the closed line geometry of the magnetic arch in chapter 4. On the other hand, the inclusion of the electron energy

equation would allow for a better description of the cooling of the electron fluid due to collisional processes in poor vacuum conditions and therefore get a self-consistent picture of the performance loss of the nozzle due to collisions with neutrals. This extension of the model would imply several changes in the code, specifically the term involving the divergence of the heat-flux tensor which gives a parabolic character to that equation would need to be discretized. To that end an a DG method for the discretization of second order elliptic problems such as the Symmetric Interior Penalty Galerkin (SIPG) method or the Local DG method (LDG) would need to be implemented.

From the point of view of the numerical methods employed here, a speed up of the solver could be obtained by using the so-called Hybridizable DG methods(HDG) which reduce the number of degrees of freedom in the discretized system while conserving the beneficial properties of DG methods. Finally, adapting the code to the latest versions of the `FEniCS` library, so-called, `FEniCSx` would be desirable in order to maintain its future support.

Bibliography

[1] Stéphane Mazouffre. Electric propulsion for satellites and spacecraft: established technologies and novel approaches. *Plasma Sources Science and Technology*, 25(3):033002, 2016.

[2] Eduardo Ahedo. Plasmas for space propulsion. *Plasma Physics and Controlled Fusion*, 53(12):124037, 2011.

[3] D.M. Goebel and I. Katz. *Fundamentals of Electric Propulsion: Ion and Hall Thrusters*. Jet Propulsion Laboratory, Pasadena, CA, 2008.

[4] R.G. Jahn. *Physics of Electric Propulsion*. Dover, 2006.

[5] Francis M Curran and Thomas W Haag. Extended life and performance test of a low-power arcjet. *Journal of Spacecraft and Rockets*, 29(4):444–452, 1992.

[6] P.J. Wilbur. Ion thruster development trends and status in the united states. *Journal Propulsion and Power*, 14:708–715, 1998.

[7] K.H. Groh and H.W. Loeb. State of the art of radio-frequency ion sources for space propulsion). *Review of scientific instruments*, 65(5):1741–1744, 1994.

[8] D.M. Goebel, R.E. Wirz, and I. Katz. Analytical ion thruster discharge performance model. *Journal of Propulsion and Power*, 23(5):1055–1067, 2007.

[9] A.I. Morozov and V.V. Savelyev. Fundamentals of stationary plasma thruster theory. In *Reviews of Plasma Physics, Vol. 21*, New York, 2000. Kluwer Academic.

[10] E. Choueiri. Fundamental difference between the two Hall thruster variants. *Physics of Plasmas*, 8(11):5025–5033, 2001.

[11] D. Rafalskyi, J. Martínez-Martínez, L. Habl, E. Zorzoli-Rossi, P. Proynov, A. Boré, T. Baret, A. Poyet, T. Lafleur, S. Dudin, and A. Aanesland. In-orbit demonstration of an iodine electric propulsion system. *Nature*, 599:411–415, 2021.

[12] JM. Tejeda and A. Knoll. A water vapour fuelled Hall effect thruster: characterization and comparison with oxygen. *Acta Astronautica*, 211:702–715, 2023.

[13] R.W. Boswell and F.F. Chen. Helicons-the early years. *IEEE Transactions on Plasma Science*, 25:1229–1244, 1997.

[14] F.F. Chen and R.W. Boswell. Helicons-the past decade. *IEEE Transactions on Plasma Science*, 25:1245–1257, 1997.

[15] J.C. Sercel. Electron-cyclotron-resonance (ECR) plasma acceleration. In *AIAA 19th Fluid Dynamics, Plasma Dynamics and Lasers Conference*, 1987.

[16] J. Jarrige, P.Q. Elias, F. Cannat, and D. Packan. Characterization of a coaxial ecr plasma thruster. In *44th AIAA Plasmadynamics and Lasers Conference, San Diego*, 2013.

[17] SN Bathgate, MMM Bilek, and DR Mckenzie. Electrodeless plasma thrusters for spacecraft: a review. *Plasma Science and Technology*, 19(8):083001, 2017.

[18] F.F. Chen. Plasma ionization by helicon waves. *Plasma Physics and Controlled Fusion*, 33(4):339, 1991.

[19] J. Freidberg. *Plasma Physics and Fusion Energy*. Cambridge University Press, 2007.

[20] Eduardo Ahedo and Mario Merino. Two-dimensional supersonic plasma acceleration in a magnetic nozzle. *Physics of Plasmas*, 17(7):073501, 2010.

[21] Mario Merino and Eduardo Ahedo. Contactless steering of a plasma jet with a 3D magnetic nozzle. *Plasma Sources Science and Technology*, 26(9):095001, 2017.

[22] Jaume Navarro-Cavallé, Mick Wijnen, Pablo Fajardo, Eduardo Ahedo, V. Gómez, A. Giménez, and M. Ruiz. Development and characterization of the helicon plasma thruster prototype hpt05m. In 36^{th} *International Electric Propulsion Conference*, number IEPC-2019-596, Vienna, Austria, 2019. Electric Rocket Propulsion Society.

[23] F. Trezzolani, M. Manente, E. Toson, A. Selmo, D. Moretto, M. Magarotto, F. Bos, P. De Carlo, D. Melazzi, and D. Pavarin. Development and testing of a miniature helicon plasma thruster. In *35th International Electric Propulsion Conference, Atlanta, GA, IEPC-2017-519*, 2017.

[24] M. R. Inchingolo, M. Merino, M. Wijnen, and J. Navarro-Cavallé. Thrust measurements of a waveguide electron cyclotron resonance thruster. *Journal of Applied Physics*, 135(9), 3 2024.

[25] K. Takahashi. Thirty percent conversion efficiency from radiofrequency power to thrust energy in a magnetic nozzle plasma thruster. *Scientific Reports*, 12:18618, 2022.

[26] Victor Désangles, Denis Packan, Julien Jarrige, Simon Peterschmitt, Patrick Dietz, Steffen Scharmann, Kristof Holste, and Peter J Klar. Ecra thruster advances: 30w and 200w prototypes latest performances. *Journal of Electric Propulsion*, 2(1):10, 2023.

[27] Filippo Cichocki, Mario Merino, and Eduardo Ahedo. Three-dimensional geomagnetic field effects on a plasma thruster plume expansion. *Acta Astronautica*, 175:190 – 203, 2020.

[28] Mario Merino, Diego García-Lahuerta, and Eduardo Ahedo. Plasma acceleration in a magnetic arch. *Plasma Sources Science and Technology*, 32(6):065005, 6 2023.

[29] E. Ahedo, P. Fajardo, M. Merino, J. Navarro-Cavallé, A. Sánchez-Villar, M. Wijnen, and J. Zhou. Helicon and ecr plasma sources for space propulsion: simulation and testing. In *2019 International Conference on Electromagnetics in Advanced Applications (ICEAA)*, pages 0788–0793, 2019.

[30] Mario Merino. *Analysis of magnetic nozzles for space plasma thrusters*. PhD thesis, Universidad Politécnica de Madrid, 2013.

[31] R.R. Hofer, P.Y. Peterson, and A.D. Gallimore. Characterizing vacuum facility backpressure effects on the performance of a Hall thruster. *IEPC Paper*, (01-045), 2001.

[32] A.L. Ortega, I.G. Mikellides, V.H. Chaplin, J.S. Snyder, and G. Lenguito. Facility pressure effects on a Hall thruster with an external cathode, i: numerical simulations. *Plasma Sources Science and Technology*, 29(3), 2020.

[33] Natalie RS Caruso and Mitchell LR Walker. Neutral ingestion effects on plume properties of a radio-frequency plasma discharge. *Journal of Propulsion and Power*, 34(1):58–65, 2018.

[34] A. Fruchtman, G. Makrinich, P. Chabert, and J.M. Rax. Enhanced plasma transport due to neutral depletion. *Physical review letters*, 95(11):115002, 2005.

[35] C.K. Birdsall and A.B. Langdon. *Plasma Physics via Computer Simulation*. Institute of Physics Publishing, Bristol, 1991.

[36] J.A. Bittencourt. *Fundamentals of plasma physics*. Springer, Berlin, Germany, 2004.

[37] Mario Merino, Javier Mauriño, and Eduardo Ahedo. Kinetic electron model for plasma thruster plumes. *Plasma Sources Science and Technology*, 27(3):035013, 2018.

[38] Gonzalo Sánchez-Arriaga, Jiewei Zhou, E Ahedo, Manuel Martínez-Sánchez, and Jesús José Ramos. Kinetic features and non-stationary electron trapping in paraxial magnetic nozzles. *Plasma Sources Science and Technology*, 27(3):035002, 2018.

[39] Bernardo Cockburn and Chi-Wang Shu. The runge–kutta discontinuous galerkin method for conservation laws v: multidimensional systems. *Journal of Computational Physics*, 141(2):199–224, 1998.

[40] Ralf Hartmann and Paul Houston. Adaptive discontinuous galerkin finite element methods for nonlinear hyperbolic conservation laws. *SIAM Journal on Scientific Computing*, 24(3):979–1004, 2003.

[41] Alberto Marín-Cebrián, Enrique Bello-Benítez, Adrián Domínguez-Vázquez, and Eduardo Ahedo. Macroscopic response of a Hall thruster discharge from an axial-radial PIC model. In 76^{th} *Gaseous Electronics Conference*, Ann Arbor, MI, October 9-13, 2023.

[42] E. Ahedo. Using electron fluid models to analyze plasma thruster discharges. *Journal of Electric Propulsion*, 2(1):2, 2023.

[43] G.F. Chew, M.L. Goldberger, and F.E. Low. The Boltzmann equation and the one-fluid hydromagnetic equations in the absence of particle collisions. *Proceedings of the Royal Society of London A*, 236:112–118, 1956.

[44] JM Little and EY Choueiri. Electron cooling in a magnetically expanding plasma. *Physical Review Letters*, 117(22):225003, 2016.

[45] Yunchao Zhang, Christine Charles, and Rod Boswell. Thermodynamic study on plasma expansion along a divergent magnetic field. *Physical review letters*, 116(2):025001, 2016.

[46] Eduardo Ahedo and Mario Merino. On plasma detachment in propulsive magnetic nozzles. *Physics of Plasmas*, 18(5):053504, 2011.

[47] Eduardo Ahedo, Sara Correyero, Jaume Navarro, and Mario Merino. Macroscopic and parametric study of a kinetic plasma expansion in a paraxial magnetic nozzle. *Plasma Sources Science and Technology*, 29(4):045017, 2020.

[48] Alfio E Vinci, Marco R Inchingolo, Stéphane Mazouffre, and Jaume Navarro-Cavallé. Ion dynamics in the magnetic nozzle of a waveguide ecr thruster via laser-induced fluorescence spectroscopy. *Journal of Physics D: Applied Physics*, 56(2):025204, 2022.

[49] S Correyero, J Jarrige, D Packan, and E Ahedo. Plasma beam characterization along the magnetic nozzle of an ECR thruster. *Plasma Sources Science and Technology*, 28(9):095004, 2019.

[50] M. R. Inchingolo, M. Merino, and J. Navarro-Cavallé. Plume characterization of a waveguide ecr thruster. *Journal of Applied Physics*, 133(11):113304, 2023.

[51] Alfio E Vinci, Stéphane Mazouffre, Víctor Gómez, Pablo Fajardo, and Jaume Navarro-Cavallé. Laser-induced fluorescence spectroscopy on xenon atoms and ions in the magnetic nozzle of a helicon plasma thruster. *Plasma Sources Science and Technology*, 31(9):095007, 2022.

[52] B Wachs and B Jorns. Background pressure effects on ion dynamics in a low-power magnetic nozzle thruster. *Plasma Sources Science and Technology*, 29(4):045002, 2020.

[53] Kazunori Takahashi, Yoshinori Takao, and Akira Ando. Performance improvement of a magnetic nozzle plasma thruster. In 36^{th} *International Electric Propulsion Conference*, 2019.

[54] R.R. Hofer, P.Y. Peterson, A.D. Gallimore, and R.S. Jankovsky. A high specific impulse two-stage Hall thruster with plasma lens focusing. In *7th International Electric Propulsion Conference, Pasadena, CA, USA*, IEPC-01-036, 2001.

[55] Mario Merino and Eduardo Ahedo. Effect of the plasma-induced magnetic field on a magnetic nozzle. *Plasma Sources Science and Technology*, 25(4):045012, 2016.

[56] Mario Merino. Motor espacial de plasma sin electrodos con geometría en U, 2019. PCT patent, Spanish Patent Office, Patent no. ES2733773.

[57] I. Bardi, O. Biro, and K. Preis. Perfectly matched layers in static fields. *IEEE Transactions on Magnetics*, 34(5):2433–2436, 1998.

[58] William H Reed and Thomas R Hill. Triangular mesh methods for the neutron transport equation. Technical report, Los Alamos Scientific Lab., N. Mex.(USA), 1973.

[59] Eleuterio F Toro. *Riemann solvers and numerical methods for fluid dynamics: a practical introduction*. Springer Science & Business Media, 2013.

[60] Dietmar Kröner. Numerical schemes for conservation laws. *(No Title)*, 1997.

[61] Vincent Wheatley, Harish Kumar, and Patrick Huguenot. On the role of riemann solvers in discontinuous galerkin methods for magnetohydrodynamics. *Journal of Computational Physics*, 229(3):660–680, 2010.

[62] Per-Olof Persson and Jaime Peraire. Sub-cell shock capturing for discontinuous galerkin methods. In *44th AIAA aerospace sciences meeting and exhibit*, page 112, 2006.

[63] Jan S Hesthaven and Tim Warburton. *Nodal discontinuous Galerkin methods: algorithms, analysis, and applications*. Springer Science & Business Media, 2007.

[64] Steffen Petersen, Charbel Farhat, and Radek Tezaur. A space–time discontinuous galerkin method for the solution of the wave equation in the time domain. *International journal for numerical methods in engineering*, 78(3):275–295, 2009.

[65] Chi-Wang Shu and Stanley Osher. Efficient implementation of essentially non-oscillatory shock-capturing schemes. *Journal of computational physics*, 77(2):439–471, 1988.

[66] Bernardo Cockburn and Chi-Wang Shu. Runge–kutta discontinuous galerkin methods for convection-dominated problems. *Journal of scientific computing*, 16:173–261, 2001.

[67] Noel Chalmers and Lilia Krivodonova. A robust cfl condition for the discontinuous galerkin method on triangular meshes. *Journal of Computational Physics*, 403:109095, 2020.

[68] Hans Petter Langtangen and Kent-Andre Mardal. *Introduction to numerical methods for variational problems*, volume 21. Springer Nature, 2019.

[69] Anders Logg, Kent-Andre Mardal, and Garth Wells. *Automated solution of differential equations by the finite element method: The FEniCS book*, volume 84. Springer Science & Business Media, 2012.

[70] Daniel Arndt, Wolfgang Bangerth, Maximilian Bergbauer, Marco Feder, Marc Fehling, Johannes Heinz, Timo Heister, Luca Heltai, Martin Kronbichler, Matthias Maier, Peter Munch, Jean-Paul Pelteret, Bruno Turcksin, David Wells, and Stefano Zampini. The `deal.II` library, version 9.5. *Journal of Numerical Mathematics*, 31(3):231–246, 2023.

[71] Oliver Sander. *DUNE—The distributed and unified numerics environment*, volume 140. Springer Nature, 2020.

[72] R. Anderson, J. Andrej, A. Barker, J. Bramwell, J.-S. Camier, J. Cerveny, V. Dobrev, Y. Dudouit, A. Fisher, Tz. Kolev, W. Pazner, M. Stowell, V. Tomov, I. Akkerman, J. Dahm, D. Medina, and S. Zampini. MFEM: A modular finite element methods library. *Computers & Mathematics with Applications*, 81:42–74, 2021.

[73] Santiago Badia and Francesc Verdugo. Gridap: An extensible finite element toolbox in julia. *Journal of Open Source Software*, 5(52):2520, 2020.

[74] Hendrik Ranocha, Michael Schlottke-Lakemper, Andrew R Winters, Erik Faulhaber, Jesse Chan, and Gregor J Gassner. Adaptive numerical simulations with trixi. jl: A case study of julia for scientific computing. *arXiv preprint arXiv:2108.06476*, 2021.

[75] Christophe Geuzaine and Jean-François Remacle. Gmsh: A 3-D finite element mesh generator with built-in pre-and post-processing facilities. *International journal for numerical methods in engineering*, 79(11):1309–1331, 2009.

[76] Yicheng Pang, Jianjun Ge, Zuozhi Liu, and Min Hu. The riemann problem for one-dimensional isentropic flow of a mixture of a non-ideal gas with small solid particles. *Results in Physics*, 15:102587, 2019.

[77] Esteban Ferrer, Gonzalo Rubio, Gerasimos Ntoukas, Wojciech Laskowski, Oscar A Mariño, Stefano Colombo, Andrés Mateo-Gabín, H Marbona, F Manrique de Lara, David Huergo, et al. : A high-order discontinuous galerkin solver for flow simulations and multi-physics applications. *Computer Physics Communications*, 287:108700, 2023.

[78] K. Takahashi. Helicon–type radiofrequency plasma thrusters and magnetic plasma nozzles. *Reviews of Modern Plasma Physics*, 3:3, 2019.

[79] Mario Merino and Eduardo Ahedo. Plasma detachment in a propulsive magnetic nozzle via ion demagnetization. *Plasma Sources Science and Technology*, 23(3):032001, 2014.

[80] Justin M Little and Edgar Y Choueiri. Electron demagnetization in a magnetically expanding plasma. *Physical review letters*, 123(14):145001, 2019.

[81] Mario Merino, Judit Nuez, and Eduardo Ahedo. Fluid-kinetic model of a propulsive magnetic nozzle. *Plasma Sources Science and Technology*, 30(11):115006, 2021.

[82] O.V. Batishchev. Mini-helicon plasma thruster characterization. In *44th Joint Propulsion Conference, Hartford, CT*, AIAA 2008-5293, 2008.

[83] D. Pavarin, F. Ferri, M. Manente, D. Curreli, Y. Guclu, D. Melazzi, D. Rondini, S. Suman, J. Carlsson, C. Bramanti, E. Ahedo, V. Lancellotti, K. Katsonis, and G. Markelov. Design of 50W helicon plasma thruster. In *31th International Electric Propulsion Conference*, IEPC 2009-205, 2009.

[84] Kazunori Takahashi, Christine Charles, and Rod Boswell. Approaching the theoretical limit of diamagnetic-induced momentum in a rapidly diverging magnetic nozzle. *Physical review letters*, 110(19):195003, 2013.

[85] J Navarro-Cavallé, M Wijnen, P Fajardo, and E Ahedo. Experimental characterization of a 1 kW helicon plasma thruster. *Vacuum*, 149:69–73, 2018.

[86] J.C. Sercel. Electron-cyclotron-resonance (ECR) plasma thruster research. In *24th Joint Propulsion Conference*, number 2916, 1988.

[87] T. Vialis, J. Jarrige, A. Aanesland, and D. Packan. Direct thrust measurement of an electron cyclotron resonance plasma thruster. *Journal of Propulsion and Power*, 34(5):1323–1333, 2018.

[88] Sara Correyero, Mario Merino, Paul-Quentin Elias, Julien Jarrige, Denis Packan, and Eduardo Ahedo. Characterization of diamagnetism inside an ECR thruster with a diamagnetic loop. *Physics of Plasmas*, 26(5):053511, 2019.

[89] Antonella Caldarelli, Félicien Filleul, Christine Charles, Rod Boswell, Nicholas Rattenbury, and John Cater. Radial characterization of an ion beam in a deflected magnetic nozzle. *Journal of Electric Propulsion*, 1(1):10, 2022.

[90] Benjamin W. Longmier, Jared P. Squire, Mark D. Carter, Leonard D. Cassady, Tim W. Glover, William J. Chancery, Chris S. Olsen, Andrew V. Ilin, Greg E. Mccaskill, and Franklin R. Chang Díaz. Ambipolar Ion Acceleration in the Expanding Magnetic Nozzle of the VASIMR ® VX-200i. In *45th AIAA/ASME/SAE/ASEE Joint Propulsion Conference & Exhibit*, number August, pages 1–10, 2009.

[91] Mario Merino, Diego García-Lahuerta, Célian Boyé, Jaume Navarro-Cavallé, and Eduardo Ahedo. Preliminary model of the plasma expansion in a magnetic arch thruster (and overview of the first prototype). In 37^{th} *International Electric Propulsion Conference*, number IEPC-2022-423, Boston, MA, June 19-23, 2022. Electric Rocket Propulsion Society.

[92] Mario Merino and Eduardo Ahedo. Influence of electron and ion thermodynamics on the magnetic nozzle plasma expansion. *IEEE Transactions on Plasma Science*, 43(1):244–251, 1 2015.

[93] Kazunori Takahashi, Trevor Lafleur, Christine Charles, Peter Alexander, and Rod W Boswell. Axial force imparted by a current-free magnetically expanding plasma. *Physics of Plasmas*, 19(8):083509, 2012.

[94] Justin M Little and Edgar Y Choueiri. Critical condition for plasma confinement in the source of a magnetic nozzle flow. *IEEE Transactions on Plasma Science*, 43(1):277–286, 2015.

[95] C.S. Olsen, M.G. Ballenger, M.D. Carter, F.R. Chang Diaz, M. Giambusso, T.W. Glover, A.V. Ilin, J.P. Squire, B.W. Longmier, E.A. Bering, and P.A.

Cloutier. Investigation of plasma detachment from a magnetic nozzle in the plume of the vx-200 magnetoplasma thruster. *Plasma Science, IEEE Transactions on*, 43(1):252–268, 2015.

[96] B.R. Roberson, R. Winglee, and J. Prager. Enhanced diamagnetic perturbations and electric currents observed downstream of the high power helicon. *Physics of Plasmas*, 18(5):053505, 2011.

[97] Mario Merino Diego García-Lahuerta and Eduardo Ahedo. Effect of collisions and facility effects on magnetic nozzle operation. *Plasma Sources Science and Technology*, (under review).

[98] C. Charles and R. Boswell. Current-free double-layer formation in a high-density helicon discharge. *Applied Physics Letters*, 82(9):1356–1358, 2003.

[99] O.V. Batishchev. Minihelicon plasma thruster. *IEEE Transactions on Plasma Science*, 37(8):1563–1571, 2009.

[100] K. Takahashi, T. Lafleur, C. Charles, P. Alexander, R.W. Boswell, M. Perren, R. Laine, S. Pottinger, V. Lappas, T. Harle, et al. Direct thrust measurement of a permanent magnet helicon double layer thruster. *Applied Physics Letters*, 98:141503, 2011.

[101] Federico Boni, Victor Désangles, and Julien Jarrige. Experimental characterization of thrust production mechanisms in a magnetic nozzle ecr thruster. *Journal of Electric Propulsion*, 1(1):33, 2022.

[102] Alfio E Vinci and Stéphane Mazouffre. Direct experimental comparison of krypton and xenon discharge properties in the magnetic nozzle of a helicon plasma source. *Physics of Plasma*, 28:033504, 2021.

[103] S.A. Andersen, V.O. Jensen, P. Nielsen, and N. D'Angelo. Continuous supersonic plasma wind tunnel. *Phys. Fluids*, 12(3):557–560, 1969.

[104] Anna Sheppard and Justin Little. Performance analysis of an electron cyclotron resonance thruster with various propellants. In *AIAA Propulsion and Energy 2021 Forum*, page 3375, 2021.

[105] Manuel Martínez-Sánchez, Jaume Navarro-Cavallé, and Eduardo Ahedo. Electron cooling and finite potential drop in a magnetized plasma expansion. *Physics of Plasmas*, 22(5):053501, 2015.

[106] J. C. Porto and P.Q. Elias. Full-pic simulation of an ecr plasma thruster with magnetic nozzle. In *IEPC 2019*, 2019.

[107] Shaun Andrews, Simone Di Fede, and Mirko Magarotto. Fully kinetic model of plasma expansion in a magnetic nozzle. *Plasma Sources Science and Technology*, 2022.

[108] A study of an air-breathing electrodeless plasma thruster discharge. *Propulsion and Power Research*, 2024.

[109] Filippo Cichocki, Adrián Domínguez-Vázquez, Mario Merino, and Eduardo Ahedo. Hybrid 3D model for the interaction of plasma thruster plumes with nearby objects. *Plasma Sources Science and Technology*, 26(12):125008, 2017.

[110] J. Zhou, A. Domínguez-Vázquez, P. Fajardo, and E. Ahedo. Magnetized fluid electron model within a two-dimensional hybrid simulation code for electrodeless plasma thrusters. *Plasma Sources Science and Technology*, 31(4):045021, 2022.

[111] A. Sánchez-Villar, J. Zhou, M. Merino, and E. Ahedo. Coupled plasma transport and electromagnetic wave simulation of an ECR thruster. *Plasma Sources Science and Technology*, 30(4):045005, 2021.

[112] Thomas A Marks, Ioannis G Mikellides, Alejandro Lopez Ortega, and Benjamin Jorns. Hall2De simulations of a magnetic nozzle. In *AIAA Propulsion and Energy 2020 Forum*, AIAA 2020-3642, 2020.

[113] M.R. Nakles and W. A. Hargus. Background pressure effects on ion velocity distribution within a medium-power Hall thruster. *Journal of Propulsion and Power*, 27(4), 2011.

[114] Théo Vialis, Julien Jarrige, and Denis Packan. Geometry optimization and effect of gas propellant in an electron cyclotron resonance plasma thruster. In *Proc. 35th Int. Electr. Propuls. Conf*, pages 1–12, 2017.

[115] Jiewei Zhou, Gonzalo Sánchez-Arriaga, and Eduardo Ahedo. Time-dependent expansion of a weakly-collisional plasma beam in a paraxial magnetic nozzle. *Plasma Sources Science and Technology*, 30(4):045009, 2021.

[116] Raoul Andriulli, Shaun Andrews, Nabil Souhair, Mirko Magarotto, and Fabrizio Ponti. Fully kinetic study of facility pressure effects on rf-source magnetic nozzles. *Acta Astronautica*, 215:362–372, 2024.

[117] S Baldinucci, Sophia Bergmann, Jack A Hondagneu, Benjamin Wachs, and Benjamin A Jorns. Impact of facility electrical boundary conditions on the performance of an electron cyclotron resonance magnetic nozzle thruster. In *37th International Electric Propulsion Conference*, IEPC-2022-510, Boston, MA, June 19-23, 2022.

[118] Sara Correyero Plaza, Julien Jarrige, Denis Packan, and Eduardo Ahedo Galilea. Measurement of anisotropic plasma properties along the magnetic nozzle expansion of an electron cyclotron resonance thruster. In 35^{th} *International Electric Propulsion Conference*, IEPC-2017-437, Atlanta, GA, 2017. Electric Rocket Propulsion Society.

[119] Kazunori Takahashi, Hikaru Akahoshi, Christine Charles, Rod W Boswell, and Akira Ando. High temperature electrons exhausted from rf plasma sources along a magnetic nozzle. *Physics of Plasmas*, 24(8):084503, 2017.

[120] June Young Kim, Kyoung-Jae Chung, Kazunori Takahashi, Mario Merino, and Eduardo Ahedo. Kinetic electron cooling in magnetic nozzles: experiments and modeling. *Plasma Sources Science and Technology*, 32(7):073001, 2023.

[121] Matteo Guaita, Mario Merino, and Eduardo Ahedo. Hybrid pic-fluid simulations of the plasma expansion through a magnetic arch. In 38^{th} *International Electric Propulsion Conference*, number IEPC-2024-471, Toulouse, France, June 23-28, 2024. Electric Rocket Propulsion Society.

[122] Danis Packan, Paul-Quentin Elias, Julien Jarrige, Theo Vialis, Sara Correyero, Simon Peterschmitt, J.C. Porto-Hernandez, Mario Merino, Álvaro Sánchez-Villar, Eduardo Ahedo, G. Peyresoubes, A. Thorinius, S. Denis, Kristoff Holste, Peter Klar, S. Scharmann, J. Zorn, M. Bekemans, T. Scalais, E. Bourguignon, S. Zurbach, P. Azais, I. Habbassi, Magali Mares, and Andy Hoque. H2020 MINOTOR: Magnetic nozzle electron cyclotron resonance thruster. In 36^{th} *International Electric Propulsion Conference*, number IEPC-2019-875, Vienna, Austria, 2019. Electric Rocket Propulsion Society.

[123] S Correyero Plaza, Julien Jarrige, Denis Packan, and Eduardo Ahedo. Ion acceleration in the magnetic nozzle of an ecr thruster: Comparison of experimental measurements with a quasi 1d kinetic model. In *Space Propulsion 2018*, 2018.

[124] TA Collard and BA Jorns. Magnetic nozzle efficiency in a low power inductive plasma source. *Plasma Sources Science and Technology*, 28(10):105019, 2019.

[125] C. Charles. High density conics in a magnetically expanding helicon plasma. *Applied Physics Letters*, 96(5):051502–051502, 2010.

[126] S. K. Saha, S. Raychaudhuri, S. Chowdhury, M. S. Janaki, and A. K. Hui. Two-dimensional double layer in plasma in a diverging magnetic field. *Physics of Plasmas*, 19(9):092502, 2012.

[127] Eduardo Ahedo and Mario Merino. Two-dimensional plasma expansion in a magnetic nozzle: separation due to electron inertia. *Physics of Plasmas*, 19(8):083501, 2012.

[128] J.J. Ramos. General expression of the gyroviscous force. *Physics of Plasmas*, 12(11):112301, 2005.

[129] John S Snyder, Giiovanni Lenguito, Jason D Frieman, Thomas W Haag, and Jonathan A Mackey. The effects of background pressure on spt-140 thruster

performance at multiple power levels. In *AIAA/SAE/ASEE Joint Propulsion Conference*, number GRC-E-DAA-TN57023, 2018.

[130] K. Takahashi and T. Fujiwara. Observation of weakly and strongly diverging ion beams in a magnetically expanding plasma. *Applied Physics Letters*, 94:061502, 2009.

[131] C. Charles and R. Boswell. Laboratory evidence of a supersonic ion beam generated by a current-free 'helicon' double-layer. *Physics of Plasmas*, 11:1706–1714, 2004.

[132] E. Ahedo, P. Martínez-Cerezo, and M. Martínez-Sánchez. One-dimensional model of the plasma flow in a Hall thruster. *Physics of Plasmas*, 8:3058–3068, 2001.

[133] E. Bello-Benítez and E. Ahedo. Axial-azimuthal, high-frequency modes from global linear-stability model of a Hall thruster. *Plasma Sources Science and Technology*, 30(3):035003, 3 2021.

[134] Davide Poli, Enrique Bello-Benítez, Pablo Fajardo, and Eduardo Ahedo. Time-dependent axial fluid model of the hall thruster discharge and its plume. *Journal of Physics D: Applied Physics*, 2023.

[135] Célian Boyé, Jaume Navarro-Cavallé, and Mario Merino. Magnetic arch plasma expansion in a cluster of two ecr plasma sources. *Journal of Electric Propulsion*, (accepted).